Cavitation simulation on marine propellers

Shin, Keun Woo

Publication date:
2010

Document Version
Publisher's PDF, also known as Version of record

Cavitation simulation on marine propellers

PhD Thesis

$$(EIv'')'' = q - \rho A\ddot{v}$$

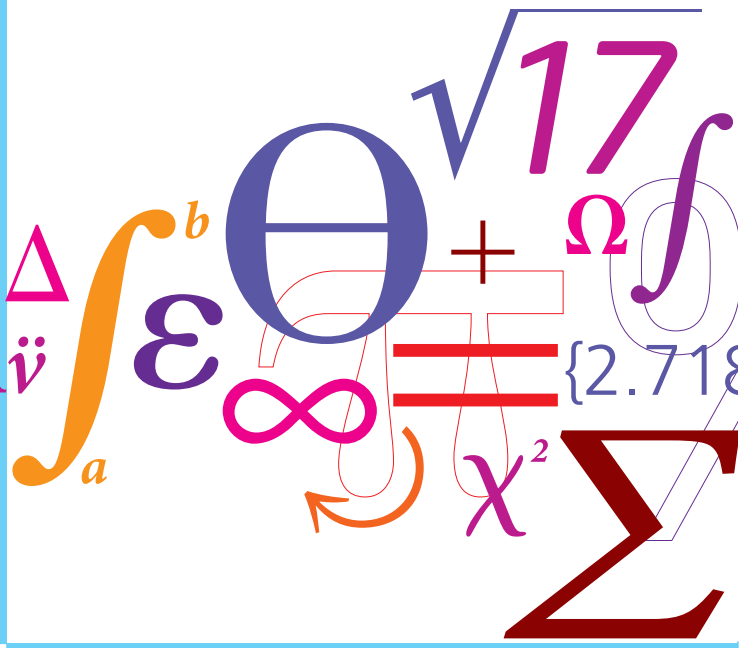

Keun Woo Shin
November 2010

DTU Mechanical Engineering
Department of Mechanical Engineering

Cavitation simulation on marine propellers

Keun Woo Shin

TECHNICAL UNIVERSITY OF DENMARK
DEPARTMENT OF MECHANICAL ENGINEERING
SECTION OF COASTAL, MARITIME AND STRUCTURAL ENGINEERING
NOV 2010

Published in Denmark by
Technical University of Denmark

Section of Coastal, Maritime and Structural Engineering
Department of Mechanical Engineering
Technical University of Denmark
Nils Koppels Alle, Building 403, DK-2800 Kgs. Lyngby, Denmark
Phone +45 4525 1360, Telefax +45 4588 4325
E-mail: info.skk@mek.dtu.dk
WWW: http://www.mek.dtu.dk/

Publication Reference Data
Shin, K. W.
Cavitation simulation on marine propellers
PhD Thesis
Technical University of Denmark, Section of Coastal, Maritime and Structural Engineering.
Nov, 2010
ISBN 978-87-90416-45-4
Keywords: Cavitation, RANS, CFD, VOF, Bubble Dynamics, Marine Propeller

Preface

This thesis is submitted as a partial fulfilment of the requirements for the Ph.D. degree. The work has been carried at the Section of the Coastal, Maritime and Structural Engineering (SKK) in the Department of the Mechanical Engineering in the Technical University of Denmark (DTU) during the Ph.D. program from September 2007 to October 2010. It has been supervised by Associate Professor Poul Andersen in SKK and Professor Jens Nørkær Sørensen in the Section of the Fluid Mechanics (FM). It has been financed by DTU and the Danish Centre for Maritime technology (DCMT). The financial support is gratefully acknowledged.

I am grateful to Associate Professor Poul Andersen for his guidance and encouragement throughout the whole Ph.D. program. I would like to thank Associate Professor Wen Zhong Shen, Assistant Professor Robert Flemming Mikkelsen and Professor Jens Nørkær Sørensen in FM for their support and advise on the overall numerical implementation and computation.

A part of the work has been conducted during my 6-month research visit to the Institute of Fluid Dynamics and Ship Theory in Technical University of Hamburg-Harburg. An important progress in the numerical implementation of pressure-correction equation has been made during this stay. I would like to thank Professor Moustafa Abdel-Maksoud and Professor Thomas Rung for their advise.

First of all, I thank God who sustains me and guides my steps. I would also like to thank all those who pray for me.

Kgs.Lyngby, 26 October, 2010
Keun Woo Shin

This page is intentionally left blank.

Abstract

Cavitation on marine propellers causes thrust breakdown, noise, vibration and erosion. The increasing demand for high-efficiency propellers makes it difficult to avoid the occurrence of cavitation. Currently, practical analysis of propeller cavitation depends on cavitation tunnel test, empirical criteria and inviscid flow method, but a series of model test is costly and the other two methods have low accuracy.

Nowadays, computational fluid dynamics by using a viscous flow solver is common for practical industrial applications in many disciplines. Cavitation models in viscous flow solvers have been developed in the last decade. They show the potential for the simulation of propeller cavitation with robustness, but they are still to be more proved for practical applications. In the present work, hydrodynamic and numerical characteristics of several cavitation models developed for a viscous flow solver are investigated, and one of the cavitation models is verified for the cavitation simulation on marine propellers.

Three cavitation models with a vapor transport equation and a cavitation model with a barotropic state law are implemented in the in-house RANS solver, EllipSys. The numerical results for cavitating flows on a 2D hydrofoil are compared with the experimental results. In the current implementation, three models with a vapor transport equation show numerical stability and equivalently good accuracy in simulating steady and unsteady sheet cavitation.

More validations for cavitating flows on 3D hydrofoils and conventional/highly-skewed propellers are performed with one of three cavitation models proven in 2D analysis. 3D cases also show accuracy and robustness of numerical method in simulating steady and unsteady sheet cavitation on complicated geometries. Hydrodynamic characteristics of cavitation like lift/drag variation with respect to cavity extent, re-entrant jet at the cavity closure and periodic oscillation of the cavity closure are demonstrated in the numerical results.

The cavitation simulations on propellers are performed in the open-water and behind-hull conditions. In the behind-hull condition, the wake field from a hull is applied to a plane upstream from the propeller by using the actuator disk model instead of modeling a whole hull. The computed cavity profile shows a reasonable agreement with the experimental result and the transient nature of propeller cavitation behind a hull is reproduced in the simulation.

The overall results suggest the possibility of the cavitation model in the RANS solver to be used for practical applications in propeller design process as a complementary tool to the cavitation tunnel test and the other numerical methods. The outstanding issue for cloudy and vortex cavitation requires further improvement and validation.

Synopsis

Kavitation på skibspropellere er årsag til formindsket propellerkraft, støj, vibrationer og erosion. De forøgede krav om propellere med høj virkningsgrad gør det vanskeligt at undgå kavitation. I dag analyseres propellerkavitation ved hjælp af modelforsøg i en kavitationstunnel, empiriske metoder eller numeriske strømningsberegning uden friktion; men modelforsøg er kostbare og de to andre metoder har begrænset nøjagtighed.

Numeriske strømningsberegninger, CFD (computational fluid dynamics), hvor viskositet tages med i beregningerne, er blevet almindelige for anvendelser i industrien. Kavitationsmodeller for viskose strømningsberegninger har været under udvikling gennem de seneste ti år. Disse modeller viser potentialet for simulering af kavitation i beregningerne med hensyn til robusthed; men der er stadig et behov for at afprøve dem på praktiske strømningsproblemer. I det foreliggende arbejde er flere kavitationsmodeller i en viskos strømningsløser undersøgt med hensyn til deres hydrodynamiske og numeriske egenskaber, og én af kavitationsmodellerne er testet ved beregning af kavitation på propellere.

Fire kavitationsmodeller er implementeret i DTU's og Risø-DTU's RANS-løser EllipSys. Tre af modellerne er baseret på en transportligning for damp, mens den fjerde er baseret på en tryk-massefylde-sammenhæng. Numeriske resultater for to-dimensional strømning med kavitation for et hydrofoil er sammenlignet med forsøgsresultater. De tre førstnævnte modeller er numerisk stabile og har tilsvarende god nøjagtighed i beregningerne af såvel stationær som instationær strømning.

Yderligere beregninger og sammenligninger med forsøg er udført for hydrofoils i tre-dimensional strømning og for en konventionel og en high-skew propeller. Alle disse beregninger er udført med den ene af de tre ovennævnte kavitationsmodeller, der både er robust og nøjagtig ved simulering af stationær og instationær lag-kavitation ved sådanne komplicerede geometrier. Beregningerne gengiver typiske kavitationsfænomener såsom variation af løft og modstand med kavitationens udstrækning, re-entrant jet og oscillerende grænse ved kavitetens nedstrøms afslutning.

Beregningerne for propellerkavitation er udført for åbent vand og propellere i medstrøm. I sidstnævnte tilfælde er medstrømsfeltet modelleret ved hjælp af en impulsskive anbragt opstrøms i forhold til propelleren i stedet for at modellere hele skibsskroget. Det beregnede kavitationsprofil viser rimelig overensstemmelse med forsøgsresultater, og den transiente karakteristik af kavitationsdannelsen og -henfaldet er gengivet i simuleringen.

De generelle resultater viser muligheden for at anvende kavitationsmodellen i RANS-beregningerne til praktiske anvendelser i propellerdesign og som supplement til modelforsøg og andre numeriske metoder. Beregninger for sky- og hvirvelkavitation kræver dog yderligere forbedringer i modellen.

Contents

Symbols

Latin letters

$A_{\phi,i}$	coefficient of the variable ϕ on i-node in the linear equation
$a_{\min}$	minimum sound speed
C	chord length
C_b	coefficient in the definition of $\partial\dot{m}/\partial p$ for Model 4
C_c	coefficient for condensation
C_D	drag coefficient
C_e	coefficient for evaporation
C_L	lift coefficient
C_p	pressure coefficient
c	chordwise distance
D	drag force
	propeller diameter
d	distance from the wall to the first-cell node
F_i	local force component
f	vapor mass fraction
f_i	local force-per-volume component
$f_{\max}$	maximum camber
g	gravitational acceleration
h	water depth
J	advance ratio
J_a	advance ratio based on the entrance velocity to the propeller
k	turbulent kinetic energy
K_T	thrust coefficient
K_Q	torque coefficient
L	largest length scale
	lift force
L_c	cavity length
$\dot{m}$	mass transfer rate per unit volume from vapor to liquid

N	number density of spherical microbubbles
	propeller rotation rate
n_{it}	number of iterations at each time step
$P_{0.7R}$	section pitch at 0.7 of propeller radius
Pr_v	turbulent Prandtl number for vapor
p	local pressure including static and dynamic pressure
p_b	pressure at bubble interface
p_c	critical bubble pressure for equilibrium condition
p_g	non-condensable gas pressure
p_v	vapor pressure
p_∞	ambient static pressure
p'	predicted pressure
p''	pressure after the pressure correction
p^c	corrected pressure
$\tilde{p}$	dynamic pressure
p_v^*	threshold pressure for phase change
Q	propeller torque
R	bubble radius
	propeller radius
$\dot{R}, \ddot{R}$	first- and second-order derivatives of bubble radius with respect to time
R_B	nucleation site radius
R_c	critical bubble radius for equilibrium condition
$R_{\max}, R_{\min}$	maximum and minimum microbubble radii
R_0	initial bubble radius
Rn	Reynolds number
r	propeller section radius
r, θ, z	cylindrical coordinates
$r_{\max}$	maximum normalized residual
r_{nuc}	nucleation site volume fraction
r_{te}	trailing-edge radius
S_ϕ	source term of a linear equation for the variable ϕ
St	Strouhal number
s_0	hydrofoil span
T	largest time scale
	surface tension
	oscillation period
	propeller thrust
t	time
$t_{\max}$	maximum thickness
t_∞	characteristic time scale
t^*	dimensionless time
U_∞	characteristic velocity
u_i	mean velocity component
u_θ	tangential velocity excluding frame rotating velocity
u_τ	friction velocity

u_i'	velocity fluctuation
u_i^*	velocity before under-relaxation
$\hat{u}_\theta$	tangential velocity including frame rotating velocity
V	axial inflow velocity
	ship advance speed
V_a	entrance velocity to the propeller
V_v	total vapor volume
V_v^*	dimensionless total vapor volume
w_i	local wake component
x, y, z	Cartesian coordinates
y^+	dimensionless wall distance

Greek letters

α	angle of attack
α_{cav}	under-relaxation factor for vapor transport equation
α_k	under-relaxation factor for turbulent kinetic energy transport equation
α_l	liquid volume fraction
α_p	under-relaxation factor for pressure correction equation
α_u	under-relaxation factor for momentum conservation equation
α_v	vapor volume fraction
α_ω	under-relaxation factor for specific dissipation rate transport equation
ΔA_i	projected surface area of a finite volume perpendicular to the i-direction
Δh	first-cell height
Δm_v	vapor mass in a finite volume
Δt	time step
ΔV	finite volume
ϵ	modeled dissipation rate
η	smallest length scale
	propeller open-water efficiency
μ	mixture viscosity
μ_t	turbulent viscosity
ξ, η, ζ	curvilinear coordinates
ρ	mixture density
$\rho\overline{u_i'u_j'}$	Reynolds stress tensor
σ	cavitation number
σ_n	cavitation number based on rotation rate
τ	smallest time scale
τ_{ij}	stress tensor
φ	blade angle
ω	frequency of imposed pressure oscillation
	specific dissipation rate
ω_n	natural frequency of bubble

Suffixes

l	liquid
v	vapor
P	central node of a finite volume
W, E, S, N, B, T	six neighboring nodes of a finite volume
w, e, s, n, b, t	six plane faces of a finite volume

Abbreviations

BC	Boundary condition
CDS	Central differencing scheme
CFD	Computational fluid dynamics
DES	Detached eddy simulation
HEM	Homogeneous equilibrium modeling
HSVA	Hamburgische Schiffbau- Versuchsanstalt (Hamburg Ship Model Basin)
ILLU	Incomplete line lower-upper factorization
ITTC	International Towing Tank Conference
LES	Large eddy simulation
MARIN	Maritime Research Institute of the Netherlands
MPI	Message passing interface
NACA	National Advisory Council for Aeronautics
RANS	Reynolds Averaged Navier Stokes
rps	Revolutions per second
SAM	Schwarz alternating method
SSPA	Statens Skeppsprovningsanstalt (Swedish National Ship Testing Facility)
SST	Shear stress transport
UDS	Upwind differencing scheme

Chapter 1

Introduction

1.1 Cavitation phenomenon

Cavitation is the formation of cavities i.e. vapor bubbles in a liquid when the pressure reaches the vicinity of the vapor pressure. Cavitation is a liquid-vapor phase change as in boiling, but it is caused by decreasing pressure, not by increasing temperature as in boiling.

In cavitation, the temperature of the liquid in the vicinity of the liquid-vapor interface is depressed, because the latent heat of vaporization is extracted from the liquid. The temperature depression and the corresponding drop of the vapor pressure are negligible in room temperature fluids. Therefore, thermodynamic effects of cavitation are ignored in the following research.

Cavitation commences at the pressure near the saturated vapor pressure p_v depending on the number density of microscopic nuclei i.e. minute particles and non-condensable gases. The dependency on water quality related to cavitation nuclei in experimental tests is on emphasis in these days. A low pressure acts as a tensile stress in the liquid and a rupture of the liquid initiates from weak spots like nuclei and material surface. The pressure inside a cavity is generally a bit larger than p_v, due to the partial pressure p_g of non-condensable gas.

The tendency of the flow to cavitate is nominally indicated by the cavitation number, which is the ratio of the static pressure margin above p_v to the kinetic energy per volume as follows

$$\sigma = \frac{p_\infty - p_v}{\frac{1}{2}\rho_l U_\infty^2} \tag{1.1}$$

where p_∞ is the ambient static pressure, ρ_l is the liquid density, and U_∞ is the reference velocity.

Cavitation is mostly an undesirable occurrence in high-speed liquid flow of various engineering devices such as ship propellers, hydrofoils, pumps, turbines, hydraulic systems etc, but it is unavoidable due to the demand for heavier loads. Cavitation results in the following negative effects:

- performance degradation: Cavitation results in the efficiency loss such as the breakdown of thrust and torque in ship propellers and the drop of pressure head in pumps. The unstable nature of cavitation brings the flow instability and pressure fluctuations, which make it difficult to control the amount of discharge liquid at the required timing in hydraulic systems.

- vibration: The flow instability and pressure fluctuation from the cavitation lead to the vibration of neighboring structure. The vibration from the vapor volume fluctuation of the attached cavitation occurs at the multiples of mechanical cyclic loading, but the cavity collapsing produces a broadband excitation having a risk of resonance with structural parts.

- noise: Cavitation accompanies the acoustic noise, as the acoustic pressure is caused by the vapor volume displacement. When the cavity collapses, its implosion emits a shock wave with high sound level of noise. The onset of cavitation is detected first by the noise rather than by visual observation of the bubble. Noise measurement is used for detecting cavitation in pumps and valves.

- erosion: When the cavity implosion takes place near enough to a solid boundary, the high pressures and temperatures of the shock wave cause material erosion (Philipp and Lauterborn, 1998). Once the erosion starts, it is accelerated by the increasing turbulence of flow and the additional cavitation due to the eroded pits.

In some industrial applications, the high pressure pulse of cavitation is utilized for removing contaminants stuck on the surface and dispersing suspended particles in liquid compound. The light emitted at the implosion of acoustically driven cavity, termed sonoluminescence, is on research for chemical and biomedical applications (Suslick, 2001).

1.2 Bubble dynamics

When a nucleus subject to cavitation is assumed to be a spherical microbubble with a constant external pressure p, the evolution of such a bubble can be explained by the Rayleigh-Plesset equation (Brennen, 1995 and Franc, 2007)

$$\rho_l \left(R\ddot{R} + \frac{3}{2}\dot{R}^2 \right) = p_b - p \tag{1.2}$$

where R is the bubble radius and $\dot{R}, \ddot{R}$ are the first- and second-order derivatives of R with respect to time.

The driving parameter for bubble dynamics is the instantaneous local pressure p. The pressure p_b at the bubble boundary is expressed by

$$p_b = p_v + p_g - \frac{2T}{R} - 4\mu_l \frac{\dot{R}}{R} \tag{1.3}$$

where T is the surface tension and μ_l is the dynamic viscosity of the liquid.

It is assumed that the mass of non-condensable gas inside the bubble remains constant and its behavior is polytropic so that

$$p_g = p_{g0} \left(\frac{R_0}{R} \right)^3 \tag{1.4}$$

where the subscript 0 refers to initial conditions.

The equilibrium condition of $p = p_b$ for $\dot{R} = \ddot{R} = 0$ is written by using the equations (1.3) and (1.4) as follows

$$p = p_{g0} \left(\frac{R_0}{R} \right)^3 + p_v - \frac{2T}{R} \tag{1.5}$$

The equilibrium radius versus the external pressure is shown in Figure 1.1. When p is smaller than the critical pressure p_c and R becomes larger than the critical radius R_c, the equilibrium becomes unstable and the bubble explodes to be a macroscopic cavitation bubble. The dotted line in Figure 1.1 indicates p_c and R_c. p_c is the minimum value in the equilibrium condition (1.5) and hence R_c is found by $\frac{dp}{dR} = 0$ as follows

$$R_c = \sqrt{\frac{3p_{g0}R_0^3}{2T}}, \qquad p_c = p_v - \frac{4T}{3R_c} \tag{1.6}$$

The results of measurements show that the radius of gas nucleus in natural water is generally between 2 and 50μm (Huang and Han, 1992). In the equilibrium condition for the standard atmospheric pressure $p = 100kPa$ and $p_v = 2.3kPa, T = 0.0728N/m$ at the temperature of 20^oC, the quantities of R_c, p_c etc for several values of R_0 are given in Table 1.1. As the nucleus is bigger, R_c/R_0 is larger and p_c is closer to p_v. p_c of the biggest nucleus is the inception pressure for cavitation.

The above equilibrium condition is limited for the case that p changes too rapidly for significant gas diffusion to occur. If sufficient time is allowed for dissolved gas to be transformed to non-condensable gas, it can get in instability for $p > p_c$. In case of periodic oscillations of p, p_c is a threshold value for stability, provided the frequency ω of the imposed oscillations

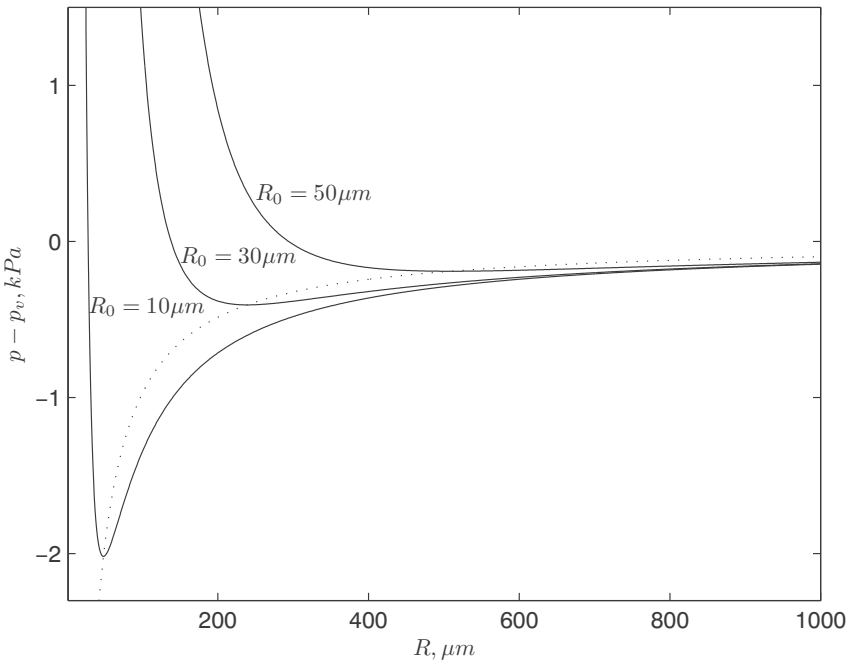

Figure 1.1: p as a function of R in the equilibrium condition

$R_0, \mu m$	p_{g0}, kPa	$R_c, \mu m$	$-\frac{4T}{3R_c}, kPa$	p_c, kPa
2	170.5	5.3	−18.3	−16.0
10	112.3	48.1	−2.0	0.3
30	102.6	238.9	−0.4	1.9
50	100.6	509.0	−0.2	2.1

Table 1.1: The critical pressure p_c for several values of the initial radius R_0 of gas nucleus

is smaller than the natural frequency ω_n of the bubble. For $\omega > \omega_n$, transient cavitation can occur for $p > p_c$. ω_n is defined by the peak frequency without viscous damping as follows (Franc, 2007)

$$\omega_n = \frac{1}{R_0}\sqrt{\frac{1}{\rho_l}\left(3p_{g0} - \frac{2T}{R_0}\right)} \tag{1.7}$$

For the developed cavitation bubble, the effects of non-condensable gas, surface tension and viscosity are negligible, i.e. $p_b \simeq p_v$. By the time integration of the equation (1.2) for $\dot{R}_0 = 0$ and a constant p, the interface velocity of a cavitation bubble is found as follows

$$\dot{R} = \pm\sqrt{\frac{2}{3}\frac{p_v - p}{\rho_l}\left[1 - \left(\frac{R_0}{R}\right)^3\right]} \tag{1.8}$$

While R increases ($R > R_0$) with a positive value of $\dot{R}$ for $p < p_v$, R decreases ($R < R_0$) with a negative value of $\dot{R}$ for $p > p_v$. As the cavity grows, the growth rate becomes dependent mainly on the pressure difference over p_v, but at the cavity collapse, the collapse rate increases and becomes infinite for $R = 0$. It is physically unreasonable. The collapse rate is attenuated by the compressibility of liquid, non-spherical and unstable shape of bubble and non-condensable gas, which are neglected in deriving the equation (1.8). The high interface velocity at the final stage of bubble collapse shows the potential for generating shock waves with high pressure and temperature.

1.3 Cavitating flows

Cavitating flows are described by the processes that nuclei are developed to macroscopic cavitation bubbles when they are convected into a low-pressure region within the flow, and the bubbles collapse when they are convected into a high-pressure region.

The cavitation of individual nuclei without interaction is called *bubble cavitation* (Figure 1.2(a)). It occurs when the number density of nuclei subject to macroscopic cavitation and the pressure gradient are relatively low. The spherical model of the Rayleigh-Plesset equation is approximately valid for the growth and collapse of a bubble, but the bubbles in real flows are not spherical due to the effects of pressure gradients, shear forces, solid surfaces etc.

In many flows, cavitation bubbles form in the vicinity of the minimum pressure point near a solid surface, except for vortex cavitation. The viscous boundary layer is usually thinner than the dimension of cavitation bubbles, hence the cavitation bubble interacts with the inviscid flow as well as the viscous boundary layer. Observations show that the cavitation bubbles on a solid surface are rather hemispherical and that they are separated from the solid surface by a thin liquid layer.

When traveling bubbles are dense enough for interaction, a separated region filled with vapor is formed and it is called *sheet cavitation* (figure 1.2(b,c,d,f)). It is also called *attached cavitation*, since it is attached to the suction side of a lifting body. When the separating flow is laminar, the cavitation initiates with a glassy smooth interface, whereas the initial interface is rough and irregular for turbulent flow, as shown in Figure 1.2(b). The interface becomes instable as the closure region is approached.

The cavity is suppressed with counter-rotating vortices at the closure, when Froude number is less than a critical value. The cavity is detached with a re-entrant jet and vortex shedding for higher Froude numbers, as shown in Figure 1.2(d,f). While the suppressed closure is rather steady, the position of the detached closure fluctuates with periodicity. When the attached cavity closes on the body surface, it is termed *partial cavitation* (Figure 1.2(b,d,f)). When the cavity extends over the entire body, it is termed *super-cavitation* (Figure 1.2(c)). The super-cavitation is applied for torpedoes and propellers on high-speed boats to reduce

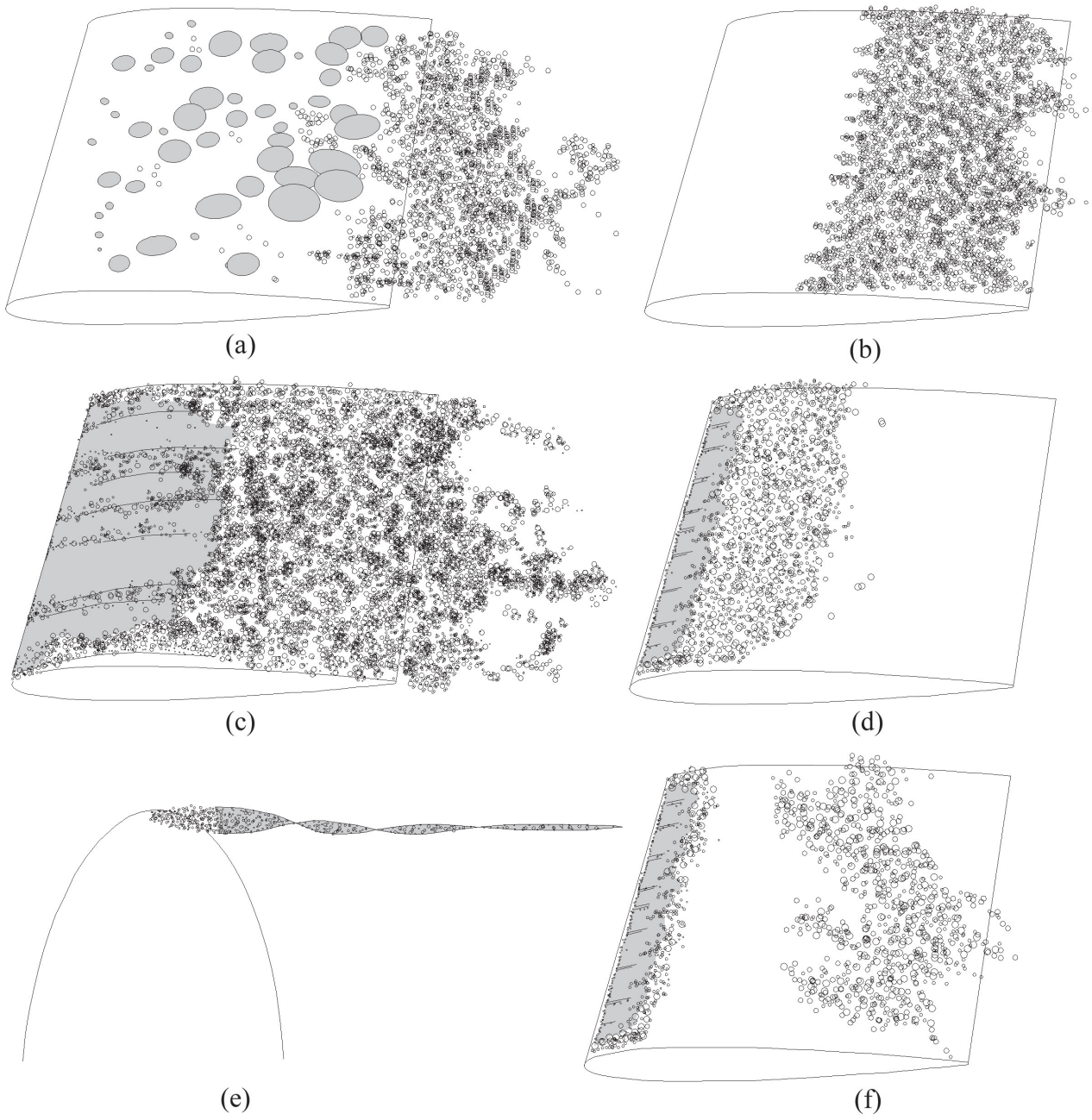

Figure 1.2: Cavitation types: (a) bubble cavitation, (b) sheet cavitation with rough initial interface, (c) super-cavitation, (d) unsteady sheet cavitation, (e) vortex cavitation, (f) cloud cavitation

viscous drag. Research on super-cavitating underwater vehicles is on progress for a military purpose.

In the fluctuating sheet cavitation, the cavity lengthens smoothly and shortens by shedding of cloud-like cavity. Such a dense cloud of micro-vortex cavities is called *cloud cavitation* (Figure 1.2(f)). The vortex sheet on the cavity interface and the re-entrant jet have an important role in generating cloud cavitation (Sato & Saito, 2001). A periodic disturbance imposed on the flow can cause cloud cavitation, as in the interaction between the behind-hull wake and a ship propeller. The coherent collapse of cloud cavity involving shock waves can cause serious noise, vibration and erosion (Brennen et al., 1999).

Cavitation may occur at the core of concentrated vorticity in the lifting-body flow as in the tip vortices of propeller blades and hydrofoils, since the pressure in the vortex core is often much lower than in the rest of the flow. It is called *vortex cavitation* (Figure 1.2(e)). The inception of tip vortex cavitation may occur continuously from the tip or some distance downstream, where individual bubbles are accumulated densely enough by the centrifugal pressure gradient of the vortex. Cloud cavitation with large transverse vortices may also be termed as vortex cavitation.

1.4 Numerical research on cavitation

Since experimental measurements are commonly supposed to be more faithful in reflecting cavitation physics in various predetermined conditions than numerical methods, the accuracy of numerical results is validated by comparison with experimental measurements. Experiments have uncertainty in measuring cavity interface and nuclei distribution, and a series of tests is costly. Current numerical methods for cavitation are ranked to be unmature for practical applications (ITTC, 2008). Therefore, it is essential to develop a reliable numerical method as a complementary or alternative tool.

Numerical methods for cavitation can be categorized mainly into two groups: interface tracking and homogeneous equilibrium modeling. In the former approach, the cavity interface is tracked with performing the computations only for the liquid phase, based on the assumption that the cavity region has a constant pressure equal to the vapor pressure. It is widely adopted for potential flow methods and Euler equation solvers. It is capable of simulating steady sheet cavitation, but may not be adequate for unsteady and scattered cavitation. It is often limited to 2D planar or axisymmetric flows and it requires cumbersome iterative procedures and preliminary knowledge for cavity closure. Although it is still used on the reason of computational efficiency, some expect that it would vanish in the next decade (ITTC, 2008).

In the homogeneous equilibrium modeling, the two-phase mixture is handled as a single-phase fluid with variable fluid properties corresponding to the composition of two phases, neglecting velocity slip between both phases. This approach is adopted primarily for viscous

flow solvers such as the Reynolds-averaged Navier-Stokes (RANS) solvers and large eddy simulation (LES) solvers. Phase changes are generally governed by either a barotropic state law or a fraction transport equation.

In the barotropic state law model, mixture density is linked to pressure by a barotropic state law. The changing rate of density in respect to pressure is an adjustable parameter defining density gradient at the cavity interface and physically it is related to the minimum sound speed in the mixture fluid.

Coutier-Delgosha et al. (2003) implement the cavitation model with a barotropic state law in a RANS solver, which simulates unsteady cloud cavitation on a 2D venturi-type section qualitatively well with a frequency close to the experimental measurement and with quantitative differences in the distributions of time-averaged velocity and vapor fraction within cavity.

Goncalves and Patella (2009) implement the cavitation model based on the homogeneous equilibrium modeling approach with a barotropic state law coupling the pressure and the density, and the stiffened-gas equation of state linking the pressure and the temperature to the thermodynamic in a compressible RANS solver with the energy equation. The computation shows the features of unsteady cloudy cavitation with some agreement in pressure distribution and quantitative differences in velocity profile and vapor volume fraction profile.

In the transport equation model, a transport equation is solved for either vapor volume fraction, liquid volume fraction or vapor mass fraction. The source term is related to the phase change rate, which is expressed as a function of the pressure and the fraction of a donor phase.

Kunz et al. (2000) develop a transport equation model with mixture momentum conservation equations, a volume continuity equation containing a mass transfer term and transport equations for liquid volume fraction and non-condensable gas volume fraction. All the equations incorporate a preconditioned pseudo-time derivative for favorable convergence characteristics. The computation by this model with $k - \epsilon$ turbulence model for steady and unsteady cavitation in 2D and 3D flows is in good agreement with experimental measurement of pressure distribution and shows reasonable cavitation patterns (Lindau et al., 2002). The computation for a 3D open-water propeller with homogeneous inflow is in good agreement with experimental results of thrust, torque and critical cavitation number for thrust/torque breakdown at lower than the design advance ratio (Lindau et al., 2005).

The vapor mass fraction transport equation proposed by Singhal et al. (2002), is based on the Rayleigh-Plesset equation and it includes the effect of turbulent flow. In the RANS solver for mixture fluids with $k - \omega$ and $k - \epsilon$ turbulence models, it has been applied for steady cavitation on a 2D hydrofoil, a 2D sharp-edged orifice and the results show good agreements in pressure distribution. Rhee et al. (2005) implement the cavitation model proposed by Singhal et al. in a RANS solver with additional capability accounting for the effects of slip velocities at the cavity interface. The computation for a 3D open-water propeller shows

good agreements in critical cavitation number for thrust/torque breakdown at lower advance ratio.

Senocak and Shyy (2004) develop a liquid fraction transport equation based on interface dynamics and a mixture mass continuity equation with a pressure-density coupling, leading to a convective and diffusive pressure correction equation. The computations for steady sheet cavitation on a 2D hydrofoil and a 2D venturi-type section show good agreements in pressure distribution, but they show quantitative differences from experimental measurements of the velocity field and the vapor volume fraction, especially at cavity closure region. The computation for unsteady cavitation reproduces the fore steady sheet cavitation, but it does not realize the large-scale structure of shedding cloud cavitation in the experimental observation.

Zwart et al. (2004) develop a vapor volume fraction transport equation based on the Rayleigh-Plesset equation and the validation examples show reasonable agreements in pressure distribution for steady cavitation on a 2D hydrofoil and in critical cavitation number for head drop of a 3D inducer at relatively low flow rates. The computation shows a reasonable unsteady cloud cavitation pattern on a 2D venturi-type section with an average frequency close to the experimental measurement.

Wikstrom (2005) implements the transport equation proposed by Kunz et al. in a LES solver. The computation for steady and unsteady cavitation on 2D and 3D hydrofoils shows reasonable cavitation patterns with quantitative differences from the experimental observations. The computation for a 3D open-water propeller with inhomogeneous inflow shows a qualitative agreement in cavity development and collapse for several propeller blade angles and a good agreement in thrust/torque breakdown at a value of advance ratio (Bensow, 2009).

Kim and Brewton (2008) implement a liquid volume fraction transport equation in the RANS solver with $k-\omega$ and $k-\epsilon$ turbulence models and the LES and detached eddy simulation (DES) solvers. The computation of all three solvers shows the main features of unsteady cloud cavitation on a 3D hydrofoil qualitatively well. The LES and DES computations show major oscillation frequencies closer to the experimental measurement than the RANS one.

Besides the Eulerian approach of all the models mentioned above, Hsiao and Chahine (2004) develop a cavitation model for the evolution, trajectory and shape of bubbles, based on the Rayleigh-Plesset equation, motion equation and free-surface boundary conditions in a Lagrangian specification. The Lagrangian bubble model is embedded in the unsteady RANS solver for the liquid phase with velocity/pressure perturbation equations. The characteristics of tip vortex cavitation are demonstrated by the simulations.

Although two-fluid model is more complicated and less popular, it is adopted for their compressible flow solver by Saurel and Lemetayer (2001). A set of conservation equations with mass transfer terms and transport equations of volume fraction and entity number density is solved for each phase. Phase changing is modeled by appropriate equations of state and average interface conditions. It is applied for a 2D supersonic cavitating flow.

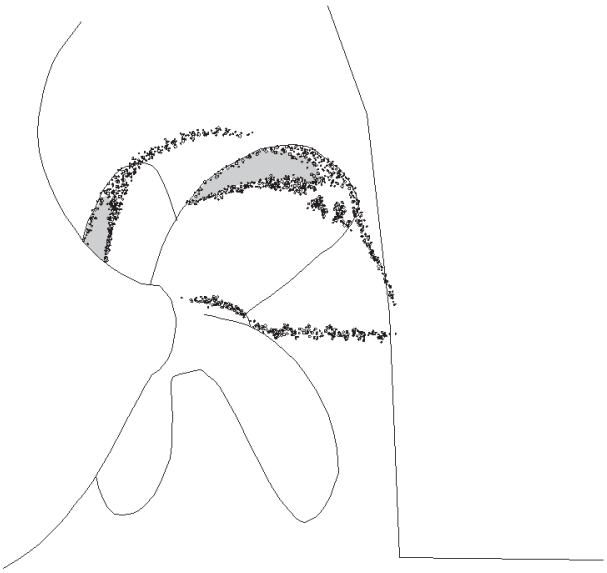

Figure 1.3: Cavitation around a ship propeller

1.5 Propeller cavitation

Cavitation on ship propellers may cause thrust breakdown, noise, vibration and erosion. These negative effects of cavitation bring an economic loss and obstruct fulfilling the requirements of specific ships. Although the detrimental effects of cavitation are crucial for propellers and ships, it is often unavoidable, because

- The propeller blade area is limited by the ship draft, but the power demand of modern ships is increasing. The propeller is more loaded by increasing rotating speed or blade lift coefficient.
- The propeller is mounted in the wake of the ship hull and the strongly non-uniform wake makes cavitation generally more susceptible. V-shaped hull sterns with a single screw arrangement result in high wake peaks. The wake field is more complicated when the ship is maneuvering.

Cavitation on ship propellers consists of one or more of bubble, sheet, cloud and vortex cavitation.

- Bubble cavitation normally occurs on the mid-chord region of the blade in non-separated flows. Model test shows that relatively large isolated bubbles are observed for smooth blade surface and their collapse is rather violent, but with roughness elements at the leading edge, large number of tiny bubbles appears and their collapse is less violent. Since bubble cavitation is known as being erosive, propellers are designed to exhibit

sheet cavitation rather than bubble cavitation with less camber and higher angle of attack. However, the basis for the erosion of bubble cavitation at full scale is not well documented (Kuiper, 1998).

- Sheet cavitation generally begins to appear at the leading edge on the suction side and it extends both chordwise and radially inward by increasing the angle of attack or decreasing the cavitation number. Extensive sheet cavitation brings thrust breakdown. Sheet cavitation is often unsteady or intermittent due to non-uniform wake inflow. The periodic variation of cavity volume leads to the pressure fluctuation on the aft body of ship at the multiples of blade frequency. The pressure amplitudes from cavity variation is generally four to six times those from blade loading and thickness without cavitation. In case with the stringent requirements for vibration and noise, tip loading is decreased at the expense of efficiency. The change from the conventional propeller to the highly skewed one can reduce low-frequency vibration and cavity extent. Sheet cavitation may occur at the inner radii of the pressure side and the blade root with instability. It is often related to the wake from the shaft angle and bossing. The propeller blade is designed to avoid it with a safety margin due to its effect on erosion.

- When sheet cavitation is strongly developed or it is periodically disturbed by the wake field, the cavity end is detached as a form of cloud cavitation. Bursting tip vortex cavitation may have the form of cloud cavitation. The collapsing of cloud cavitation at the blade surface is known the most harmful in material erosion. Broadband noise and vibration are related to the collapsing of cloud cavitation and tip vortex cavitation.

- Vortex cavitation occurs at blade tip, leading edge and propeller hub. At relatively low loading, vortex cavitation appears with a distance from tip or leading edge. It is generally the first cavitation to occur on ship propellers. With higher loading, it is attached to the blade or sheet cavitation. Stable vortex cavitation is formed in the hub vortex combining the vortices shed from the blade roots. Vortex cavitation extended to the rudder can cause the erosion on the rudder surface. The collapsing of vortex cavitation extended to the rudder can cause the erosion of the rudder surface. For low advance ratio and small tip clearance, vortex cavitation can occur between a blade tip and the flat hull surface above the propeller. It is called as propeller-hull vortex cavitation.

The research of cavitating propellers generally involves model tests and computational methods for the purpose of predicting cavitation phenomena and controlling its negative effects. Model experiments are still considered more reliable. Computational methods for practical application of cavitating propellers are on development. A systematic approach to couple model test and computational method is desirable.

Empirical criteria for cavitation inception and thrust breakdown have been derived from experimental results and theoretical formulations. Burril's diagram, as one of the well-known criteria, is for assessing the sheet cavitation tendency as a function of thrust loading coefficient and local cavitation number for fixed pitch conventional propellers in uniform

inflow. Empirical criteria can be useful for rough estimation in the early stage of propeller design.

In computational methods, inviscid flow methods have many cases for the prediction of propeller cavitation, because it has long been used for the analysis of propeller flows. However, it has inherent limitations leading to quantitative disagreements with the experimental results due to the fact that cavitating flows are closely related to viscous flow effects such as turbulence flow, flow separation and vortex formation. On the other hand, the computational efficiency enables its repetitive application in the optimization algorithm of blade sections (Takekoshi et al., 2005). It may be prospective to couple an inviscid flow method with a viscous flow method for expensive computations such as full-scale computations including ship hull and other appendages.

Cavitation models in viscous flow methods have been developed in the last decade. They show the potential for the simulation of all types of cavitation with robustness, but they are to be more proved for the practical application of propeller cavitation. The up-to-date computations for cavitating propeller flows show reasonable agreements in sheet cavitation pattern, thrust, torque and cavitation inception with experimental results (Bensow, 2009, Lindau et al., 2002, Rhee et al., 2005). Further improvements and validations are still required for the simulation of cloud and vortex cavitations, which are the main source for erosion and broadband vibration.

1.6 Objectives and outline

The objective of the present work is

1. to investigate hydrodynamic and numerical characteristics of several cavitation models for a viscous flow solver,
2. to verify a cavitation model for the cavitation simulation on marine propellers as a complementary tool to the cavitation tunnel test and the other existing numerical methods.

Chapter 1 introduces general aspects of cavitation phenomenon including negative effects of cavitation on engineering devices, cavitation dynamics for a single spherical bubble and types of cavitating flows. Rayleigh-Plesset equation for bubble dynamics provides a theoretical basis for some of numerical models. The overview of numerical research on cavitation and the introduction of propeller cavitation are provided.

Chapter 2 presents the mathematical formulation and implementing procedure of the RANS solver and four cavitation models. The existing formulation for incompressible flows is modified into that for isothermal compressible flows with variable fluid properties depending

on the composition of two-phase fluid. The quantitative comparison of the mass transfer rate from the three cavitation models with a vapor transport equation is made. Numerical approximations for ensuring computational stability are described.

In Chapter 3, the validation of the implemented cavitation models is made for the cavitating flows on a 2D hydrofoil. The numerical results from the cavitation models are compared with the experimental results. The effects of numerical properties on steady and unsteady cavitation are investigated by numerical tests. The numerical tests and further validations are performed with one of the cavitation models proven in the 2D validation. Chapter 4 handles the validation for the cavitating flows on 3D hydrofoils. We consider non-swept and swept hydrofoils, resembling conventional and highly-skewed propellers, respectively, in hydrodynamic characteristics.

Chapter 5 is about the validation for the cavitating flows on a conventional and highly-skewed propellers in the open-water and behind-hull conditions. Instead of modeling the whole hull, the behind-hull wake field is applied to a plane upstream from the propeller by using the non-homogeneously loaded actuator disk. The effects of the Reynolds number on the numerical results are considered. Chapter 6 outlines the results and draws the conclusions.

This page is intentionally left blank.

Chapter 2

Mathematical formulation and implementation

2.1 Reynolds-Averaged Navier-Stokes equations

When the Navier-Stokes equations are merely solved for turbulent flows, the spatial and temporal resolutions are required to be high enough to capture the smallest scales of turbulent fluctuations. The number of degrees of freedom for resolving the largest length scale L and time scale T into the smallest ones η, τ is about $Rn_L^{11/4}$, based on the Kolmogorov scales $L/\eta \sim Rn_L^{3/4}, T/\tau \sim Rn_L^{1/2}$. The requirement for such computational effort makes it unfeasible for practical applications.

The common alternatives are the RANS model and large eddy simulation (LES). In RANS model, the complete turbulent components are estimated by a turbulence model, whereas the larger turbulent components are resolved and the smaller ones are modeled in LES. LES requires more computational effort, but it may achieve higher accuracy and robustness. Although the turbulence models are not well proved for cavitating flows, we implement a cavitation model in a RANS solver as a starting step. Since the in-house flow solver, EllipSys, used for this study, incorporates LES and DES as well as RANS, it has a possibility for further research on the cavitation model in LES and DES. See Michelsen (1994) and Sørensen (2003) for the details of mathematical formulation and implementation in EllipSys.

The RANS model is still the most popular tool for the simulation of turbulent flows in industrial applications of computational fluid dynamics (CFD). By the Reynolds decomposition and time averaging of the Navier-Stokes equations, we get the RANS equations, which are in

Cartesian coordinates for the isothermal compressible flows of a Newtonian fluid as follows

$$\frac{\partial \rho}{\partial t} + \frac{\partial}{\partial x_j}(\rho u_j) = 0 \tag{2.1}$$

$$\frac{\partial}{\partial t}(\rho u_i) + \frac{\partial}{\partial x_j}(\rho u_i u_j) - \frac{\partial}{\partial x_j}\left[\mu\left(\frac{\partial u_i}{\partial x_j} + \frac{\partial u_j}{\partial x_i}\right) - \rho\overline{u_i' u_j'}\right] + \frac{\partial p}{\partial x_i} = 0 \tag{2.2}$$

The variations of mean density are considered with ignoring the effects of density fluctuations. p includes the hydrostatic pressure i.e. $p = \tilde{p} + \rho_l g h$, where h is the water depth. To close the equations, the Reynolds stress tensor $\rho\overline{u_i' u_j'}$ is approximated by the eddy viscosity model and the momentum conservation equation (2.2) is rewritten with the eddy viscosity μ_t as follows

$$\frac{\partial}{\partial t}(\rho u_i) + \frac{\partial}{\partial x_j}(\rho u_i u_j) - \frac{\partial}{\partial x_j}\left[(\mu + \mu_t)\left(\frac{\partial u_i}{\partial x_j} + \frac{\partial u_j}{\partial x_i}\right)\right] + \frac{\partial p}{\partial x_i} = 0 \tag{2.3}$$

μ_t is specified by a two-equation model, which is more popular than the algebraic model and one-equation model. Among several two-equation models, we use the shear stress transport (SST) turbulence model of Menter (2003), which blends the $k-\epsilon$ model in the outer region and $k-\omega$ model in the near wall region to achieve higher accuracy of $k-\omega$ model in the near wall region and avoid the dependency of ω on the prescribed free stream value in the outer region. In the SST model, μ_t is defined by a function of the turbulent kinetic energy k and specific dissipation rate ω, and two transport equations are solved for k and ω, respectively. The definition of μ_t is modified for the multi-phase flow (Frikha et al., 2008). See Appendix A.1 for the details of the SST model with the modified definition of μ_t.

2.2 Cavitation models

For mixture fluid of liquid and vapor, we adopt the homogeneous equilibrium modeling (HEM) approach, which assumes that vapor is evenly dispersed in a finite volume of liquid, and hence velocity and pressure are equal between two phases inside each finite volume. The assumption enables us to treat the mixture fluid as a single pseudo-fluid with variable fluid properties corresponding to the composition of two phases. Since the velocity slip between two phases, ignored in the HEM, is rather small for high Reynolds number Rn and small vapor bubbles, the assumption for no velocity slip is a fair simplification for the cavitation in high Rn flows with tiny bubbles. The density ρ and viscosity μ of mixture fluid are averaged on a volume fraction basis, as in the volume-of-fluid method (Hirt & Nichols, 1981)

$$\rho = \alpha_v \rho_v + (1 - \alpha_v)\rho_l, \qquad \mu = \alpha_v \mu_v + (1 - \alpha_v)\mu_l \tag{2.4}$$

where α_v is the vapor volume fraction, which is the ratio of the vapor volume ΔV_v to the total volume ΔV of a finite volume i.e. $\alpha_v = \frac{\Delta V_v}{\Delta V}$, and the subscripts v and l indicate vapor and liquid, respectively.

The continuity equation for the vapor phase contains the mass transfer rate $\dot{m}$ per unit volume from the vapor to the liquid as a sink term, as follows

$$\frac{\partial}{\partial t}(\alpha_v \rho_v) + \frac{\partial}{\partial x_j}(\alpha_v \rho_v u_j) = -\dot{m} \tag{2.5}$$

It can be rewritten as follows

$$\frac{\partial \alpha_v}{\partial t} + u_j \frac{\partial \alpha_v}{\partial x_j} + \alpha_v \frac{\partial u_j}{\partial x_j} = \frac{D\alpha_v}{Dt} + \alpha_v \frac{\partial u_j}{\partial x_j} = -\frac{\dot{m}}{\rho_v} \tag{2.6}$$

Differentiating the equation (2.4) for ρ with respect to time, we have the relation of the material derivatives of ρ and α_v

$$\frac{D\rho}{Dt} = (\rho_v - \rho_l)\frac{D\alpha_v}{Dt} \tag{2.7}$$

Rewriting the continuity equation (2.1) for the mixture in a form of inhomogeneous divergence equation, we have the relation of the divergence of flow velocity to $\frac{D\rho}{Dt}$ and $\frac{D\alpha_v}{Dt}$

$$\frac{\partial u_j}{\partial x_j} = -\frac{1}{\rho}\frac{D\rho}{Dt} = \frac{\rho_l - \rho_v}{\rho}\frac{D\alpha_v}{Dt} \tag{2.8}$$

Applying the equation (2.8) to the equation (2.6), we have the relation of $\dot{m}$ to $\frac{D\alpha_v}{Dt}$

$$\dot{m} = -\frac{\rho_l \rho_v}{\rho}\frac{D\alpha_v}{Dt} \tag{2.9}$$

When we assume that vapor is distributed as a constant number density N of spherical microbubbles with the radius R, the vapor volume fraction α_v and its material derivative $\frac{D\alpha_v}{Dt}$ are expressed by

$$\alpha_v = \frac{4}{3}\pi R^3 N, \qquad \frac{D\alpha_v}{Dt} = 4\pi R^2 N \dot{R} = \frac{3\alpha_v}{R}\dot{R} \tag{2.10}$$

Applying the simplified solution (1.8) of the Rayleigh-Plesset equation for $\dot{R}$ and using the equation (2.9), $\dot{m}$ is rewritten as

$$\dot{m} = \pm\frac{3\rho_l \rho_v \alpha_v}{\rho R}\sqrt{\frac{2}{3}\frac{p_v - p}{\rho_l}\left[1 - \left(\frac{R_0}{R}\right)^3\right]} = \pm\frac{3\rho_l \rho_v \alpha_v}{\rho R}\sqrt{\frac{2}{3}\frac{p_v - p}{\rho_l}\left(1 - \frac{\alpha_{v0}}{\alpha_v}\right)} \tag{2.11}$$

We assume that a vapor grows or collapses rapidly, i.e. $R \to R_{\max}, \alpha_v \to 1, \rho \to \rho_v$ or $R \to R_{\min}, \alpha_v \to \frac{4}{3}\pi R_{\min}^3 N, \rho \to \rho_l$, but it does not collapse completely and R reduces to

a certain minimum value near to zero, because the equation is singular at $R = 0$. By the assumption, $\dot{m}$ is simplified to

$$\dot{m} = \begin{cases} -\frac{3\rho_l}{R_{\max}}\sqrt{\frac{2}{3}\frac{p_v - p}{\rho_l}}\sqrt{1-\alpha_{v0}} & = -C_e\sqrt{\frac{2}{3}\frac{p_v - p}{\rho_l}}\sqrt{1-\alpha_{v0}} \quad \text{for} \quad p < p_v \\ \rho_v\sqrt{12\pi R_{\min} N}\sqrt{\frac{2}{3}\frac{p - p_v}{\rho_l}}\sqrt{\alpha_{v0}} & = C_c\sqrt{\frac{2}{3}\frac{p - p_v}{\rho_l}}\sqrt{\alpha_{v0}} \quad \text{for} \quad p > p_v. \end{cases} \tag{2.12}$$

where C_e, C_c are constant coefficients.

In most cavitation models (Merkle et al., 1998, Kunz et al., 2000, Singhal et al., 2002, Lindenau and Bertram, 2003, Zwart et al., 2004, Kim and Brewton, 2008) in the HEM approach, the mass transfer is based on a transport equation identical or analogous to the equation (2.5). It is common for all these models that the mass transfer depends firsthand on the local pressure, the amount of liquid for evaporation or vapor for condensation and numerically-determined coefficients. We implement the three following models among them in EllipSys.

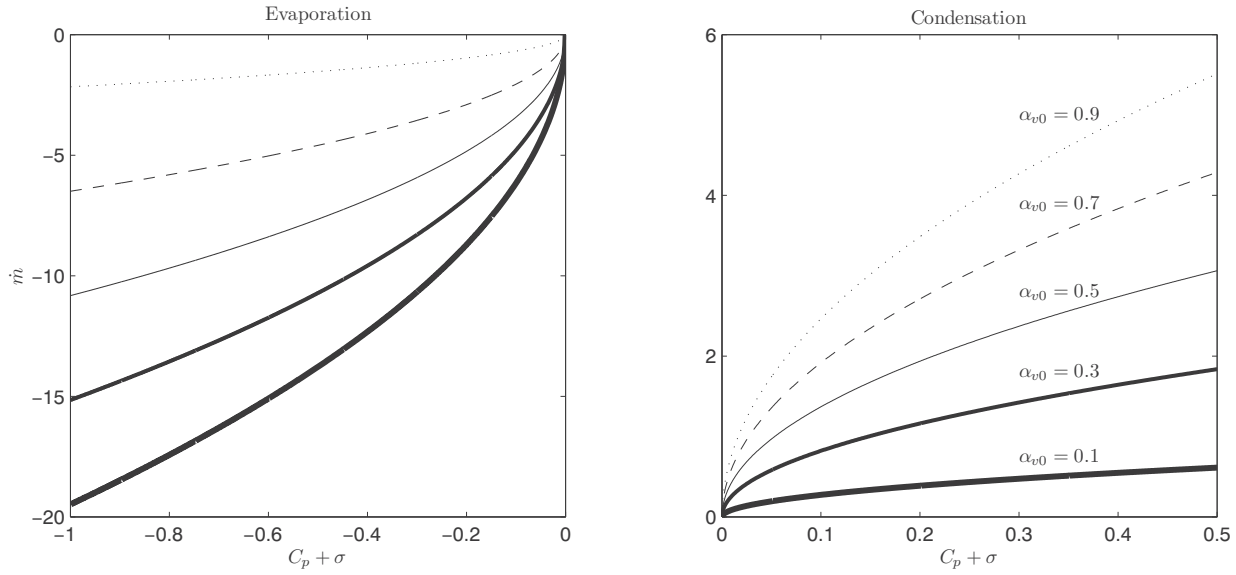

Figure 2.1: $\dot{m}$ as a function of $C_p + \sigma$ with varying α_{v0} for Model 1

Model 1

The cavitation model proposed by Zwart et al. (2004) uses the equation (2.5) as a vapor transport equation. Their definition of $\dot{m}$ is analogous to the equation (2.12), whereas the direct proportionality of $\dot{m}$ to the volume fraction of liquid for evaporation is not mathematically derived, but it is added by a physical reasoning that the nucleation site density for

evaporation must decrease accordingly, as α_v increases. The nucleation site volume fraction r_{nuc} and the nucleation-site radius R_B are constants. $\dot{m}$ is defined by

$$\dot{m} = \begin{cases} -C_e \frac{3 r_{nuc} \rho_v}{R_B} \sqrt{\frac{2}{3} \frac{p_v - p}{\rho_l}} (1 - \alpha_{v0}) & \text{for} \quad p < p_v \\ C_c \frac{3 \rho_v}{R_B} \sqrt{\frac{2}{3} \frac{p - p_v}{\rho_l}} \alpha_{v0} & \text{for} \quad p > p_v. \end{cases} \tag{2.13}$$

As shown in Figure 2.1, the absolute values of $\dot{m}$ in evaporation are about $3 \sim 4$ times larger than those in condensation for the same absolute value of $C_p + \sigma$, where C_p is the pressure coefficient, $C_p = \frac{p - p_\infty}{0.5 \rho_l U_\infty^2}$, σ is the cavitation number in Eq.(1.1). The coefficients applied for the computations with Model 1 in the next chapters, are used for Figure 2.1.

Model 2

In the model proposed by Singhal et al. (2002), the mass transfer is governed by a generic transport equation for the vapor mass fraction f with an addition term for turbulent diffusion as follows

$$\frac{\partial}{\partial t}(\rho f) + \frac{\partial}{\partial x_j}(\rho u_j f) - \frac{\partial}{\partial x_j}\left(\frac{\mu_t}{Pr_v} \frac{\partial f}{\partial x_j}\right) = -\dot{m} \tag{2.14}$$

where Pr_v is the turbulent Prandtl number for the vapor, $Pr_v = 0.7 \sim 1.0$ (Rhee et al., 2005).

The vapor mass fraction f is related to the vapor volume fraction α_v by $\rho f = \rho_v \alpha_v = \frac{\Delta m_v}{\Delta V}$, where Δm_v is the vapor mass in a finite volume. This relation explains the similarity of the equation (2.14) to the equation (2.5).

To account for the turbulent fluctuations of velocity and pressure, the turbulent kinetic energy k is included in the definition of $\dot{m}$, and the threshold pressure p_v^* for the phase change is obtained by adding the turbulent pressure fluctuation to the vapor pressure i.e. $p_v^* = p_v + 0.195 \rho k$. $\dot{m}$ is defined by

$$\dot{m} = \begin{cases} -C_e \frac{\sqrt{k}}{T} \rho_l \rho_v \sqrt{\frac{2}{3} \frac{p_v^* - p}{\rho_l}} (1 - f_0) & \text{for} \quad p < p_v^* \\ C_c \frac{\sqrt{k}}{T} \rho_l^2 \sqrt{\frac{2}{3} \frac{p - p_v^*}{\rho_l}} f_0 & \text{for} \quad p > p_v^* \end{cases} \tag{2.15}$$

where T is the surface tension.

Model 3

In the model proposed by Kunz et al. (2000), the mass transfer is governed by the continuity equation for the liquid phase

$$\frac{\partial}{\partial t}(\alpha_l \rho_l) + \frac{\partial}{\partial x_j}(\alpha_l \rho_l u_j) = \dot{m} \tag{2.16}$$

As $\dot{m}$ works as a source for the liquid phase and as a sink for the vapor phase, the total mass is conserved in the mixture fluid. The characteristic velocity U_∞ and time scale t_∞ are included in the definition of $\dot{m}$

$$\dot{m} = \frac{C_e \rho_v \alpha_{l0} \min(0, p - p_v)}{0.5 \rho_l U_\infty^2 t_\infty} + \frac{C_c \rho_v \alpha_{l0}^2 (1 - \alpha_{l0})}{t_\infty} \tag{2.17}$$

The evaporation is linear in $p_v - p$ and the condensation is not related to p, whereas the mass transfer between two phases is proportional to $\sqrt{|p - p_v|}$ as Model 1 and 2.

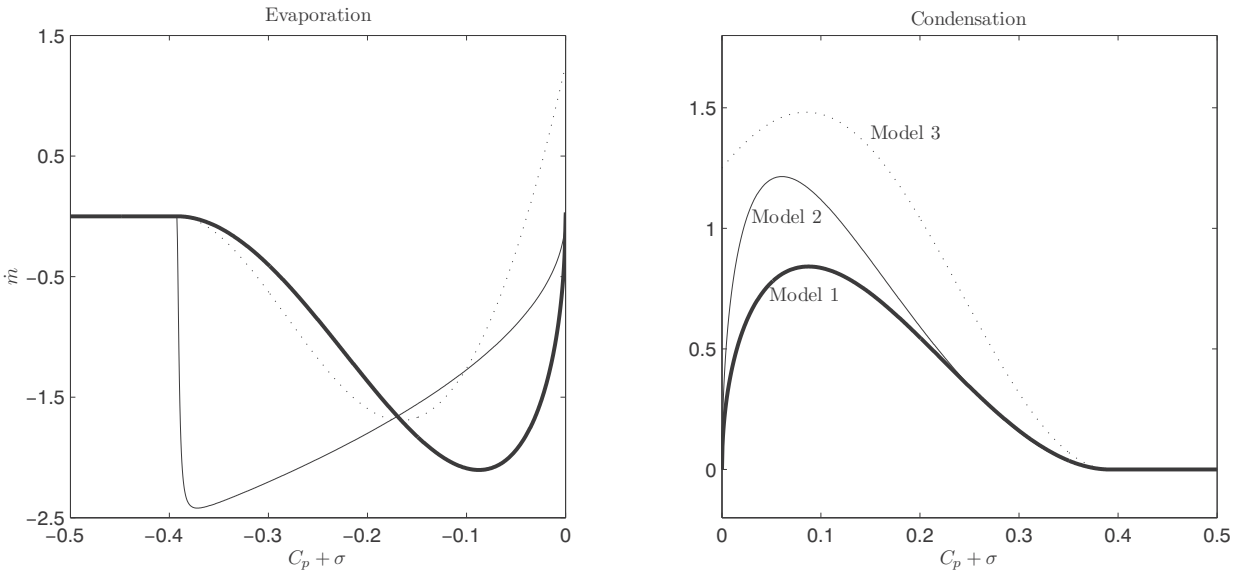

Figure 2.2: The comparison of $\dot{m}$ from three cavitation models based on a transport equation

In Figure 2.2, the quantities of $\dot{m}$ from the three models with a transport equation are compared. The vapor fraction in the previous iteration is approximated by coupling it with p via the barotropic state law in Model 4 introduced later. The coefficients applied for the computations in the next chapters are used. $\sqrt{k}$ in Model 2 is approximated by $5 \cdot 10^{-2} U_\infty$ in condensation and $5 \cdot 10^{-4} U_\infty$ in evaporation, because for example the flow in the fore evaporating part of a sheet cavity is less turbulent than in the aft closing part.

$\dot{m}$ from all three models is in a similar range. In evaporation, the distribution of $\dot{m}$ from Model 2 has a different pattern. The transport equation (2.14) in Model 2 is concerned with ρf and it is solved for f, taking ρ from the previous iteration. The transport equations (2.5) and (2.16) in Model 1 and 3 handle $\rho_v \alpha_v$ and $\rho_l \alpha_l$, respectively, and ρ_v, ρ_l are constants. ρ from the previous iteration in Model 2 can lead to the different distribution of $\dot{m}$ in evaporation, because ρ can be suddenly changed by evaporation. When ρ is not directly coupled with f, the transport equation for f can have a different distribution of the source term.

In Figure (2.3) (left), the relation between f and α_v is presented for the density ratio between liquid and vapor of $\rho_l/\rho_v = 40000$. The magnitude of f is quite different from α_v at the same mixture density due to the high density ratio e.g. $f \simeq 0.0005 \rightarrow \alpha_v \simeq 0.95$. Such a difference of f from α_v may lead to a different distribution of $\dot{m}$.

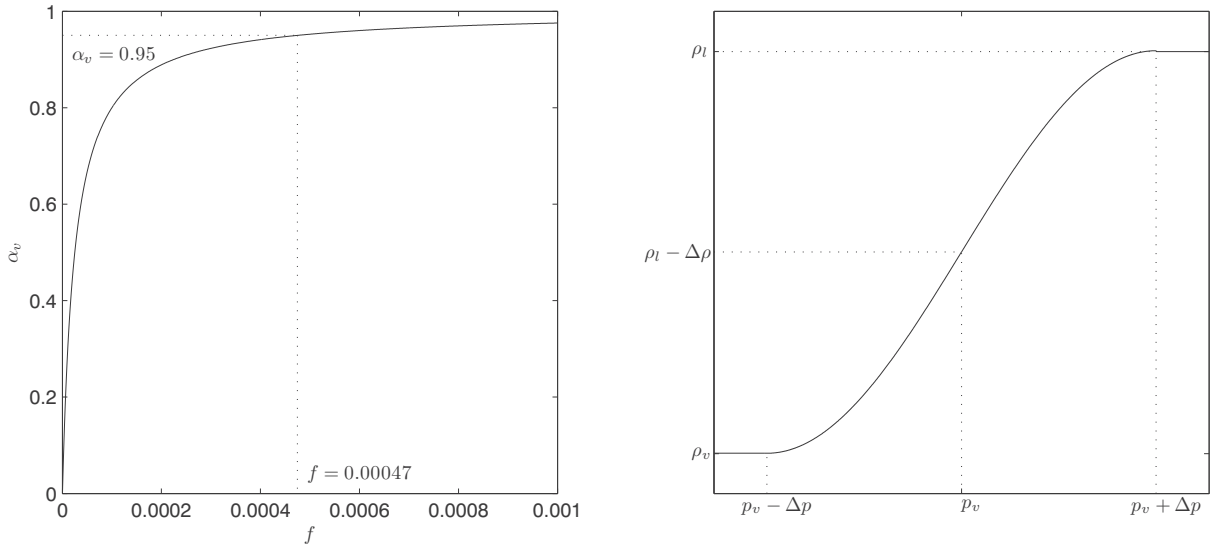

Figure 2.3: The relation between f and α_v (left) and ρ as a function of p by a barotropic state law for the mixture fluid (right)

Model 4

In several cavitation models (Hoeijmakers et al., 1998, Coutier-Delgosha et al., 2003), the mass transfer is based on a barotropic state law, which links the mixture density directly to the local static pressure without a vapor transport equation. In the transition region around p_v, the mixture fluid is treated as a compressible mixture, of which the sound speed a is minimum for a half-and-half mixture and it increases exponentially, as the mixture becomes closer to the pure liquid or vapor. a is related to the pressure derivative with respect to the mixture density by

$$a = \sqrt{\frac{dp}{d\rho}} \tag{2.18}$$

The variation of a according to the mixture composition resembles its physical property in a mixture fluid and it enables the smooth transition between two phases in the numerical

model. The barotropic state law proposed by Hoeijmakers et al. (1998) is

$$\rho(p) = \begin{cases} \rho_l & \text{for} \quad p > p_v + \Delta p \\ \rho_v & \text{for} \quad p < p_v - \Delta p \\ \rho_v + \Delta\rho \left[1 + \sin\left(\frac{p-p_v}{\Delta\rho a_{\min}^2}\right)\right] & \text{elsewhere} \end{cases} \tag{2.19}$$

As shown in Figure 2.3, the minimum sound speed $a_{\min}$ determines the maximum slope i.e. $(d\rho/dp)_{\max} = 1/a_{\min}^2$, and the width of the transition region is inversely proportional to the maximum slope by the relation $\Delta p = 0.5\pi a_{\min}^2 \Delta\rho$.

2.3 Implementation

While EllipsSys uses general curvilinear coordinates for complex geometries, the following implementing procedure is presented in Cartesian coordinates to avoid complication in mathematical expressions from transforming the coordinate system. See Sørensen (2003) and Michelsen (1998) for the transformation from Cartesian or cylindrical coordinates into general curvilinear ones. EllipSys is parallelized by using the multi-block topology and the Message Passing Interface (MPI).

Momentum conservation equation

Adopting the finite volume method, the fluid domain is divided into finite volumes and the partial differential equations are integrated on each finite volume ΔV. Using the divergence theorem, the volume integral of a divergence term is converted to a surface integral. The integral form of the momentum conservation equation (2.3) is

$$\int_{\Delta V} \frac{\partial}{\partial t}(\rho u_i) dV + \oint_{\Delta A_j} \rho u_i u_j \, dA - \oint_{\Delta A_j} \left[(\mu + \mu_t)\left(\frac{\partial u_i}{\partial x_j} + \frac{\partial u_j}{\partial x_i}\right)\right] dA + \oint_{\Delta A_i} p \, dA = 0 \tag{2.20}$$

where ΔA_i is the projected surface area perpendicular to the i-direction.

The temporal domain is discretized by the time step Δt. The time-derivative term in Eq.(2.20) is approximated as follows

$$\int_{\Delta V} \frac{\partial}{\partial t}(\rho u_i) dV \simeq \frac{\Delta V_P}{\Delta t}\left[(\rho u_i)_P^{t+\Delta t} - (\rho u_i)_P^t\right] \tag{2.21}$$

The superscript $t + \Delta t$ indicates the value treated implicitly and t indicate the values known from the previous time step. $\rho^{t+\Delta t}$ is found from the cavitation model before solving the momentum equation. Based on the collocated grid arrangement, all variables are evaluated

in the centre of each finite volume except for the mass flux. Each finite volume consists of six plane faces, of which the central nodes are denoted by lower-case letters w, e, s, n, b, t according to their direction from the central node P of ΔV_P. The central nodes of neighboring finite volumes are denoted by upper-case letters W, E, S, N, B, T.

To obtain a linearized equation, the mass flux $\int_{\Delta A_j} \rho u_j dA$ in the convective term is taken from the previous time step. The mass flux on the face is approximated by the Rhie-Chow method, which is dealt with later in the pressure correction equation. The convective velocity on the face is approximated by the first-order upwind differencing scheme (UDS), because high-order schemes can bring oscillations in the density profile in the vicinity of sharp density gradients, which lead to numerical instability (Senocak and Shyy, 2004). As an example, the convective term for a one-dimensional flow perpendicular to the western and eastern faces are

$$\oint_{\Delta A_w+\Delta A_e} \rho u_i u_j \, dA = \max[0, (\rho u \Delta A)_w^t] \cdot (u_P^{t+\Delta t} - u_W^{t+\Delta t}) + \min[0, (\rho u \Delta A)_e^t] \cdot (u_E^{t+\Delta t} - u_P^{t+\Delta t}) \tag{2.22}$$

While the normal diffusive term is treated implicitly, the cross diffusive term is explicitly evaluated with the velocity field from the previous time step. Both diffusive terms are approximated by the central differencing scheme (CDS). The viscosity is linearly interpolated. The normal diffusive term for a velocity component is

$$\oint_{\Delta A_w+\Delta A_e} \left[(\mu + \mu_t) \frac{\partial u}{\partial x} \right] dA = \frac{\mu_E + \mu_P}{\Delta V_E + \Delta V_P} \Delta A_e^2 (u_E^{t+\Delta t} - u_P^{t+\Delta t}) - \frac{\mu_P + \mu_W}{\Delta V_P + \Delta V_W} \Delta A_w^2 (u_P^{t+\Delta t} - u_W^{t+\Delta t}) \tag{2.23}$$

where μ_E, μ_P, μ_W are the sum of μ and μ_t at each node.

The pressure term is explicitly evaluated with the pressure field from the previous time step. The pressure term for a one-dimensional flow is

$$\oint_{\Delta A_w+\Delta A_e} p \, dA = \frac{1}{2}(p_E^t \Delta A_e - p_W^t \Delta A_w) + \frac{p_P^t}{2}(\Delta A_e - \Delta A_w) \tag{2.24}$$

Collecting the coefficient of the velocity component on each node and the explicit terms excluding the time-derivative term (2.21), we have a linearized algebraic equation for a steady-state computation

$$A'_{u_i,P} \cdot u_{i,P} + \sum_{nb} A_{u_i,nb} \cdot u_{i,nb} = S'_{u_i} \tag{2.25}$$

where the subscript nb denotes the central nodes of the neighboring cells.

To avoid numerical instability, the changing rate from the result $u^*_{i,P}$ in the previous iteration is slowed down by an under-relaxation factor α_{u_i} as follows

$$\frac{A'_{u_i,P}}{\alpha_{u_i}} \cdot u_{i,P} + \sum_{nb} A_{u_i,nb} \cdot u_{i,nb} = S'_{u_i} + \frac{1-\alpha_{u_i}}{\alpha_{u_i}} A'_{u_i,P} u^*_{i,P} \tag{2.26}$$

For a unsteady-state computation, the time-derivative term (2.21) is added to the central node coefficient and the source term as follows

$$\underbrace{\left(\frac{A'_{u_i,P}}{\alpha_{u_i}} + \frac{\Delta V_P}{\Delta t}\rho_P\right)}_{A_{u_i,P}} \cdot u^{t+\Delta t}_{i,P} + \sum_{nb} A_{u_i,nb} \cdot u^{t+\Delta t}_{i,nb} = \underbrace{S'_{u_i} + \frac{1-\alpha_{u_i}}{\alpha_{u_i}} A'_{u_i,P} u^*_{i,P} + \frac{\Delta V_P}{\Delta t}\rho_P u^t_{i,P}}_{S_{u_i}} \tag{2.27}$$

The linear equation is solved by the red-black Gauss-Seidel method (Saad, 2003). The velocity field at an inlet boundary is specified by the Dirichlet boundary condition (BC). The outlet velocity field has a zero-gradient condition of the Neumann type for a steady-state computation and a convective BC for an unsteady-state one. The outlet mass flux is scaled from the inlet mass flux to fulfill the global mass conservation. The wall boundary has the no-slip condition. See Appendix A.2 for the implementation of boundary conditions.

Pressure correction equation

Since the result from solving the momentum equations does not fulfill the continuity equation, the pressure field is corrected to satisfy this equation. To make the continuity equation (2.8) coupled with the vapor transport equation, the term in the right-hand side is rewritten with $\dot{m}$ by the relation (2.9). The integral form of the continuity equation is

$$\oint_{\Delta A_j} u_j \, dA = \int_{\Delta V} \left(\frac{1}{\rho_l} - \frac{1}{\rho_v}\right) \dot{m} \, dV \tag{2.28}$$

Since the linear interpolation of the pressure field in Eq.(2.24) does not account for the pressures on the alternate nodes, it can lead to the oscillatory pressure field. To avoid this problem, the mass/volume fluxes are approximated by the Rhie-Chow method. As an example, the sum of the volume fluxes for a one-dimensional flow is

$$\begin{aligned}\oint_{\Delta A_w + \Delta A_e} u'' \, dA = {} & \Delta A_e \left[\left(\frac{1}{A_{u,P}}(\tilde{S}_u - \sum_{nb} A_{u,nb} \cdot u''_{nb})\right)_e + \left(\frac{1}{A_{u,P}}\right)_e \Delta A_e (p''_E - p''_P)\right] \\ & - \Delta A_w \left[\left(\frac{1}{A_{u,P}}(\tilde{S}_u - \sum_{nb} A_{u,nb} \cdot u''_{nb})\right)_w + \left(\frac{1}{A_{u,P}}\right)_w \Delta A_w (p''_P - p''_W)\right]\end{aligned} \tag{2.29}$$

where $\tilde{S}_u$ is the source term excluding the portion from the pressure term and the value on the face is linearly interpolated.

In the approximation of the mass flux, the velocity portion without the pressure-gradient effect is multiplied by the density before the interpolation. Since the pressure gradient is approximated on the face, $\frac{\rho}{A_{u_i,P}}$ is interpolated on the face and afterwards it is multiplied by the pressure gradient on the face, as follows

$$\begin{aligned}\oint_{\Delta A_w+\Delta A_e} \rho u'' \, dA = \Delta A_e \left[\left(\frac{\rho}{A_{u,P}} (\tilde{S}_u - \sum_{nb} A_{u,nb} \cdot u''_{nb}) \right)_e + \left(\frac{\rho}{A_{u,P}} \right)_e \Delta A_e (p''_E - p''_P) \right] \\ - \Delta A_w \left[\left(\frac{\rho}{A_{u,P}} (\tilde{S}_u - \sum_{nb} A_{u,nb} \cdot u''_{nb}) \right)_w + \left(\frac{\rho}{A_{u,P}} \right)_w \Delta A_w (p''_P - p''_W) \right]\end{aligned} \tag{2.30}$$

When the velocity and pressure fields with double primes in Eq.(2.29) fulfill the continuity equation and there is no mass transfer between phases yet, Eq.(2.29) is equal to zero. When u''_i and p'' consist of the predicted part with a prime from the momentum equations and the corrected one with the superscript c, Eq.(2.29) can be rewritten as follows

$$\begin{aligned}\Delta A_e \left[\left(\frac{1}{A_{u,P}} (\tilde{S}_u - \sum_{nb} A_{u,nb} \cdot (u'_{nb} + u^c_{nb})) \right)_e + \left(\frac{1}{A_{u,P}} \right)_e \Delta A_e (p'_E + p^c_E - p'_P - p^c_P) \right] \\ -\Delta A_w \left[\left(\frac{1}{A_{u,P}} (\tilde{S}_u - \sum_{nb} A_{u,nb} \cdot (u'_{nb} + u^c_{nb})) \right)_w + \left(\frac{1}{A_{u,P}} \right)_w \Delta A_w (p'_P + p^c_P - p'_W - p^c_W) \right] = 0\end{aligned} \tag{2.31}$$

Based on the SIMPLE method, u^c_i is neglected. By the iterations of solving for the corrected pressure and updating the velocity field accordingly, the neglected portion is decreased. Assembling the coefficient of p^c on each node and the explicit terms in Eq.(2.31), we have a linear equation

$$A'_{p,P} \cdot p^c_P + \sum_{nb} A_{p,nb} \cdot p^c_{nb} = S'_p \tag{2.32}$$

When a mass transfer occurs, the pressure correction equation needs to include the effect of the mass transfer. $\dot{m}$ is dependent on both p' and p^c. Since p^c is small compared to p', the contribution to $\dot{m}$ from p^c is approximated by multiplying p^c and the pressure derivative of $\dot{m}$ at p' (Maquil, 2007). The term on the right-hand side of Eq.(2.28) is approximated by

$$\int_{\Delta V} \left(\frac{1}{\rho_l} - \frac{1}{\rho_v} \right) \dot{m} \, dV = \left(\frac{1}{\rho_l} - \frac{1}{\rho_v} \right) \left(\dot{m}' + p^c_P \left(\frac{\partial \dot{m}}{\partial p} \right)' \right) \Delta V_P \tag{2.33}$$

where the prime on $\dot{m}$ and $\frac{\partial \dot{m}}{\partial p}$ indicates that those values are evaluated with p'.

Adding the mass transfer term (2.33) to the linear equation (2.32), it becomes

$$\underbrace{(A'_{p,P} + \left(\frac{1}{\rho_l} - \frac{1}{\rho_v}\right)\left(\frac{\partial \dot{m}}{\partial p}\right)' \Delta V_P)}_{A_{p,P}} \cdot p^c_P + \sum_{nb} A_{p,nb} \cdot p^c_{nb} = \underbrace{S'_p - \left(\frac{1}{\rho_l} - \frac{1}{\rho_v}\right)\dot{m}'}_{S_p} \tag{2.34}$$

The value of $\frac{\partial \dot{m}}{\partial p}$ is always positive, as shown in Figure 2.4. Since the additional term in $A_{p,P}$ always has the same sign as $A'_{p,P}$, $A_{p,P}$ is increased. It brings a positive effect on numerical stability. Imitating Model 1 and 2 without a mathematical derivation, $\frac{\partial \dot{m}}{\partial p}$ for Model 4 is defined with a coefficient C_b, which is obtained by numerical tests (See Appendix A.3). $\frac{\partial \dot{m}}{\partial p}$ for each cavitation model is defined by

$$\frac{\partial \dot{m}}{\partial p} = \begin{cases} \frac{\dot{m}}{2(p-p_v)} & \text{Model 1 and 2} \\ \frac{C_e \rho_v \alpha_l}{0.5 \rho_l U_\infty^2 t_\infty} & \text{for} \quad p < p_v, \quad 0 \quad \text{for} \quad p \geq p_v \quad \text{Model 3} \\ \left|\frac{C_b \dot{m}}{p-p_v}\right| & \text{Model 4} \end{cases} \tag{2.35}$$

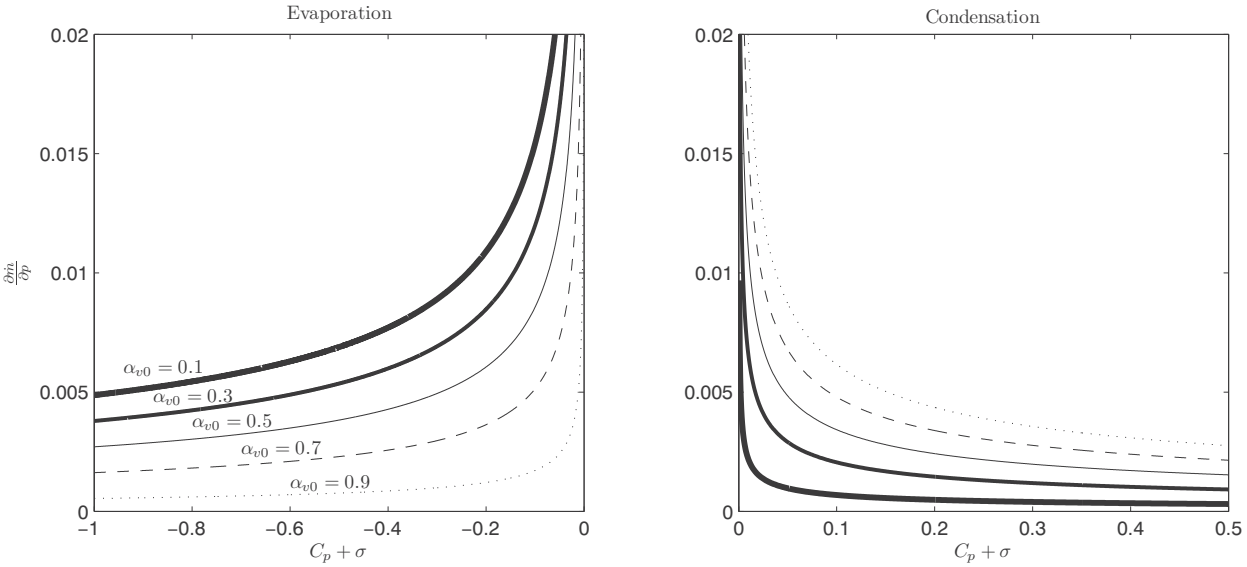

Figure 2.4: $\frac{\partial \dot{m}}{\partial p}$ as a function of $C_p + \sigma$ with varying α_{v0} for Model 1

The linear equation (2.34) for the pressure correction is solved by a five-level multigrid method combined with the Schwarz Alternating Method (SAM) and the Incomplete Line Lower-Upper (ILLU) factorization. P^c at a boundary has a zero-gradient condition of the Neumann type, whereas p is extrapolated from the known inner values.

Cavitation models

For the first three models, a transport equation is solved in the same way as the momentum conservation equation. Although Model 1 and 3 originally do not contain a normal diffusive term, numerical stability can be improved by inserting this term with a large value of Pr_v e.g. $Pr_v = 1000$. p from the pressure correction is applied to the source term. As in the cavitation tunnel test, the cavitation number σ is gradually decreased to a prescribed value. The vapor pressure p_v is calculated from σ. The value known in the previous iteration is applied to the variable with a subscript 0 in the source term. While the vapor fraction at an inlet is specified, it has a zero-gradient condition at wall and outlet boundaries.

The mixture properties are updated by Eq.(2.4). To avoid numerical instability due to high density gradients, smoothing is performed on ρ and μ by averaging surrounding nodal values.

For Model 4 with a barotropic state law, ρ is directly linked to p by Eq.(2.19). $\dot{m}$ is computed by Eq.(2.5) with α_v updated according to ρ. After reaching the prescribed ρ, a_{min} is gradually decreased e.g. from 1 to 0.5 in order to achieve a sharp interface while maintaining numerical stability.

The converged steady-state solution for a non-cavitating flow is restarted and cavitation is induced by reducing σ. Since the residuals in cavitating flow solutions are generally larger than those in non-cavitating flow ones, the program is terminated by a specified maximum number of iterations or a time span rather than convergence criteria. The overall solution procedure is summarized as follows

Time stepping : $t \rightarrow t + \Delta t$

Outer iteration

$u_i, \rho, \mu, \mu_t, k, \omega$	$\rightarrow$	$k-\omega$ SST turbulence model	$\rightarrow$	k, ω	$\rightarrow$	μ_t
$p, u_i, \rho, \alpha_v, f, (\mu_t, k)$	$\rightarrow$	Cavitation model	$\rightarrow$	$\alpha_v, f, \dot{m}$	$\rightarrow$	ρ, μ
p, u_i, ρ, μ, μ_t	$\rightarrow$	Momentum conservation equation	$\rightarrow$	u_i		

Pressure iteration

$p, u_i, \dot{m}$	$\rightarrow$	Pressure correction equation	$\rightarrow$	p	$\rightarrow$	u_i

This page is intentionally left blank.

Chapter 3

Cavitating flows on a 2D hydrofoil

The first validation of the implemented cavitation models is performed for the cavitating flows on a 2D hydrofoil. The section model and flow condition follow those in the experiment of Shen and Timotakis (1989).

3.1 Hydrofoil model and flow condition

The section model is NACA66 with a mean-line of $a = 0.8$ (mod), a camber ratio of $f_{\max}/C = 0.02$ and a thickness ratio of $t_{\max}/C = 0.09$, where $f_{\max}$ is the maximum camber, C is the chord length and $t_{\max}$ is the maximum thickness. While a hydrofoil with $0.1524m$ span and $0.1524m$ chord dimensions is tested in a $1.27m$ long, $0.762m$ high and $0.1524m$ wide water tunnel, the chord length in a 2D meshed grid for the computations is $1m$ and an inflow velocity is adjusted to reach the same Reynolds number as in the experiment. Since roughness is applied on both surfaces of the experimental model from the leading edge to $0.015C$ to reduce the scale effects, the scale of the computational model is increased. Two cases with different angles α of attack and Reynolds numbers Rn are considered: $\alpha = 4^o, Rn = 2 \cdot 10^6$ and $\alpha = 1^o, Rn = 3 \cdot 10^6$.

As shown in Figure 3.1, an O-type grid consisting of 32768 cells is generated with a radial extent of $6C$. By using the tanh function for stretching the grid size $\Delta\eta$ along the radius, $\Delta\eta$ is gradually increased in the near-field region and almost constant in the far-field. The grid size $\Delta\xi$ along the hydrofoil surface is defined to be relatively small at the leading and trailing edge. The height of first cells from the wall is $\Delta h = 3 \cdot 10^{-5}$, resulting in $y^+ \leq 2$, where y^+ is the dimensionless wall distance, $y^+ = \frac{\rho_l d\, u_\tau}{\mu_l}$, where d is the distance from the wall to the first-cell centre and u_τ is the friction velocity. The effects of Δh on the result will be investigated later in this chapter.

In a fully wetted flow condition i.e. at a sufficiently high value of σ, steady-state computations are performed to be converged until the maximum normalized residual $r_{\max}$ for velocity

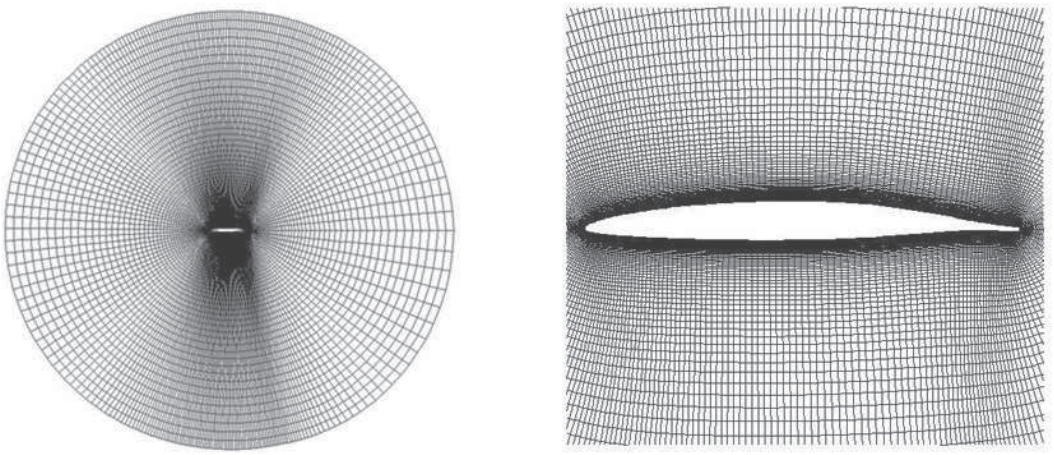

Figure 3.1: Computational grid and close-up view around a hydrofoil section

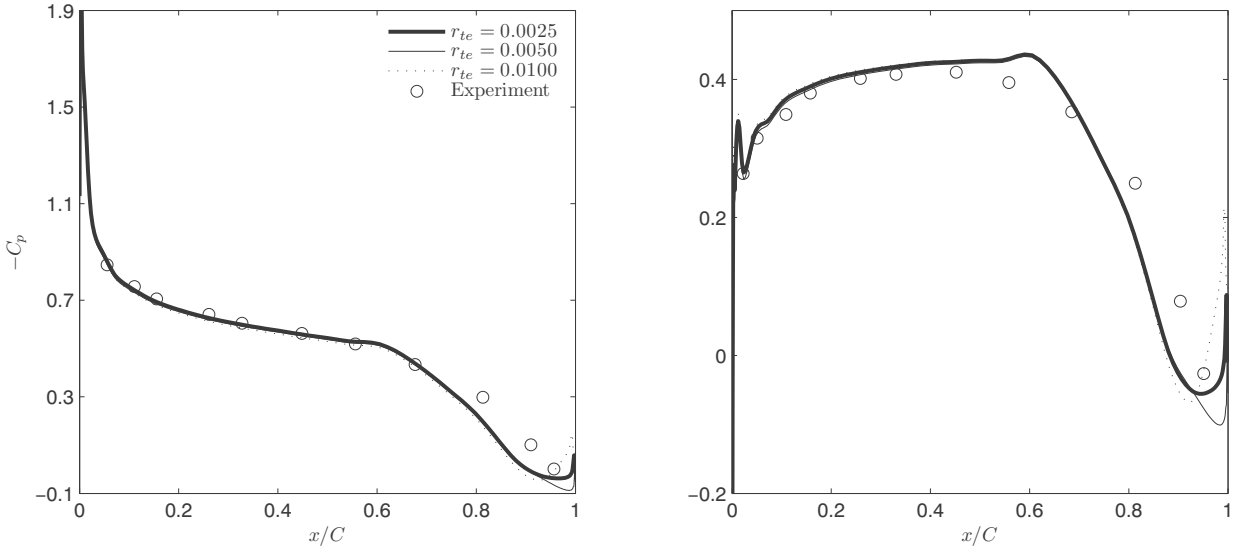

Figure 3.2: Pressure coefficient on the suction side for $\alpha = 4^o$ (left) and $\alpha = 1^o$ (right) with varying r_{te} in a fully wetted flow

	α	Re	Experiment	$r_{te} = 0.0025$	$r_{te} = 0.0050$	$r_{te} = 0.0100$
C_L	4^o	$2 \cdot 10^6$	0.6290	0.6628	0.6769	0.6860
C_D	4^o	$2 \cdot 10^6$	0.01800	0.01750	0.01836	0.02084
C_L	1^o	$3 \cdot 10^6$	0.3062	0.3485	0.3568	0.3641
C_D	1^o	$3 \cdot 10^6$	0.01390	0.01247	0.01324	0.01537

Table 3.1: C_L and C_D from the computation and the experiment in a fully wetted flow

components and pressure drops below 10^{-3}. As shown in Figure 3.2, the pressure distribution on the suction side shows a good agreement with that from the experiment except the trailing-edge region. The variation of the trailing-edge radius r_{te} does not improve agreement significantly. Other 2D computations (Singhal et al., 2002, Rhee et al., 2005) also show such quantitative differences from the 3D experimental results.

As shown in Table 3.1, the lift coefficient C_L from the computation has a difference of $5-9\%$ and $14-19\%$ from that from the experiment for $\alpha = 1^o$ and $\alpha = 4^o$, respectively. The drag coefficient C_D has a difference of $2-16\%$ and $5-11\%$. Such differences may be due to the limitation of 2D computations. C_L and C_D are defined by

$$C_L = \frac{L}{0.5\rho_l U_\infty^2 C}, \qquad C_D = \frac{D}{0.5\rho_l U_\infty^2 C} \tag{3.1}$$

where L and D are the lift and drag per unit span, respectively.

C_p, C_L and C_D for $r_{te} = 0.005C$ are mostly closer to the experimental ones than those for two other r_{te}. We proceed to the following computations with $r_{te} = 0.005C$.

3.2 Numerical results

For two cases of cavitating flow, the numerical results from the four implemented cavitation models are compared. Unsteady-state computations are performed except for Model 4, which has a stability problem in unsteady-state computations and hence steady-state computations are made for this model. The time step is set to $\Delta t = 2.5 \cdot 10^{-4} C/U_\infty$. The under-relaxation factor is $\alpha_u = 0.6$ for the momentum conservation equation, $\alpha_p = 0.1$ for the pressure correction, $\alpha_k = \alpha_\omega = 0.7$ for the turbulence model equations and $\alpha_{cav} = 0.1$ for the vapor fraction. The iteration number n_{it} at each time step is set to 1, because each iteration in steady-state computations can have a transient nature for unsteady cavitation, as shown in Figure 3.5 (right). The effects of each numerical property like Δt, α_{cav} and n_{it} will be investigated in the next section. The coefficient values applied to the definition of $\dot{m}$ are determined to achieve stability by numerical tests, as shown in Table 3.2.

	Model 1	Model 2	Model 3	Model 4
C_e , C_c	0.5 , 10^{-4}	10 , 0.2	2500 , 400	$a_{min} = 0.5$

Table 3.2: The coefficient values for the cavitation models

As shown in Figure 3.3, the solutions for $\alpha = 4^o, \sigma = 0.91$ from all models are converged with $r_{\max} < 10^{-3}$. In the solution from Model 2, V_v has irregular fluctuations, which correspond to cavity length variation of less than $0.001C$ and are not so influential on the overall flow.

For $\alpha = 1^o, \sigma = 0.38$, the cavity length L_c is in a periodic variation with the amplitude of about $0.1C$ for the first three models and about $0.03C$ for Model 4. The Strouhal number

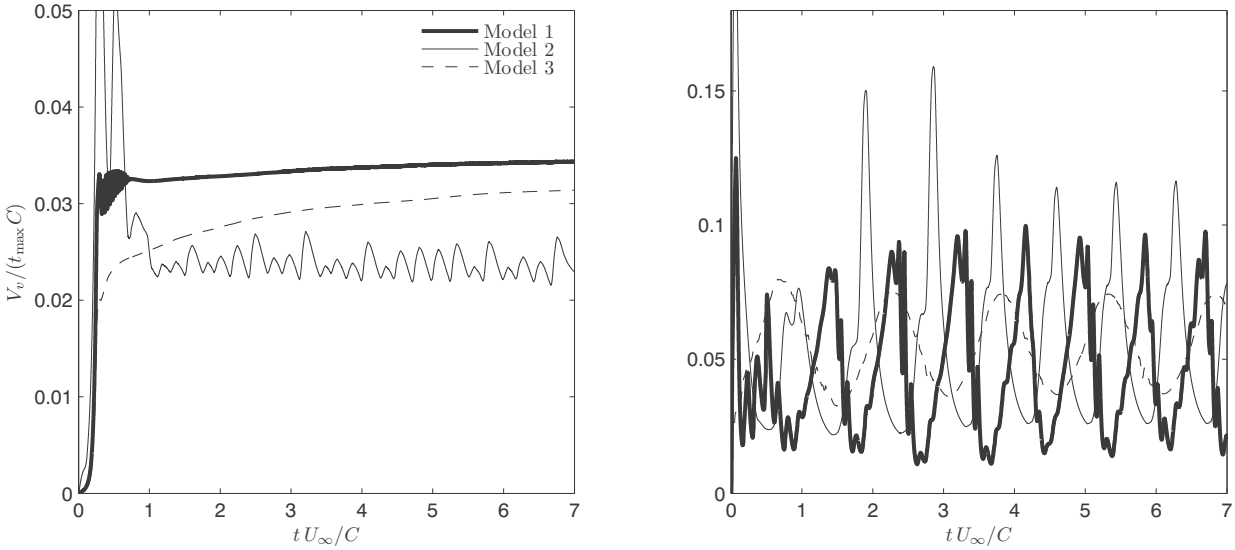

Figure 3.3: Total vapor volume as a function of time in unsteady-state computation for $\alpha = 4^o, \sigma = 0.91$ (left) and $\alpha = 1^o, \sigma = 0.38$ (right)

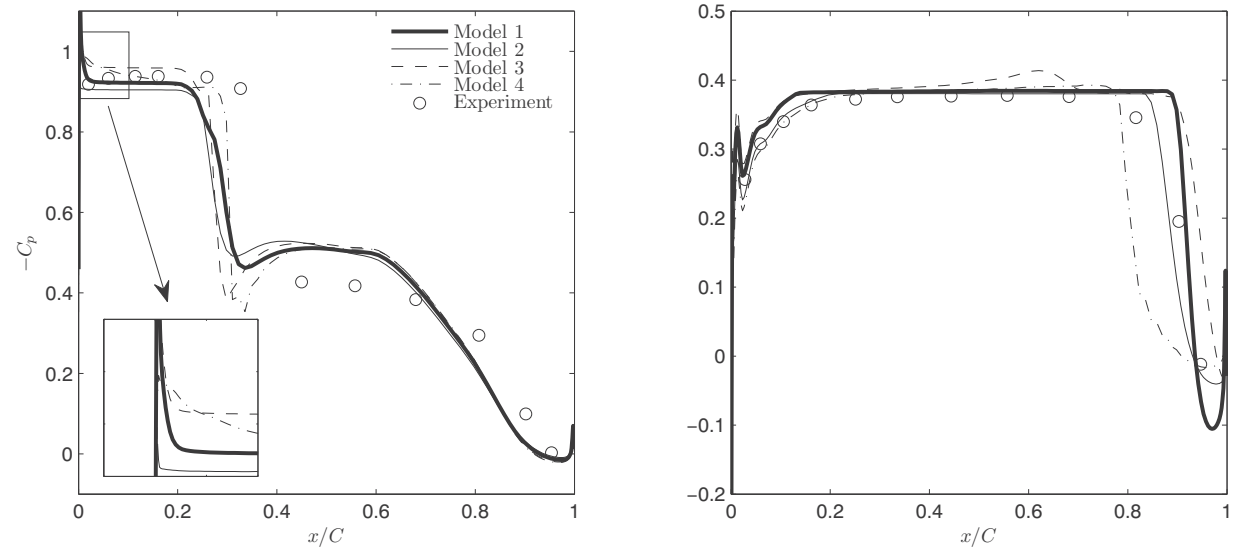

Figure 3.4: Pressure coefficient on the suction side for $\alpha = 4^o, \sigma = 0.91$ (left) and $\alpha = 1^o, \sigma = 0.38$ (right)

St in unsteady-state computation is 0.296, 0.297, 0.167 for Model 1, 2 and 3, respectively. The period T in steady-state is 1172 and 4627 iterations for Model 1 and 4. Since the experimental measurement of frequency is not available, St and T are used for investigating unsteady characteristics of cavitation.

For both cases, the magnitude of V_v from Model 4 is more than twice as big as those from the other models, because vapor is more diffused with a smooth interface, due to low gradients of mixture density. The attempt to sharpen the interface by reducing a_{min} encounters stability problems in the computations.

Pressure coefficient

$-C_p$ from all the models shows a good agreement with that from the experiment for $\alpha = 4^o$ in Figure 3.4 (left). As the constant pressure region is shorter than that in the experiment, the cavity length L_c is shorter. The fact that the values of L_c from all the models are similar, implies that the difference in L_c from the experiment is more likely to be not due to the cavitation model, but due to the fundamental difference in flow characteristics.

The constant pressure at the leading edge and the mid-chord for $\alpha = 4^o$ and 1^o, respectively, corresponds to p_b inside the cavity, which is close to p_v. For Model 2, $-C_p$ in the constant pressure region is a bit smaller than σ, i.e. p_b is a bit larger than p_v, whereas p_b is slightly smaller than p_v for Model 3 and 4. The difference between $-C_p$ and σ is more noticeable for $\alpha = 4^o$ having a stronger sheet cavitation with dense vapors. Since the turbulent pressure fluctuation is added to p_v in Model 2, p_b is larger than p_v. $\dot{m}$ in Model 3 is a sum of two terms of which one is always positive. Hence, $\dot{m}$ becomes negative a bit below p_v as in Figure 2.2 and p_b is smaller than p_v. In Model 4, vapor volume fraction is directly linked to p e.g. $p = p_v - \Delta p \rightarrow \alpha_v = 1$ and $p = p_v \rightarrow \alpha_v = 0.5$ in the barotropic state law, hence α_v in the overall cavity for $\alpha = 4^o$ is converged to $\alpha_v \simeq 0.6$ corresponding to $p_b < p_v$.

It is noted that the peak of $-C_p$ i.e. the pressure lower than p_v still exists at the foremost end of the leading edge for $\alpha = 4^o, \sigma = 0.91$, even though it is weakened, compared to that in a fully wetted flow. It implies that it takes time for cavitation bubbles to grow. As the pressure is gradually decreased for $\alpha = 1^o, \sigma = 0.38$, there is no pressure lower than p_v.

For $\alpha = 1^o$, $-C_p$ from the first three models shows a good agreement with that from the experiment with a difference at the closure, because the cavity closure oscillates and the $-C_p$ distribution in Figure 3.4 (right) is taken at a time point corresponding to the mid-point of the upslope in Figure 3.3 (right). In the closing part of cavity for $\alpha = 1^o, \sigma = 0.38$, $-C_p$ from the computation drops more steeply than in the experiment, because C_p from the experiment is time-averaged.

The constant pressure region for Model 4 is less extended than for the other models, probably because the steady-state computation has a limitation for simulating the unsteady cavitation correctly.

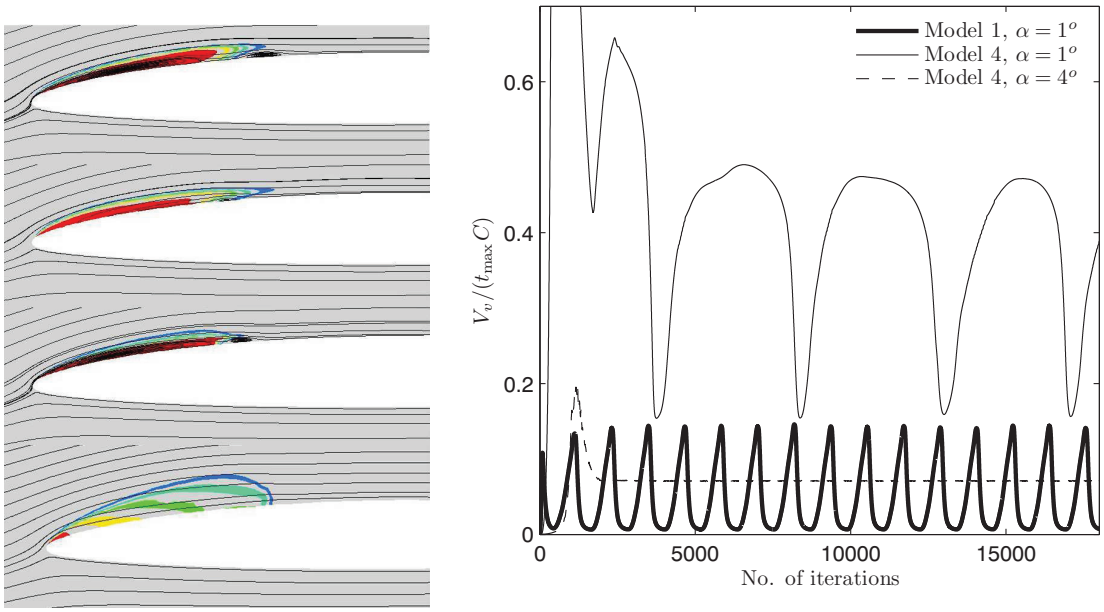

Figure 3.5: α_v and streamlines for $\alpha = 4^o, \sigma = 0.91$ from Model 1 - 4 (from top to bottom on the left column) with the outermost layer i.e. the outer layer of blue filling indicating $\alpha_v = 0.1$, an interval of $\Delta\alpha_v = 0.1$ and the outer layer of red filling indicating $\alpha_v = 0.9$ and total vapor volume as a function of the number of iterations in steady-state computation (right)

Vapor distribution

As shown in Figure 3.5 (left), steady sheet cavitation is on the leading edge for $\alpha = 4^o, \sigma = 0.91$. Since neither snapshots nor measurements of the flow field from the experiment are available, the numerical results for the vapor distribution and the flow field could not be experimentally validated.

For the first three models, the vapor volume fraction is more than 90% in the most part of the cavity and α_v is gradually decreased in the closing part. The upper part of the cavity is more extended at the closure because of the no-slip wall boundary condition. The streamlines of the main flow are affected by the cavity, as the flow in reality goes around a sheet cavity. There are flow separations inside the cavity and at the closure. The flow separation at the closure i.e. re-entrant jet is not strong enough to detach the cavity and is suppressed by the main flow. For Model 4, the cavity is more diffused to the direction perpendicular to the flow and the vapor fraction inside the cavity is gradually decreased. The streamline is not so affected by the vapor contour with no flow separation.

As shown in Figure 3.6 and 3.7, vapor distributions of unsteady cavitation for $\alpha = 1^o, \sigma = 0.38$ are taken at five time-points within a cycle, including the crest and peak of V_v. The distribution of α_v is presented with streamlines at the peak. When each cycle starts from

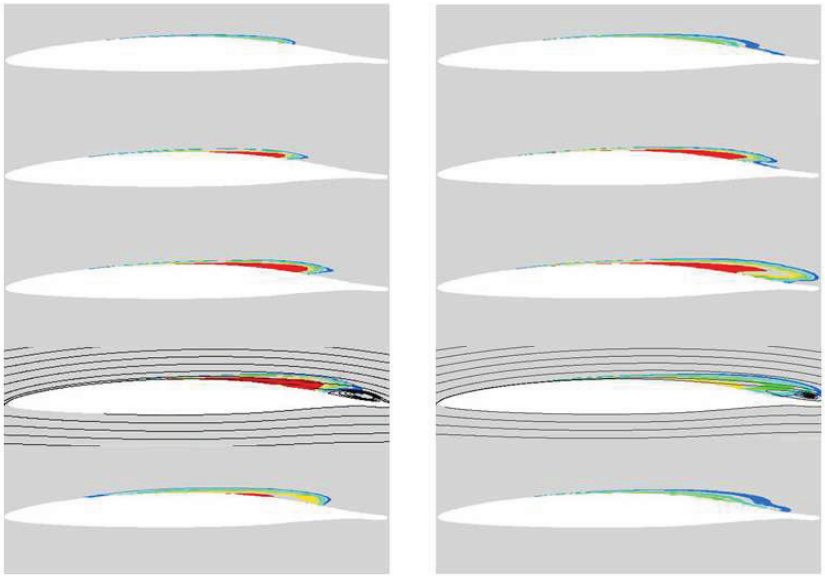

Figure 3.6: α_v for $\alpha = 1^o, \sigma = 0.38$ from Model 1 at $0.00T, 0.20T, 0.40T, 0.58T, 0.78T$ (from top to bottom on the left column) and from Model 2 at $0.00T, 0.25T, 0.43T, 0.63T, 0.80T$ (from top to bottom on the right column)

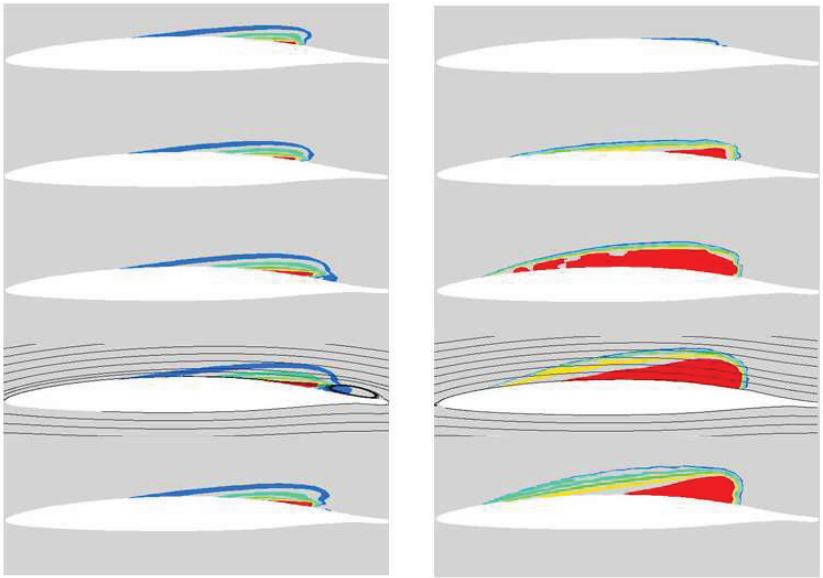

Figure 3.7: α_v for $\alpha = 1^o, \sigma = 0.38$ from Model 3 at $0.00T, 0.21T, 0.42T, 0.58T, 0.79T$ (from top to bottom on the left column) and from Model 4 at $0.00T, 0.09T, 0.30T, 0.56T, 0.86T$ (from top to bottom on the right column)

the crest, the peak is not exactly at half a period $0.5T$. The peak is about at $0.58T$ for Model 1 and 3 and about at $0.43T$ for Model 2. For Model 4, the maximum value of V_v lasts at most of iterations and it drops down momentarily with a regular frequency.

V_v increases more gradually than it decreases, hence the peak is after $0.5T$ for Model 1 and 3. For Model 2, the rate in most of the declining phase is higher than the increase rate, but as it is close to the crest, it decreases slowly and the declining phase becomes longer.

The variation of vapor distribution is explained by a mechanism:

1. A sheet cavity grows up from the mid-chord until the aft part of the cavity becomes unstable.
2. The unstable part is gradually suppressed and the sheet cavity become small.

The experimental observation (de Lange and de Bruin, 1998) of unsteady sheet cavitation at the leading-edge of the NACA16 hydrofoil shows another mechanism that the aft part of the cavity is pinched off by a re-entrant jet and the detached cavity has a form of cloud cavitation. In our computation, a re-entrant jet is formed and becomes stronger as the cavity grows up, but the cavity interface is not impinged by the re-entrant jet and cloud cavitation is not formed. The observation of cloud cavitation is not mentioned in the experiment corresponding to our case. For Model 4, unsteady cavitation has a similar cycle, but the cavity is less extended chordwise and more diffused vertically without a re-entrant jet.

The results of the computations is that the first three models are to some extent equivalently capable of predicting steady and unsteady cavitation. Model 4 seems to require improvements with respect to accuracy and stability. Further numerical analyses are performed with Model 1.

Lift and drag

Variations of C_L and C_D with σ from the computations are compared with those from the experiment in Figure 3.8 and 3.10. For $\alpha = 4^o$, the lift is decreased, as long as the cavity length L_c is smaller than about $0.2C$ corresponding to $\sigma = 1.0$ approximately. L_c in Figure 3.9 (left) is determined by the contour of $\alpha_v = 0.1$ in the computation, whereas it is dependent on a visual check without a numerical measurement in the experiment. As shown in Figure 3.9 (right), the suction pressure peak is reduced and the increased suction pressure in the constant pressure region is rather small and the pressure on the opposite side is kept almost unchanged. Therefore, the lift is decreased in the computation. C_p on the pressure side is not presented, because its change along σ is insignificant. Since the measurement is not conducted for $1.00 < \sigma < 1.76$, the lift decrease is not demonstrated in the experiment.

As the cavity is more extended for a lower value of σ, the total suction pressure is increased due to the extended constant suction pressure inside the cavity and hence the lift is increased.

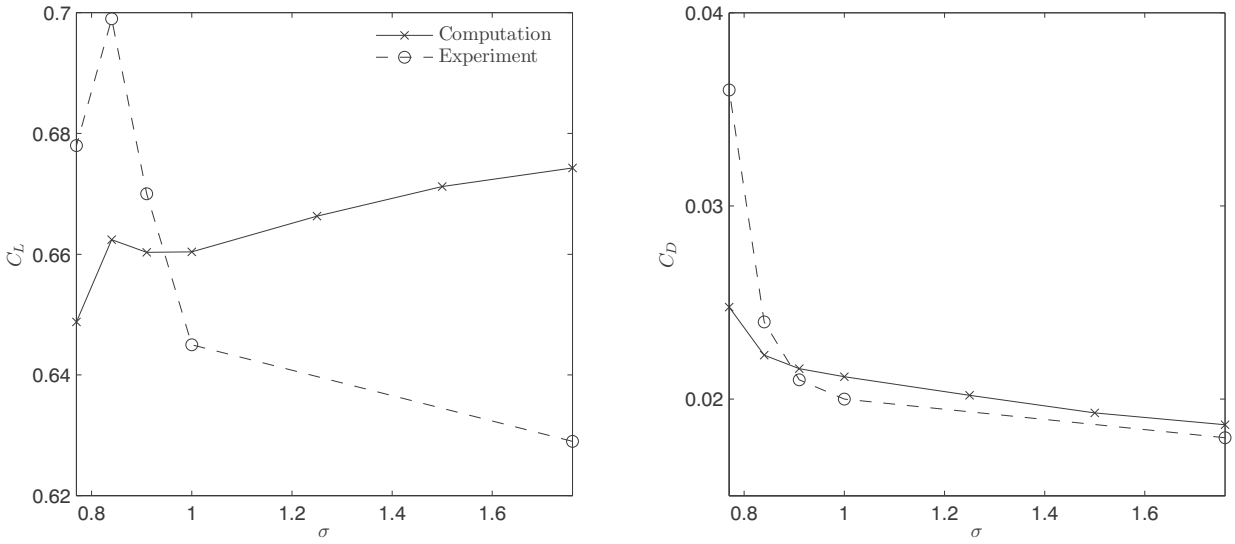

Figure 3.8: C_L (left) and C_D (right) as a function of σ for $\alpha = 4^o$

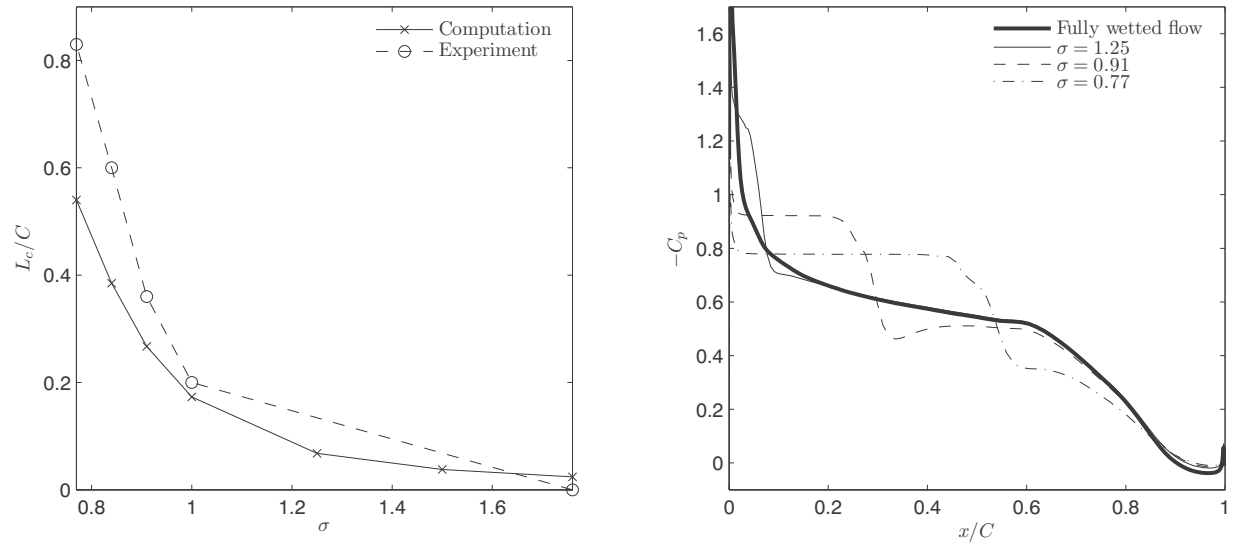

Figure 3.9: Cavity length as a function of σ (left) and pressure coefficient on the suction side (right) for $\alpha = 4^o$

As the cavity in the experiment is more extended than in the computation, the lift increase is also larger.

For $\sigma = 0.77$, L_c fluctuates with an amplitude of $\Delta L_c = 0.022C$ and $St = 0.636$. C_L and C_D are averaged by taking the mean value of the maximum and the minimum in a cycle. As the cavity is extended to more than $0.5C$, the main flow around the cavity results in a significant decrease of the suction loading at $x/C \simeq 0.6 - 0.8$ behind the cavity and the average lift is decreased accordingly. In Figure 3.9(right), $-C_p$ for $\alpha = 4^o, \sigma = 0.77$ is taken at the average L_c.

As the cavity is increased, the drag is also increased. The formation of cavity makes the main flow detour and hence the form drag is increased. The increased turbulence behind the cavity induce an additional drag. In the experiment, the drag at $\sigma = 0.77$ and 0.84 is steeply increased due to the higher turbulent intensity.

Although the values of C_L and C_D in the computation are quantitatively different from those in the experiment due to the 3D effects and turbulent intensity as mentioned before, they show qualitative agreements with similar changing patterns.

For $\alpha = 1^o, \sigma = 0.4$, the total suction pressure is increased and the lift is accordingly increased, as the cavity is extended. As the pressure loading on the pressure side is reduced, C_L in the computation is decreased for $\sigma = 0.38$. In Figure 3.11, the lower curve indicates $-C_p$ on the pressure side. In the experiment, turbulent intensity may not be enough to induce a flow separation and a corresponding alternation of the pressure-side loading for $\sigma = 0.38$, because rough elements are installed only on the leading edge in the experimental model. For $\sigma = 0.347$ and 0.34, the lift in both the experiment and the computation is further decreased by the reduced loading on the pressure side in spite of the suction increase. Since the alternation of the pressure-side loading appears more remarkably at the minimum value of V_v, $-C_p$ for $\alpha = 1^o$ in Figure 3.11 (left) is taken at that moment for unsteady cavitation.

As the cavity is increased, the drag is increased due to increased form drag and higher turbulent intensity. The drag increase in the computation is larger than that in the experiment. This difference is probably due to the turbulent intensity. The drag from the experiment has an irregular decrease for $\sigma = 0.347$.

3.3 Numerical properties

Time-step, under-relaxation factor and iteration number

Computations are made for $\alpha = 1^o, \sigma = 0.38$ with varying the time step Δt and the under-relaxation factor α_{cav} for the vapor transport equation to investigate their effects on cavitation characteristics and the numerical solution. Δt and α_{cav} are less important for the converged solution, hence their effects are analyzed only for unsteady cavitation.

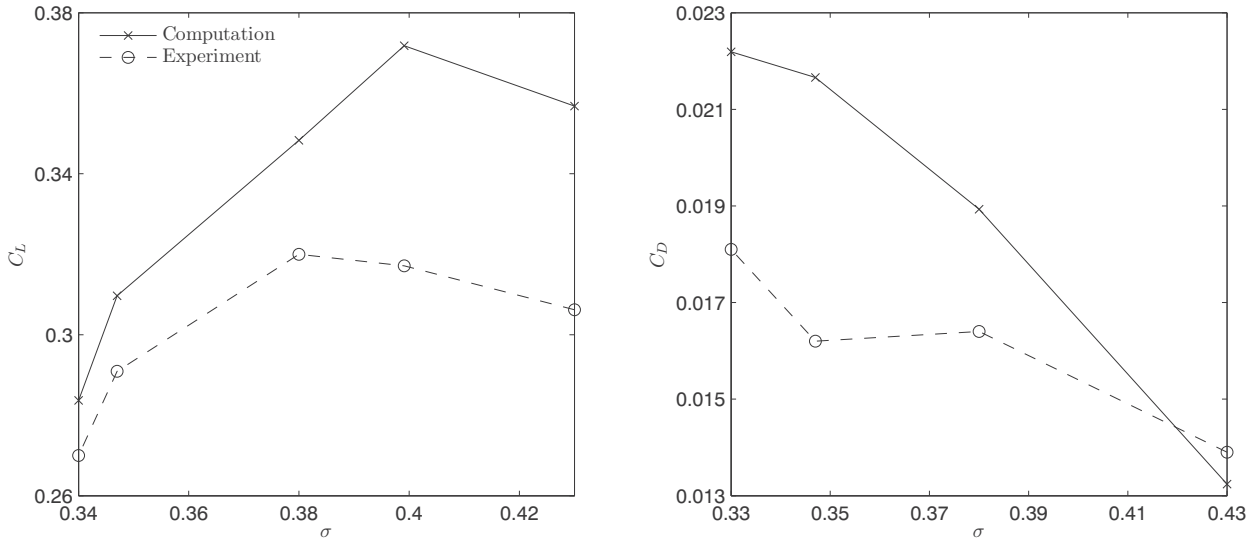

Figure 3.10: C_L (left) and C_D (right) as a function of σ for $\alpha = 1^o$

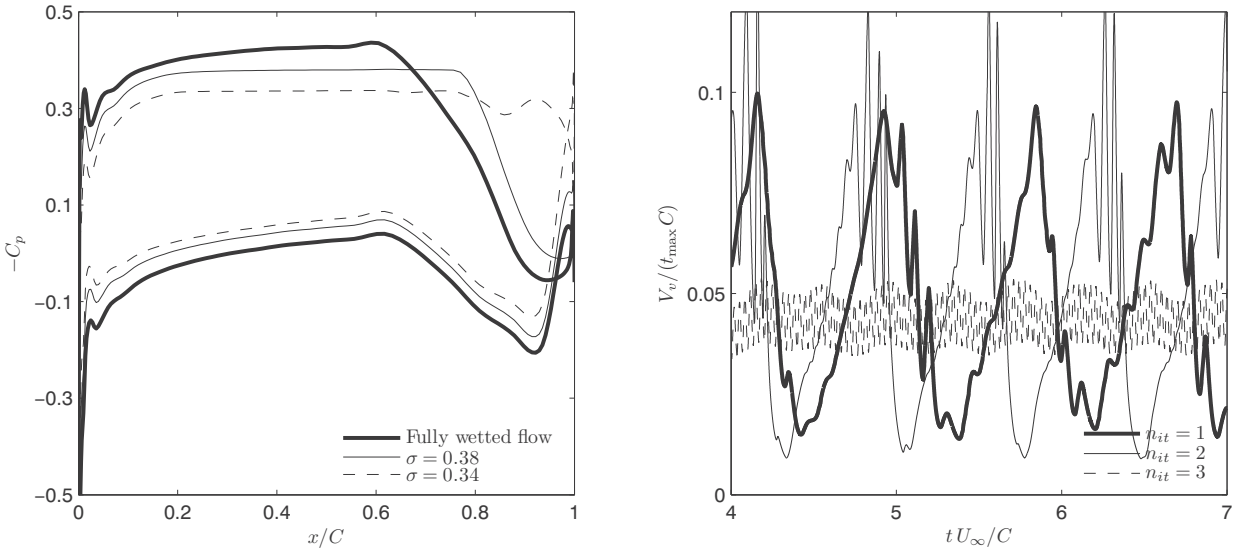

Figure 3.11: Pressure coefficient (left) on both sides for $\alpha = 1^o$ and total vapor volume along time (right) with different number of iterations at each time-step

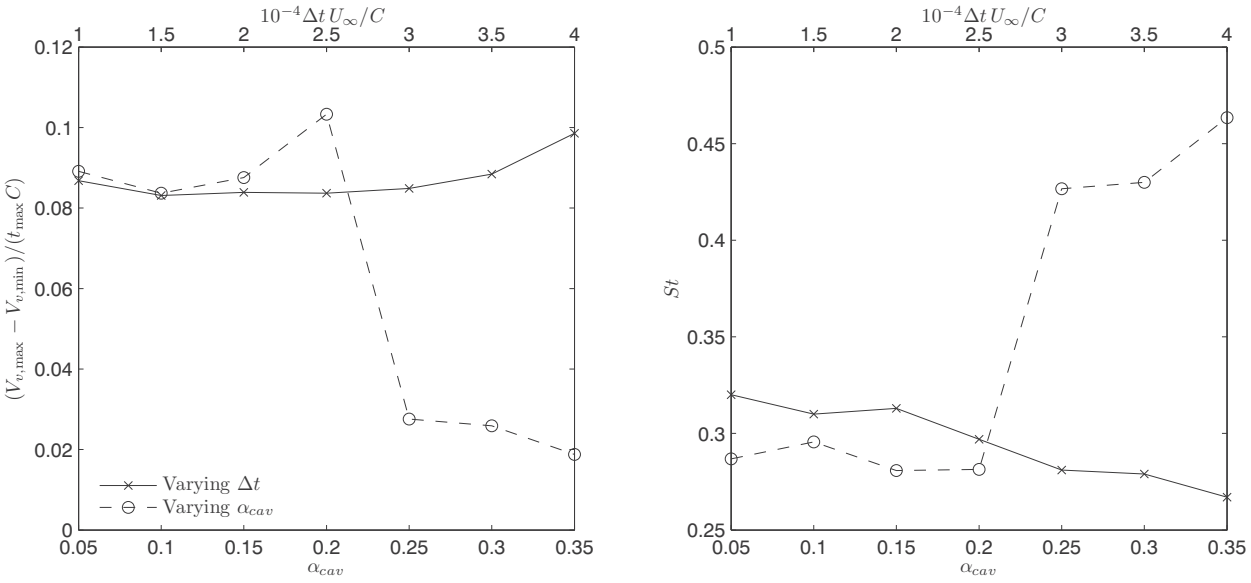

Figure 3.12: Amplitude (left) and St (right) of the vapor volume variation as functions of Δt and α_{cav} for $\alpha = 1^o, \sigma = 0.38$

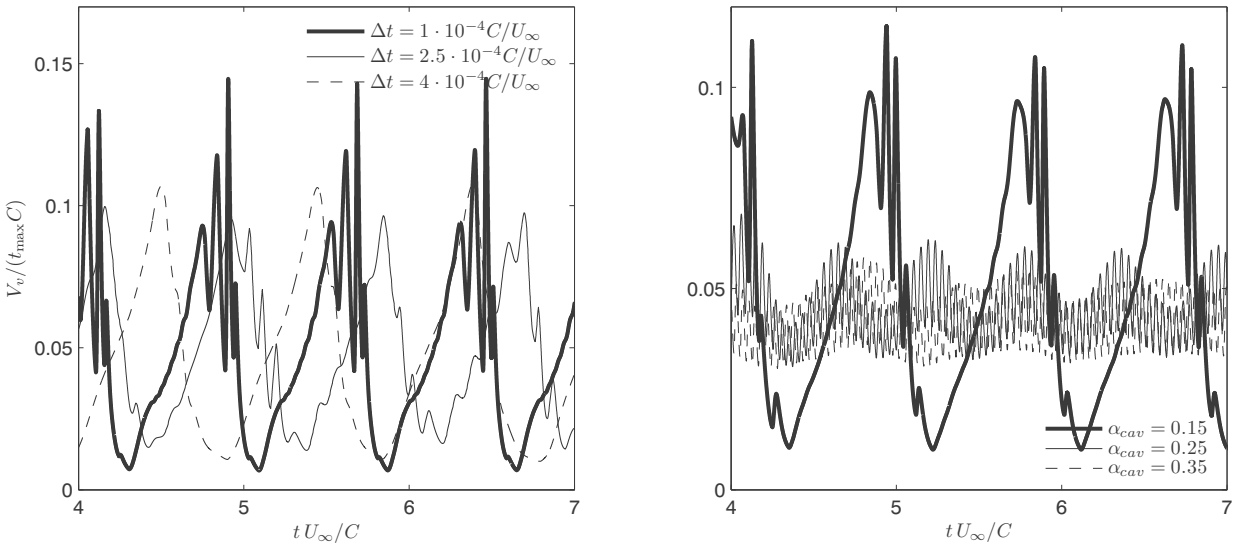

Figure 3.13: Total vapor volume as a function of time for three different values of Δt (left) and for three different values of α_{cav} (right)

The amplitude and Strouhal number of the total vapor volume variation as functions of Δt and α_{cav} are presented in Figure 3.12. It is to be noted that x-axes on the top and bottom indicate Δt and α_{cav}, respectively. $\alpha_{cav} = 0.1$ and $\Delta t = 2.5{\cdot}10^{-4}C/U_\infty$ are fixed with varying Δt and α_{cav}, respectively. The variation of V_v in some cases has high-peak fluctuations on a down-slope, which are regarded as numerical noise and are not considered in calculating the amplitude.

The maximum variation of the amplitude for the five smallest values of Δt is $6.89 \cdot 10^{-3}$. The amplitude for the three smallest values of α_{cav} is also converged with the maximum variation of $3.89{\cdot}10^{-3}$. The converged value with respect to Δt is close to that with respect to α_{cav} with a difference of $7.22 \cdot 10^{-3}$, which corresponds to a cavity-length variation of $0.012C$. Such convergence shows consistency of the numerical solution for unsteady cavitation strength with respect to Δt and α_{cav}.

St for the three smallest values is converged with the maximum variations of 0.010 and 0.015 with respect to Δt and α_{cav}, respectively. However, St still has an increasing tendency, as Δt is decreased. It implies that the frequency is affected by the size of Δt. St with respect to α_{cav} is converged with a maximum difference of 0.032 to a value smaller than that with respect to Δt and it shows no increasing or decreasing tendency. It implies that St is converged with respect to α_{cav} for a specific time-step of $\Delta t = 2.5 \cdot 10^{-4}C/U_\infty$.

In Figure 3.13 (left), the variation of V_v along time is rather smooth for $\Delta t = 4 \cdot 10^{-4}C/U_\infty$. As Δt is decreased, the variation of V_v has small fluctuations for $\Delta t = 2.5 \cdot 10^{-4}C/U_\infty$ and high-peak fluctuations on down-slopes for $\Delta t = 1 \cdot 10^{-4}C/U_\infty$. It implies that the numerical instability can be avoided by increasing Δt. The solution of the Rayleigh-Plesset equation by a numerical integration using a fourth-order Runge-Kutta scheme for a spherical vapor under a sinusoidal pressure variation shows such fluctuations of vapor volume on the vapor collapsing phase (Brandner, 2003). Instability on vapor collapse may be from the nature of the equation governing the cavitation model.

When α_{cav} is increased with a fixed time step of $\Delta t = 2.5{\cdot}10^{-4}C/U_\infty$, V_v in Figure 3.13 (right) has high-peak fluctuations as for $\alpha_{cav} = 0.1$ and $\Delta t = 1 \cdot 10^{-4}C/U_\infty$. With increasing α_{cav} further, an additional small-scale periodicity appears with $St = 5.97$ and 6.53 for $\alpha_{cav} = 0.25$ and 0.35, respectively. The small-scale frequency is increased and the amplitude is reduced, as α_{cav} is increased. With the appearance of small-scale periodicity between $\alpha_{cav} = 0.20$ and 0.25, sudden changes of the amplitude and large-scale frequency appear. Small-scale periodicity seems to be a numerical byproduct, because it is the result for $\alpha_{cav} \geq 0.25$. Since the cavitation model is closely related to the pressure correction equation, α_{cav} is required to have similar magnitude as $\alpha_p = 0.1$.

As shown in Figure 3.11 (right), high peaks are on down-slopes for an increased iteration number of $n_{in} = 2$ and small-scale periodicity appears for $n_{in} = 3$. The large-scale frequency and amplitude are suddenly decreased between $n_{in} = 2$ and 3. For $n_{in} = 4$, the cavitation becomes steady with a converged cavity size of $V_v = 0.036 t_{\max} C$. It implies that additional iterations increase numerical noise by weakening physical time-transient characteristics in a similar way as increasing α_{cav}.

Density ratio

In two-phase flows, the density ratio between liquid and vapor has a crucial importance for numerical stability. The mathematical formulation and implementation, based on the homogeneous equilibrium modeling approach and the pressure correction equation with volume fluxes and a mass transfer rate, are intended to overcome the challenge from high density ratio. The density ratio between water liquid and saturated water vapor is larger than 50000 at room temperature. $\rho_l = 1000$ and $\rho_v = 0.1$ are here applied to the computations, if it is not mentioned explicitly.

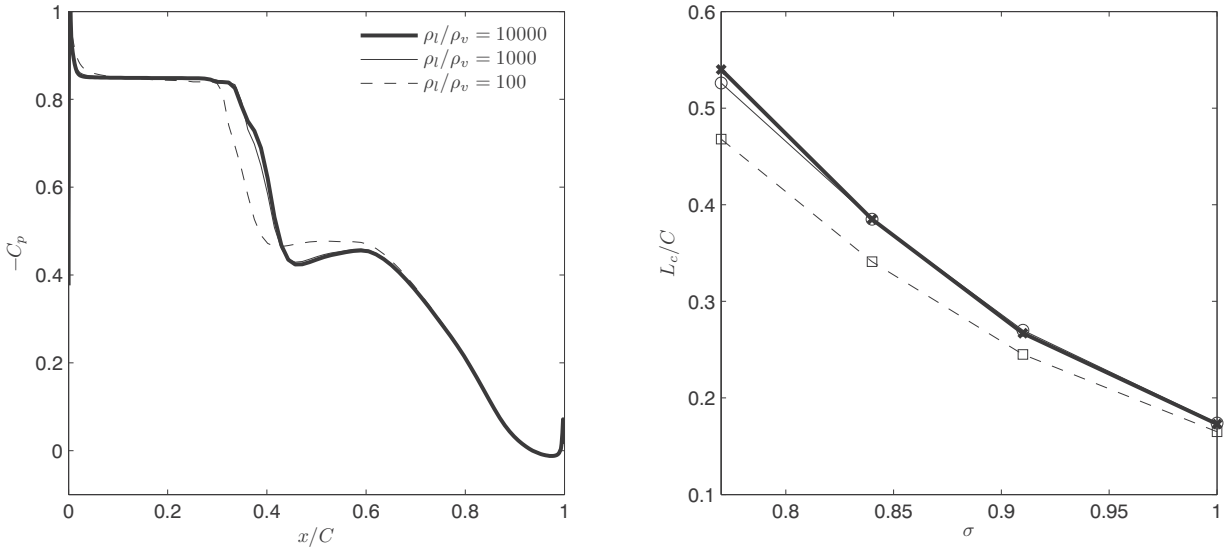

Figure 3.14: Pressure coefficient on the suction side for $\alpha = 4^o, \sigma = 0.84$ (left) and cavity length as a function of σ for $\alpha = 4^o$ (right)

The computation is performed with varying ρ_l/ρ_v. ρ_l is fixed and ρ_v is adjusted to ρ_l/ρ_v. ρ_v in the definition of $\dot{m}$ is kept fixed as $\rho_v = 0.025$ to calibrate the level of $\dot{m}$ only by C_e, C_c.

While $-C_p$ for $\alpha = 4^o, \sigma = 0.84$ is almost identical for $\rho_l/\rho_v = 1000$ and 10000, the cavity is less extended and the drop of $-C_p$ behind the cavity is less for $\rho_l/\rho_v = 100$, as shown in Figure 3.14 (left).

In Figure 3.14 (right) and 3.15, L_c, C_L and C_D as functions of σ have similar distributions for $\rho_l/\rho_v = 1000$ and 10000. For $\rho_l/\rho_v = 100$, L_c is smaller over the whole range of σ and the difference becomes larger, as σ is decreased. An increase in C_L at $\sigma = 0.84$ does not appear and C_L is gradually decreased, as σ is decreased. C_D has a similar increasing pattern, but the increase at $\sigma = 0.77$ is smaller. Such differences are caused by the fact that a cavity with a lower density ratio is not influential enough to divert the main flow from the cavity. The streamlines in Figure 3.16 (left) are not diverted significantly from the cavity and no flow separation occurs inside the cavity and at the closure for $\rho_l/\rho_v = 100$.

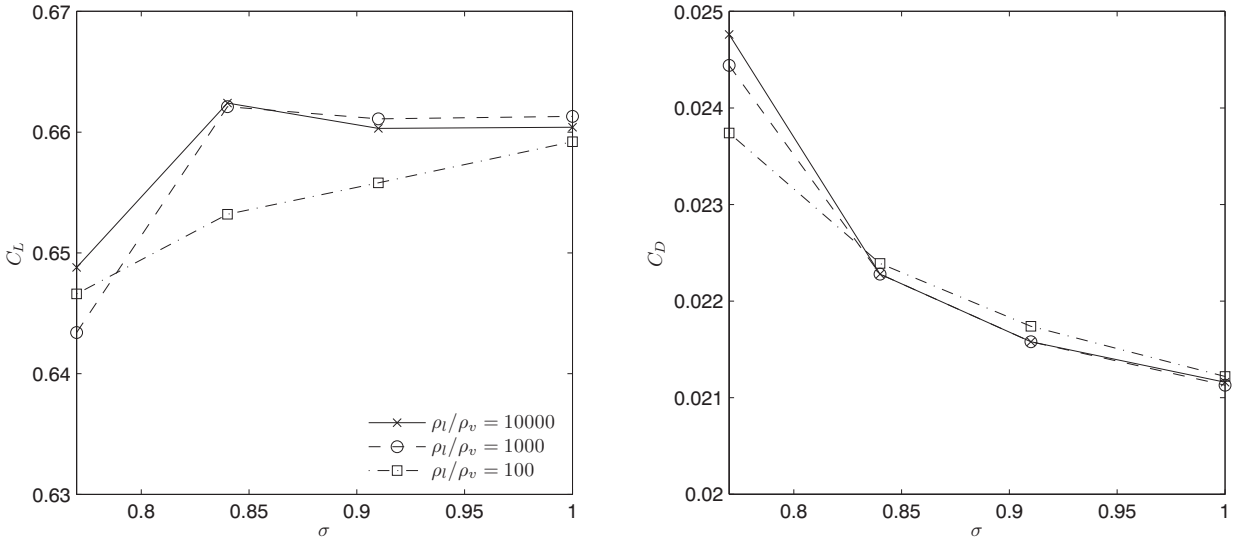

Figure 3.15: C_L (left) and C_D (right) as a function of σ for $\alpha = 4^o$

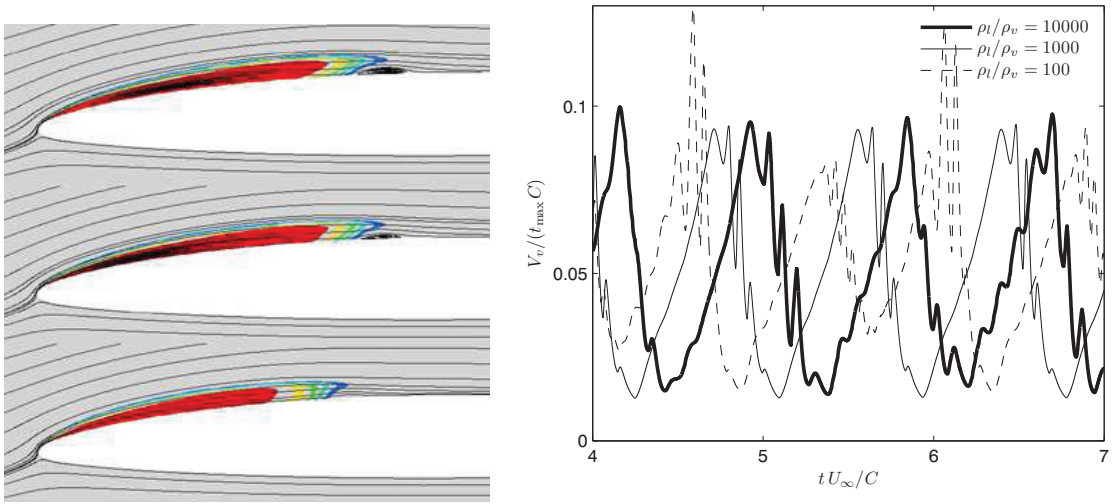

Figure 3.16: α_v with streamlines for $\alpha = 4^o, \sigma = 0.84$ with $\rho_l/\rho_v = 10000, 1000, 100$ (from top to bottom on the left column) and total vapor volume as a function of time (right) with different values of ρ_l/ρ_v

The variation of vapor distribution along time for $\alpha = 1^o, \sigma = 0.38$ does not differ significantly for varied density ratios. As shown in Figure 3.16 (right), the variation frequency is higher with a smaller amplitude for $\rho_l/\rho_v = 100$ than for higher density ratios. As the effects of vapor as a different phase are weakened, the unsteadiness of cavitation is also weakened.

The consistence in the results for $\rho_l/\rho_v = 1000$ and 10000 implies that a density ratio of 1000 is enough for the simulation of cavitating flows with avoiding the risk of numerical instability from higher density ratios.

Coefficients for evaporation and condensation

The definition of mass transfer rate contains constant coefficients C_e and C_c for evaporation and condensation, respectively. C_e and C_c have a certain range for numerical stability, which differs case by case. Their effects are investigated by applying different values of C_e and C_c to the computations. C_e and C_c are fixed as $C_e = 0.5$ and $C_c = 1.0 \cdot 10^{-4}$, respectively, when the other is varied.

Figure 3.17 (left) shows that the constant pressure region in the distribution of $-C_p$ for $\alpha = 4^o, \sigma = 0.84$ is more extended and $-C_p$ behind that region drops more steeply to a lower point, as C_e is increased. For higher value of C_e, the peak at the leading edge is lowered and the constant region starts a bit more at the fore. Since a higher value of C_e leads to stronger evaporation, the cavity is formed faster and extended more. As shown in Figure 3.18 (left), the gradient of vapor fraction at the interface is increased especially along the direction perpendicular to the main flow for a higher value of C_e, because the evaporating rate is increased only on the points with $p < p_v$. As the interface is more sharpened, the main flow around the cavity and the flow separation at the closure are more noticeable, which leads to the sharper decline of the suction pressure at the closure.

Since C_c is related to condensation, its effects appear only at the closure, where vapor is condensed. As C_c is increased, a decrease of α_v starts earlier and the cavity is shortened. The gradient of α_v at the closure is expected to be increased for a higher value of C_c, but it is not increased in our case and is even a bit lower along the flow direction, because the local pressure is not high enough to induce rapid condensation and the donor-phase amount reduced earlier, damps down the condensing rate. The gradient of α_v for $C_c = 0.5 \cdot 10^{-4}$ is higher directly due to the reduced C_c, compared to that for $C_c = 1.0 \cdot 10^{-4}$.

L_c for different values of C_e in Figure 3.19 (left) shows that it is increased with a similar rate, as σ is decreased. For a higher value of C_e, L_c is a bit larger over all applied values of σ except for $\sigma = 0.77$. For $\sigma = 0.77$, cavitation is unsteady and L_c fluctuates. As C_e is increased, the frequency of V_v is decreased with an increased amplitude and the unsteadiness becomes more severe.

L_c for different values of C_c in Figure 3.19 (right) shows a similar changing trend. L_c for a higher value of C_c is smaller. While the difference for $C_c = 1.0 \cdot 10^{-4}$ and $2.0 \cdot 10^{-4}$ becomes

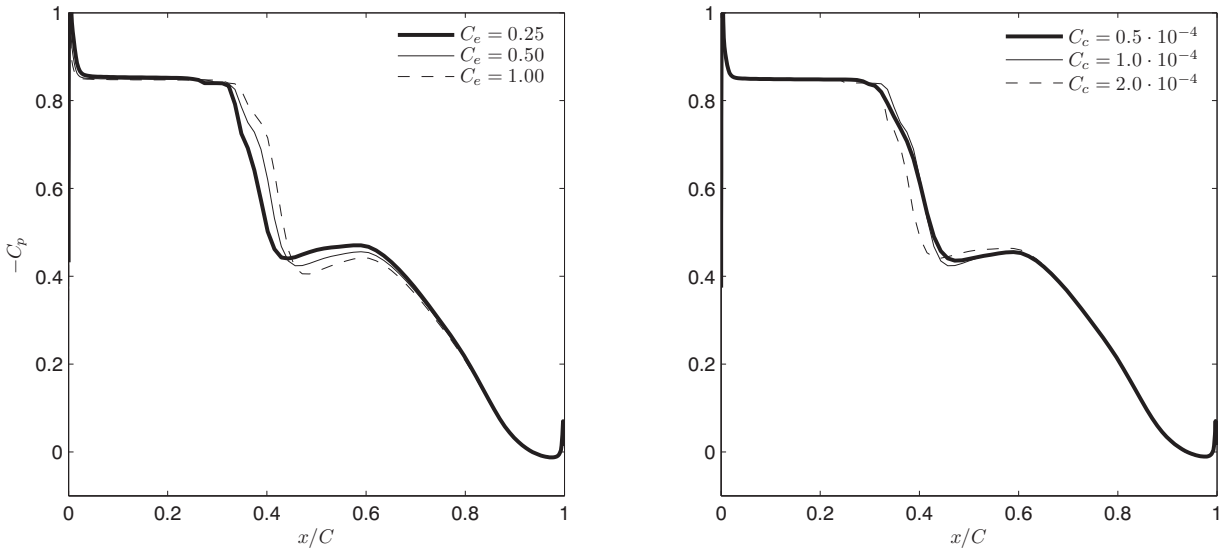

Figure 3.17: Pressure coefficient on the suction side for $\alpha = 4^o, \sigma = 0.84$ with varying C_e (left) and C_c (right)

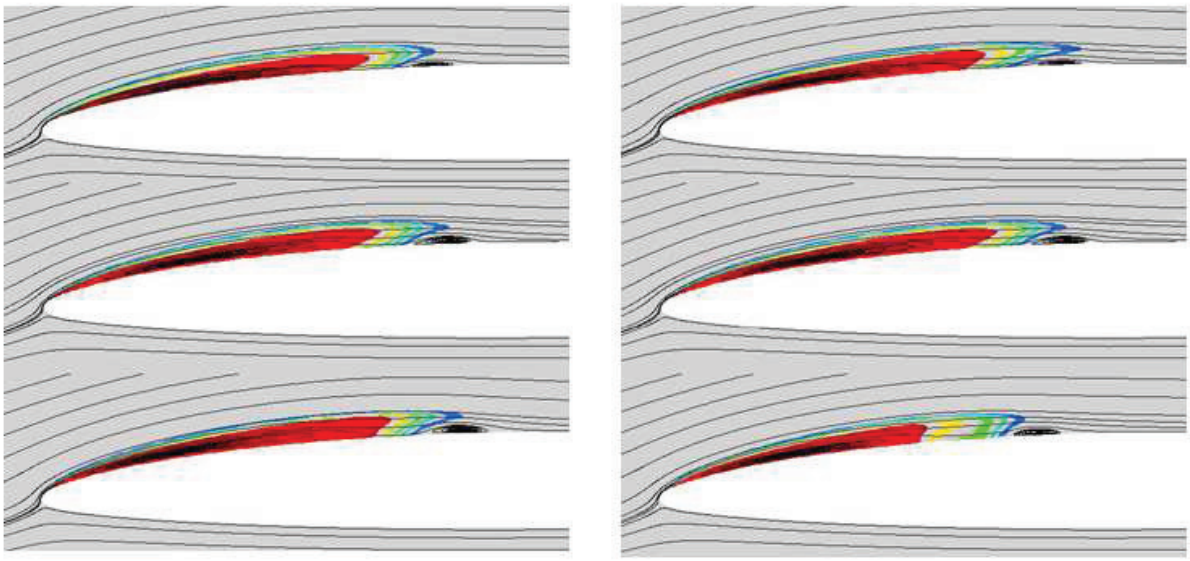

Figure 3.18: α_v with streamlines for $\alpha = 4^o, \sigma = 0.84$ with $C_e = 0.25, 0.50, 1.00$ (from top to bottom on the left column) and $C_c = 0.5 \cdot 10^{-4}, C_c = 1.0 \cdot 10^{-4}, C_c = 2.0 \cdot 10^{-4}$ (from top to bottom on the right column)

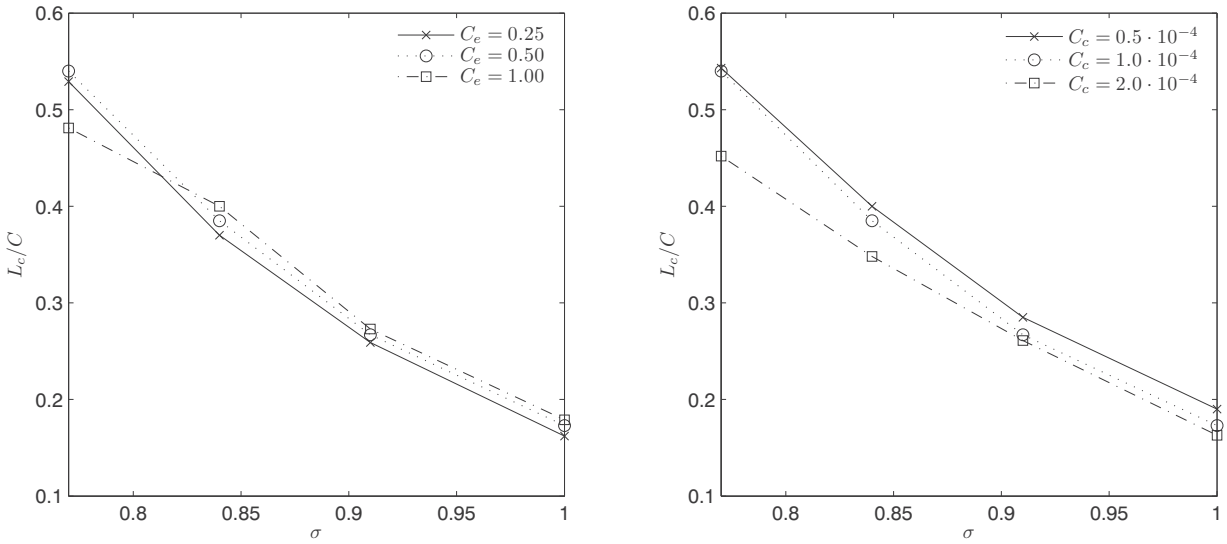

Figure 3.19: Cavity length as a function of σ with varying C_e (left) and C_c (right)for $\alpha = 4^o$

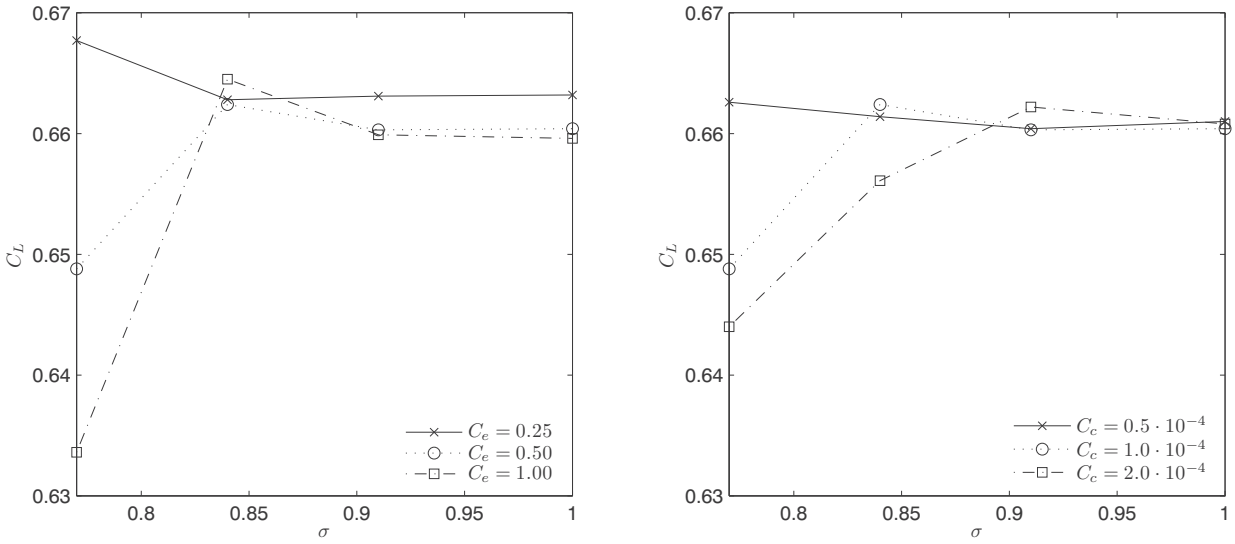

Figure 3.20: C_L as a function of σ with varying C_e (left) and C_c (right) for $\alpha = 4^o$

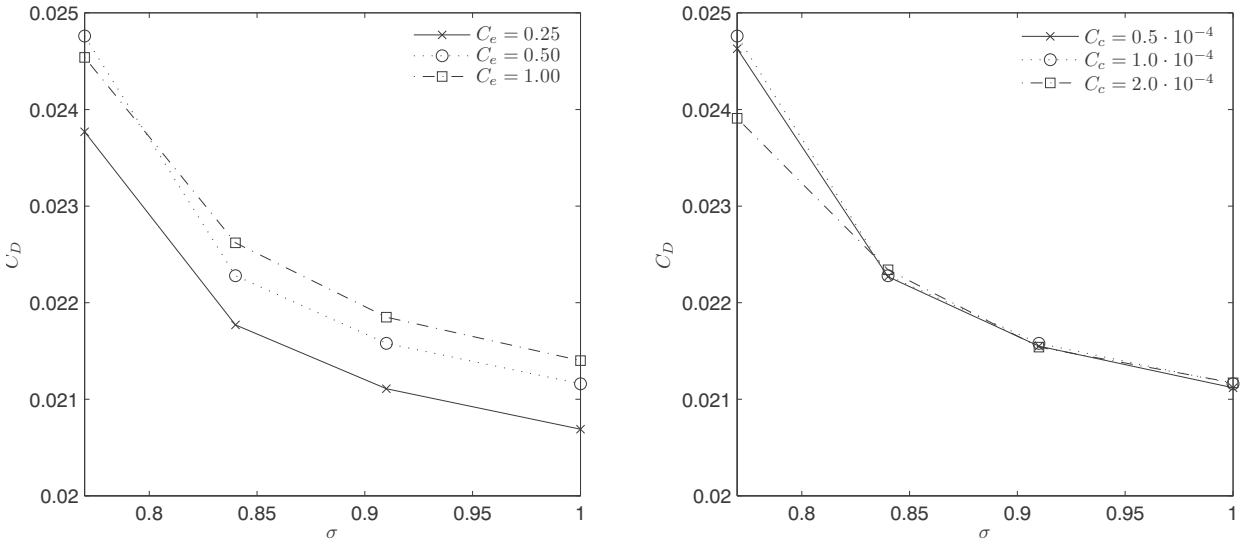

Figure 3.21: C_D as a function of σ with varying C_e (left) and C_c (right) for $\alpha = 4^o$

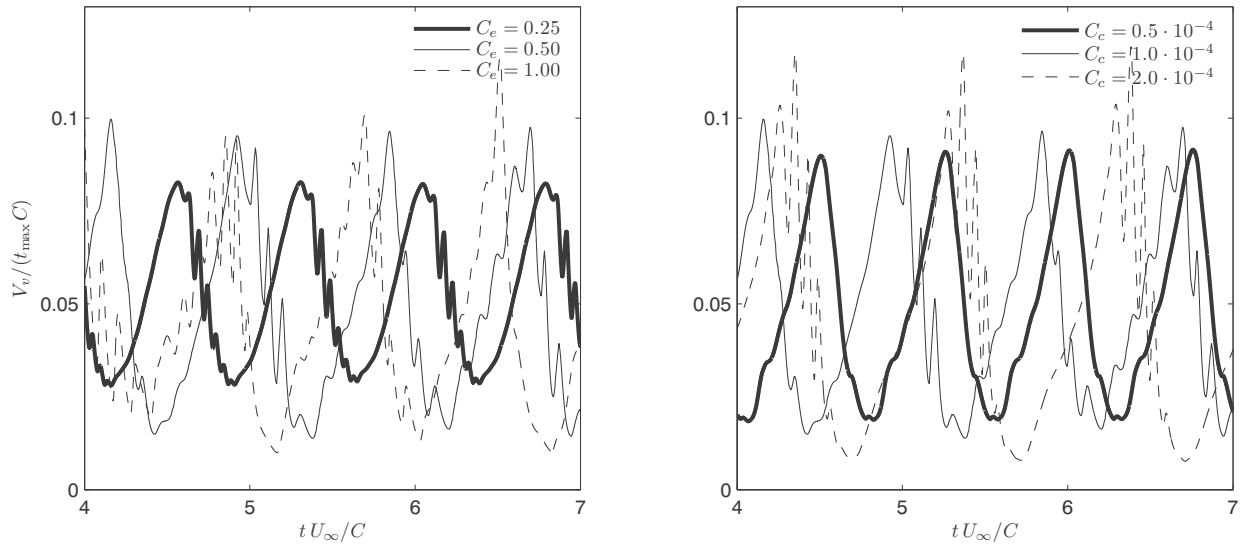

Figure 3.22: Total vapor volume as a function of time with varying C_e (left) and C_c (right) for $\alpha = 1^o$

larger for a smaller value of σ, the values of L_c for $C_c = 0.5 \cdot 10^{-4}$ and $1.0 \cdot 10^{-4}$ become closer to each other. For $\sigma = 0.77$, the frequency and amplitude of V_v are increased for a higher value of C_c, and hence the difference in L_c is also increased.

As shown in Figure 3.20 (left), C_L varies with a similar trend for $C_e = 0.5$ and 1.0. The increase at $\sigma = 0.84$ and the reduction at $\sigma = 0.77$ are larger for $C_e = 1.0$. Such a trend appears at a lower value of σ for $C_e = 0.25$. It is gradually decreased with decreasing σ to 0.84 and it has an increase at $\sigma = 0.77$, because the evaporating strength is relatively small at a certain value of σ for a lower value of C_e.

As shown in Figure 3.20 (right), C_L for $C_c = 2.0 \cdot 10^{-4}$ has an increase at $\sigma = 0.91$, because the drop of $-C_p$ at the cavity closure is less in spite of the shortened cavity length. The cavitation for $C_c = 2.0 \cdot 10^{-4}$ becomes unsteady from $\sigma = 0.84$, hence a decrease of C_L occurs at a higher value of σ, compared to those for lower values of C_c. C_L for $C_c = 0.5 \cdot 10^{-4}$ does not show a decrease at $\sigma = 0.77$, because the cavity does not fluctuate.

The variation of C_D in Figure 3.21 shows a similar trend for different values of C_e and C_c. C_D is larger for a higher value of C_e or C_c over all applied values of σ except for $\sigma = 0.77$. The cavity fluctuation at $\sigma = 0.77$ is stronger for $C_e = 1.0$ and $C_c = 2.0 \cdot 10^{-4}$ than that for lower values of C_e or C_c, hence C_D becomes smaller.

For $\alpha = 1^o, \sigma = 0.38$, the variations of V_v with respect to time for different values of C_e and C_c are compared in Figure 3.22. The frequency is lower with a larger amplitude for a higher value of C_e and C_c. As the evaporating rate is increased, the maximum cavity size is also increased and the variation amplitude is accordingly increased. A higher value of C_c reduces the minimum cavity size further down, which induces a stronger rebound with an increased amplitude. Irregular small fluctuations are increased on up-slopes for a higher value of C_e and on down-slopes for a higher value of C_c, because C_e is related to the increasing phase of a cavity. As C_c is increased, the condensing duration of down-slope becomes a bit shorter than that of up-slope. It implies that C_e and C_c have an influence on the evaporating and condensing durations, respectively, in unsteady cavitation.

Grid size

To investigate the effects of grid size on the cavitation model, we apply grids half and twice the size of the grid used above without changing the domain extent. The number of cells is four times less and more for the coarse and fine grids, respectively, as shown in Figure 3.23. The first-cell height is $\Delta h = 1.5 \cdot 10^{-5}$ and $6 \cdot 10^{-5}$ for the fine and coarse grids, respectively, which result in the location of more cells inside the viscous sublayer for a finer grid.

Figure 3.24 (left) and 3.25 (left) show that the cavity is more extended and thicker with a finer grid for $\alpha = 4^o, \sigma = 0.84$. The re-entrant jet is stronger and the suction pressure drop at the cavity closure is larger, as the grid size is smaller. It seems that the difference in the cavity size is not from the overall grid size but from the grid size at the leading edge, where

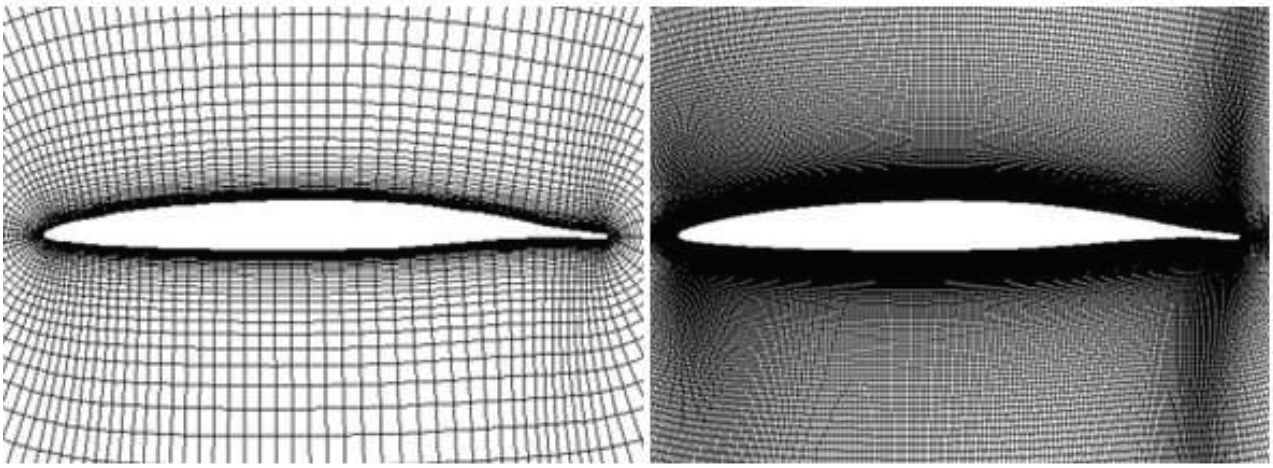

Figure 3.23: The coarse (left) and fine (right) grids around the hydrofoil section

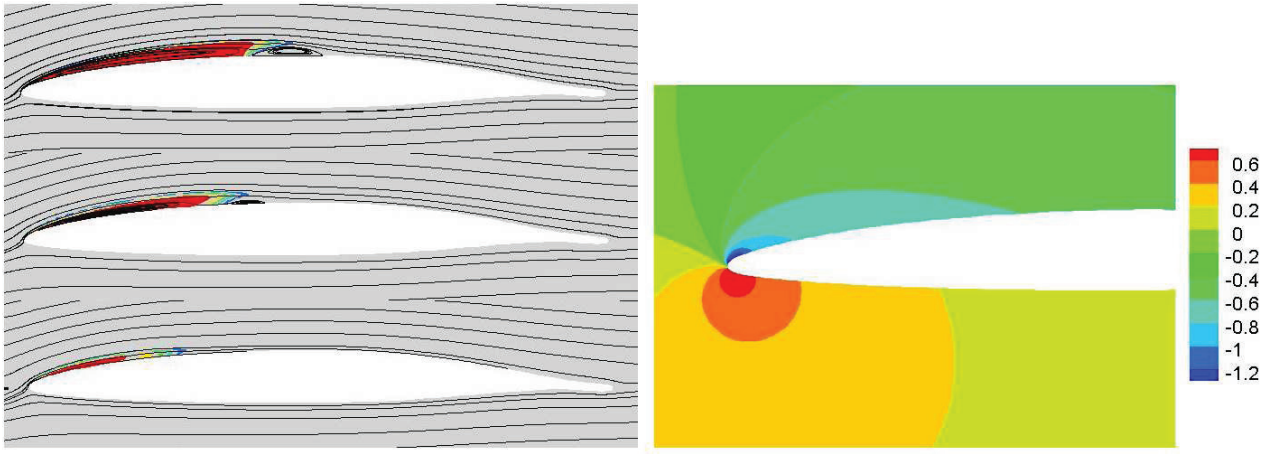

Figure 3.24: α_v with streamlines for the fine, medium, coarse grids (from top to bottom on the left column) for $\alpha = 4^o, \sigma = 0.84$ and C_P (right) in a fully wetted flow for $\alpha = 4^o$

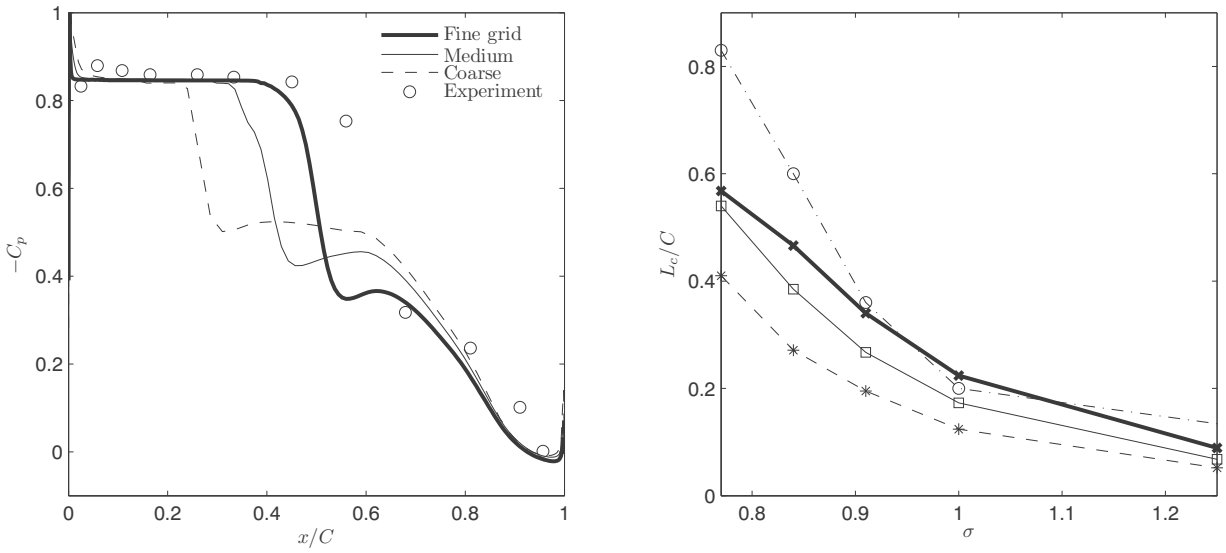

Figure 3.25: Pressure coefficient on the suction side for $\alpha = 4^o, \sigma = 0.84$ (left) and cavity length as a function of σ (right) with varying grid size

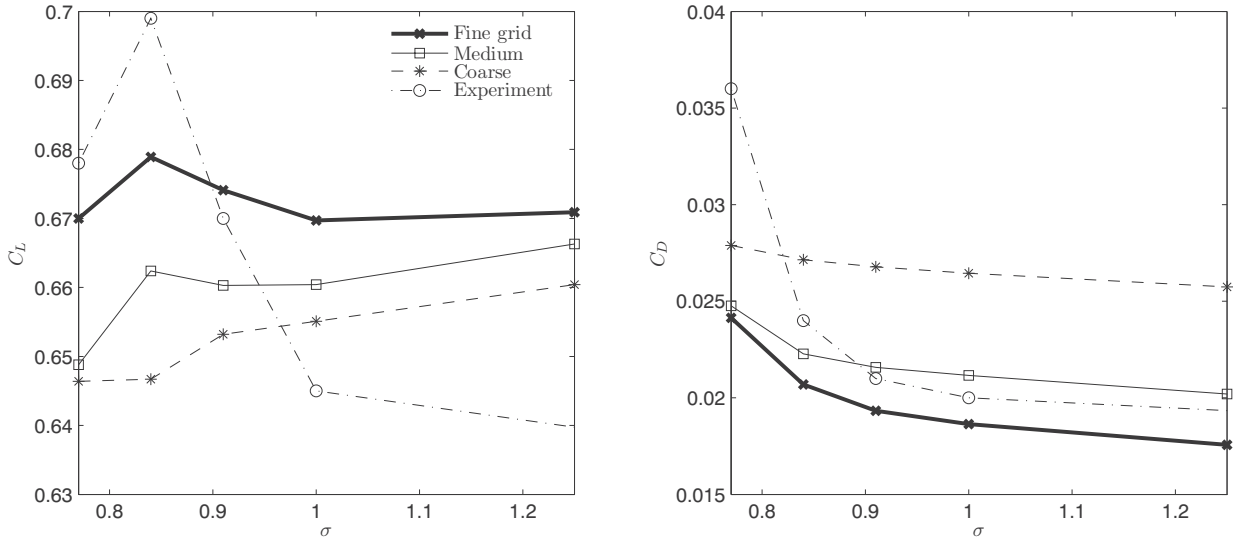

Figure 3.26: C_L (left) and C_D (right) as a function of σ for $\alpha = 4^o$ with varying grid size

the suction peak appears. More cells at the region of the suction peak can result in the development of a thicker cavity, because the cavity formed at the suction peak is convected downstream. The number density of the cells at the suction-peak region can be crucial for the overall development of a cavity in the leading-edge cavitation, because the suction peak in high Reynolds number flows for relatively high incident angles appears in a small area and the cavity formed at the suction peak is convected downstream. The pressure distribution around the fore half of the hydrofoil in Figure 3.24 (right) shows how small the area of $C_P \leq -1$ is in the fully wetted flow.

Since the fine grid has numerical instability in unsteady cavitation, C_e and C_c are reduced by half for $\alpha = 4^o, \sigma = 0.77$. Therefore, the slope of L_c between $\sigma = 0.77$ to 0.84 is smaller for the fine grid, compared to those at the higher values of σ, as shown in Figure 3.25 (right). As the grid is finer, L_c is closer to that from the experiment over all applied values of σ. The numerical instability for unsteady cavitation may be related to the grid size at the cavity closure.

As shown in Figure 3.26 (left), C_L from the computation is quantitatively different from the experimental result for the weak cavitation at $\sigma = 1.25$ due to the effects of three dimensionality in the experiment and the difference is even larger for a finer grid. However, the varying trend for a finer grid is more similar to that in the experiment. C_L for the fine grid shows an increase between $\sigma = 1.00$ and 0.91 like the experimental result, whereas it is almost constant for the medium grid and it is even decreased for the coarse grid. At $\sigma = 0.84$, the increase in C_L is steeper for the fine grid. The decreasing rate for the fine grid is less than for the medium grid due to the reduction of C_e and C_c. C_L for the coarse grid does not show any increase, as σ is decreased.

In Figure 3.26 (right), C_D from the computation shows a similar increasing trend to that from the experiment. C_D for the medium grid is quantitatively closer to that from the experiment at $\sigma \geq 0.91$, but the quantitative comparison is questionable for the estimation of accuracy due to the limitation of the 2D computations as mentioned above. As σ is decreased, the growth rate of C_D is more steeply increased in the experiment than that in the computation. C_D is more steeply increased for a finer grid, although the increasing rate is still smaller than that in the experiment.

3.4 Conclusion for 2D cavitating flows

Numerical solutions are made for cavitating flows on a 2D hydrofoil section. The cases for two angles of attack and several different cavitation numbers are considered. The pressure on the suction side, cavity length, lift and drag from the computation are compared to those from the experiment. The distribution of vapor fraction and the variation of vapor volume along time are analyzed. The results from different models are compared. The effects of numerical properties are investigated with applying several different values to them. The conclusion is summarized by

1. The cavitation models (Model 1-3) based on a vapor transport equation has good quantitative and qualitative accuracy for steady and unsteady cavitations.

2. The numerical result demonstrates physical characteristics of steady and unsteady sheet cavitation, but cloud cavitation is not realized.

3. The three different models (Model 1-3) based on a vapor transport equation have equivalent performances, but the model (Model 4) based on a barotropic state law has lower accuracy, and stability problems occur in the present implementation.

4. The numerical solution has consistency in respect to time-step, under-relaxation factor and density ratio.

5. Additional iterations at each time-step increase numerical fluctuations for unsteady cavitation.

6. Evaporating and condensing rates can to some extent be controlled by the constant coefficients in the definition of the mass transfer rate.

7. More computational cells within the suction-peak region can help the overall development of the cavity in the leading-edge cavitation, but an excessively fine grid at the cavity closure can have a stability problem for unsteady cavitation.

Chapter 4

Cavitating flows on a 3D hydrofoil

The cavitation model is validated for cavitating flows on 3D hydrofoils prior to the cavitation simulation on a ship propeller. We consider non-swept and swept hydrofoils, which resemble conventional and highly-skewed propellers, respectively, in hydrodynamic characteristics.

4.1 Hydrofoil model and flow condition

We consider the hydrofoil models and flow conditions used in the experiment of Ukon (1986). The same section of NACA 16-206 with a meanline of $a = 0.8$ is applied to non-swept and 30^o swept-back hydrofoils. The same scale of the chord length $C = 0.18m$ and the span $s_0 = 0.25m$ as in the experiment is used for the computation. The hydrofoils are mounted in the cavitation tunnel of a $0.75m$-diameter circular section, as shown in Figure 4.1. The hemispherical computational domain in Figure 4.2 is based on an O-O topology consisting of about $1.4 \cdot 10^6$ cells with an extent of about $5C$. The first-cell height is $\Delta h = 5.5 \cdot 10^{-6}C$ leading to $y^+ \leq 1$ and the grid size is increased from near-field to far-field by the tanh function. The symmetric boundary condition is applied to the side wall.

Unsteady-state computations are made for $\alpha = 4^o, U_\infty = 6m/s$ with the non-swept hydrofoil and for $\alpha = 4.4^o, U_\infty = 6m/s$ with the swept one, both in the fully-wetted flow. The time step is set to $\Delta t = 10^{-4}s$. The under-relaxation factor is 0.1 for the vapor transport equation and pressure correction equation and 0.7 for the momentum conservation equation and turbulence model equations. A single iteration is conducted at each time-step. The solutions are converged with the maximum normalized residual of less than 10^{-3}.

In Figure 4.4, the pressure distributions on the surface at three spanwise positions are compared to those from the experiment. In 40% and 70% span from the root i.e. $y/s_0 = 0.4$ and 0.7, C_p from the computation has a good agreement with that from the experiment all over both surfaces except for the region near the leading and trailing edges. Deviations of

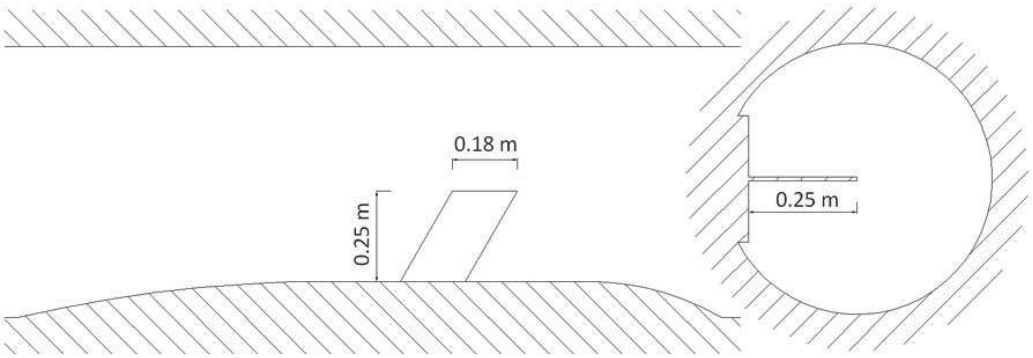

Figure 4.1: Arrangement of the hydrofoil in the cavitation tunnel (Ukon, 1986): horizontal section (left) and vertical section (right)

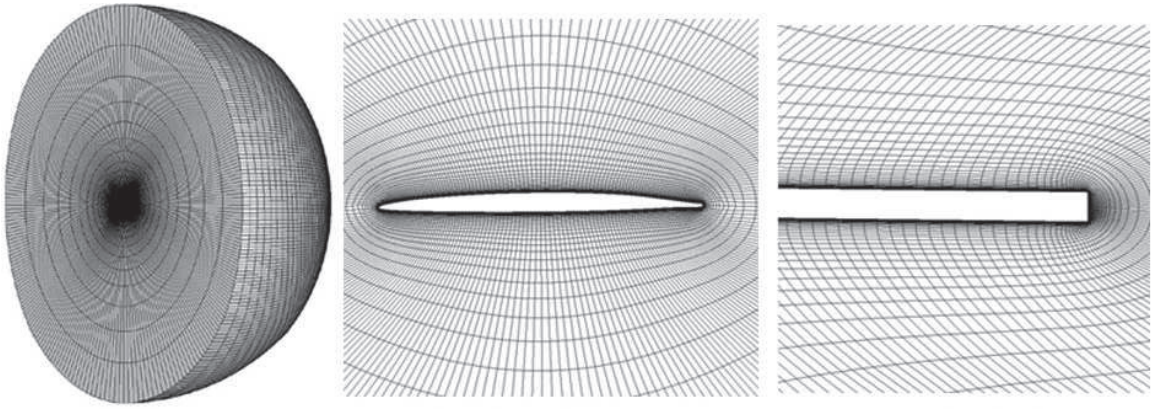

Figure 4.2: Computational grid (left) and close-up views of the side wall (centre) and vertical section (right)

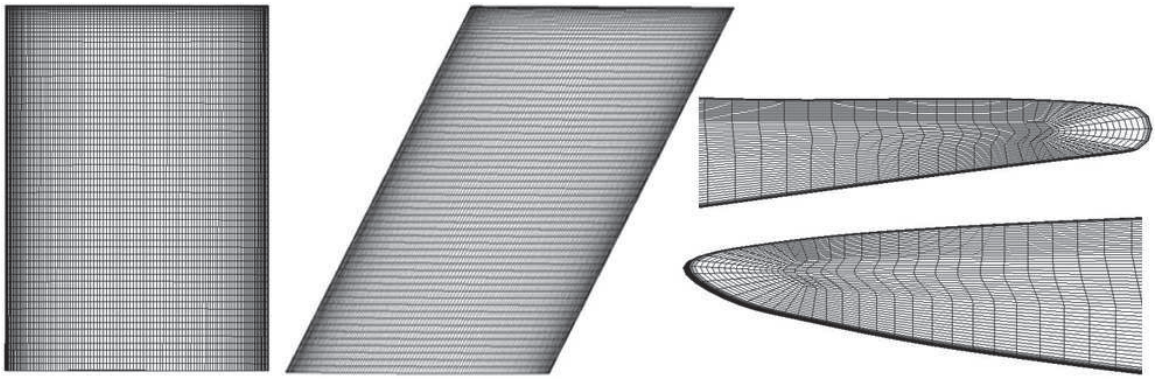

Figure 4.3: Surface mesh of non-swept (left) and 30^o-swept hydrofoils (centre) and tip-side mesh at leading and trailing edges (right)

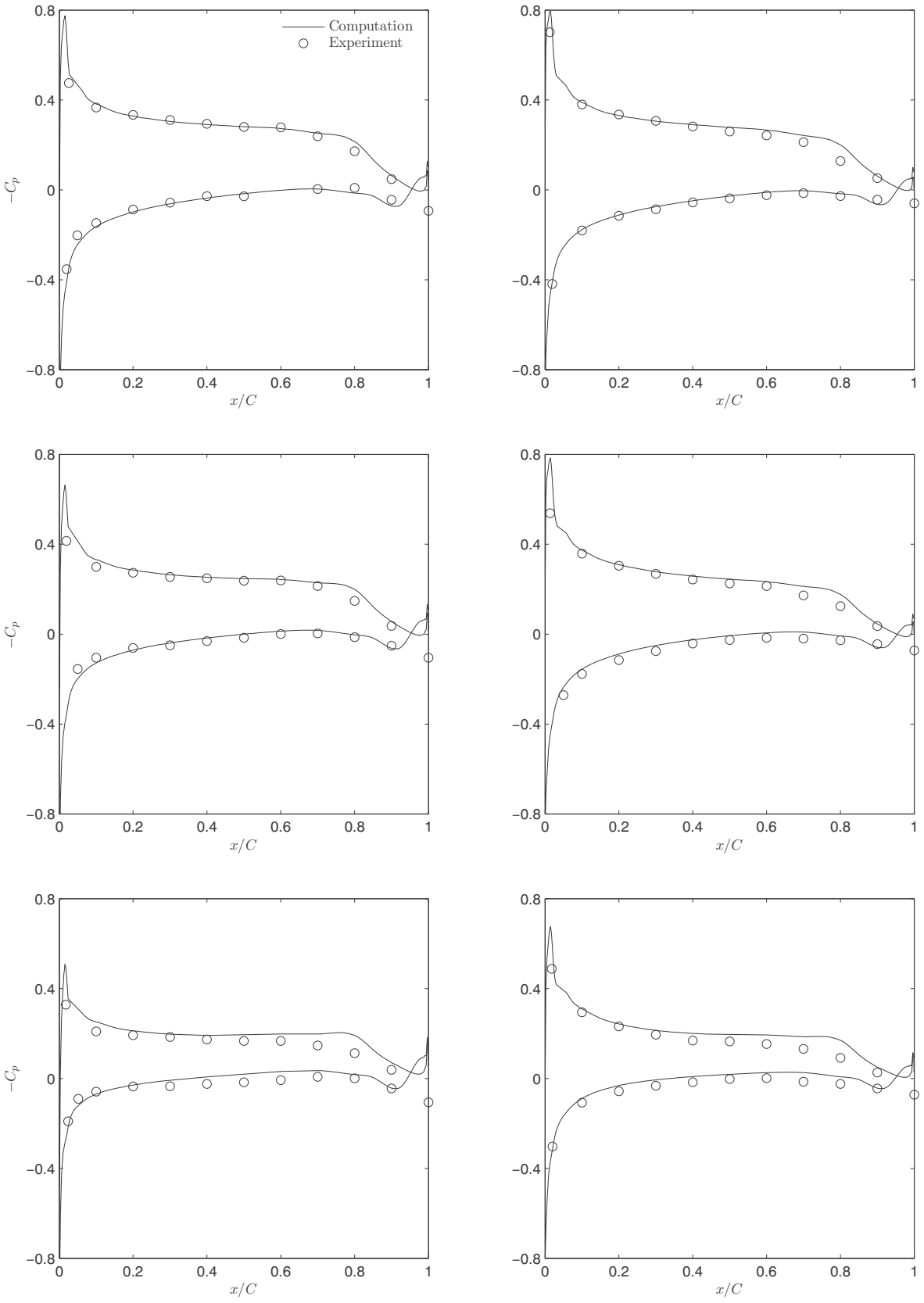

Figure 4.4: Pressure coefficient on the hydrofoil surface of the non-swept (left column) and swept (right column) hydrofoils for $y/s_0 = 0.4, 0.7, 0.9$ (from top to bottom) in the fully-wetted flow

the computational model from the experimental one in geometry and turbulent characteristics may lead to such a disagreement. As the spanwise position gets closer to the tip, the overall suction pressure is decreased. In a position of $y/s_0 = 0.9$ near the tip, noticeable disagreements appear in a more extended region from the trailing edge. It is supposed to be due to the difference in roundness of the tip finishing. While the tip detail is not described in the experiment, a small roundness is applied to the tip edge in the computational model, as shown in Figure 4.3.

4.2 Numerical results

Case 1

Unsteady-state computations are made for cavitating flows. The first case is for a moderate angle of incidence $\alpha = 6^o, U_\infty = 8m/s, \sigma = 0.628$ with the non-swept hydrofoil and $\alpha = 6^o, U_\infty = 8m/s, \sigma = 0.585$ with the swept one. When $C_e = 0.5$ and $C_c = 1.0 \cdot 10^{-4}$ are applied, the total vapor volume fluctuates periodically with time for both hydrofoils. The variation of the dimensionless vapor volume V_v^* with time is shown in Figure 4.5, where $V_v^* = \frac{V_v}{C\, s_0\, t_{\max}}$ and $t_{\max}$ is the maximum thickness of the hydrofoil. The fluctuation on the non-swept hydrofoil has a frequency of $St = 0.448$ with an amplitude of $\Delta V_v^* = 0.008$. The frequency for the swept one is lowered to $St = 0.359$ with a larger amplitude of $\Delta V_v^* = 0.012$.

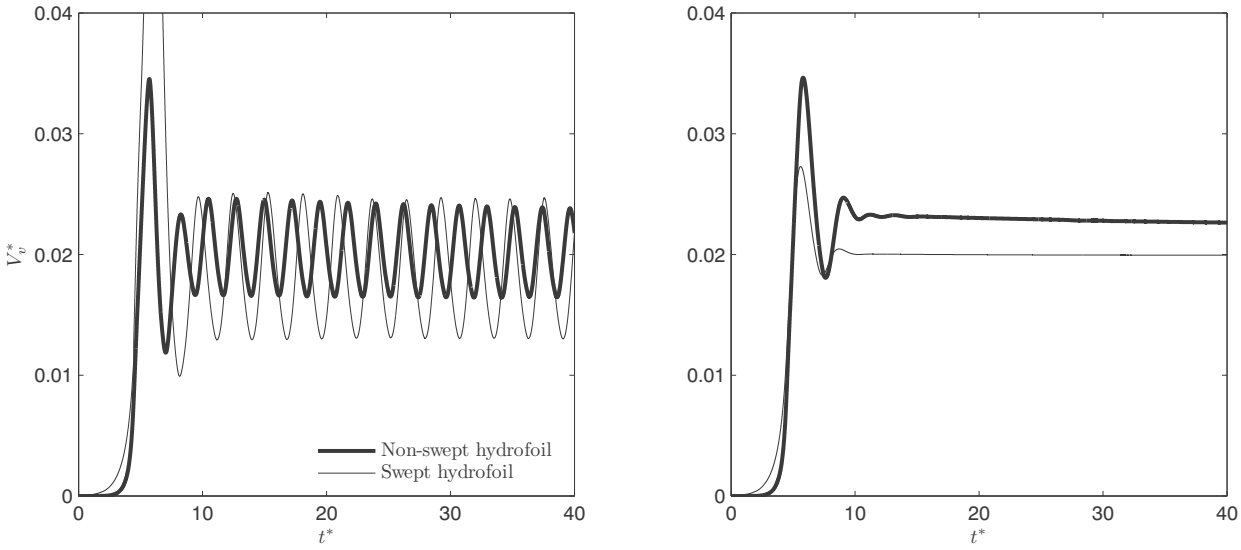

Figure 4.5: V_v^* as a function of t^* for $\alpha = 6^o$ with $C_e = 0.5, C_c = 1 \cdot 10^{-4}$ (left) and with $C_e = 0.5, C_c = 0.5 \cdot 10^{-4}$ (right)

Since the computed maximum chordwise extent of the cavity was shorter than that from the experiment, computations were done with a reduced coefficient of $C_c = 0.5 \cdot 10^{-4}$ for the

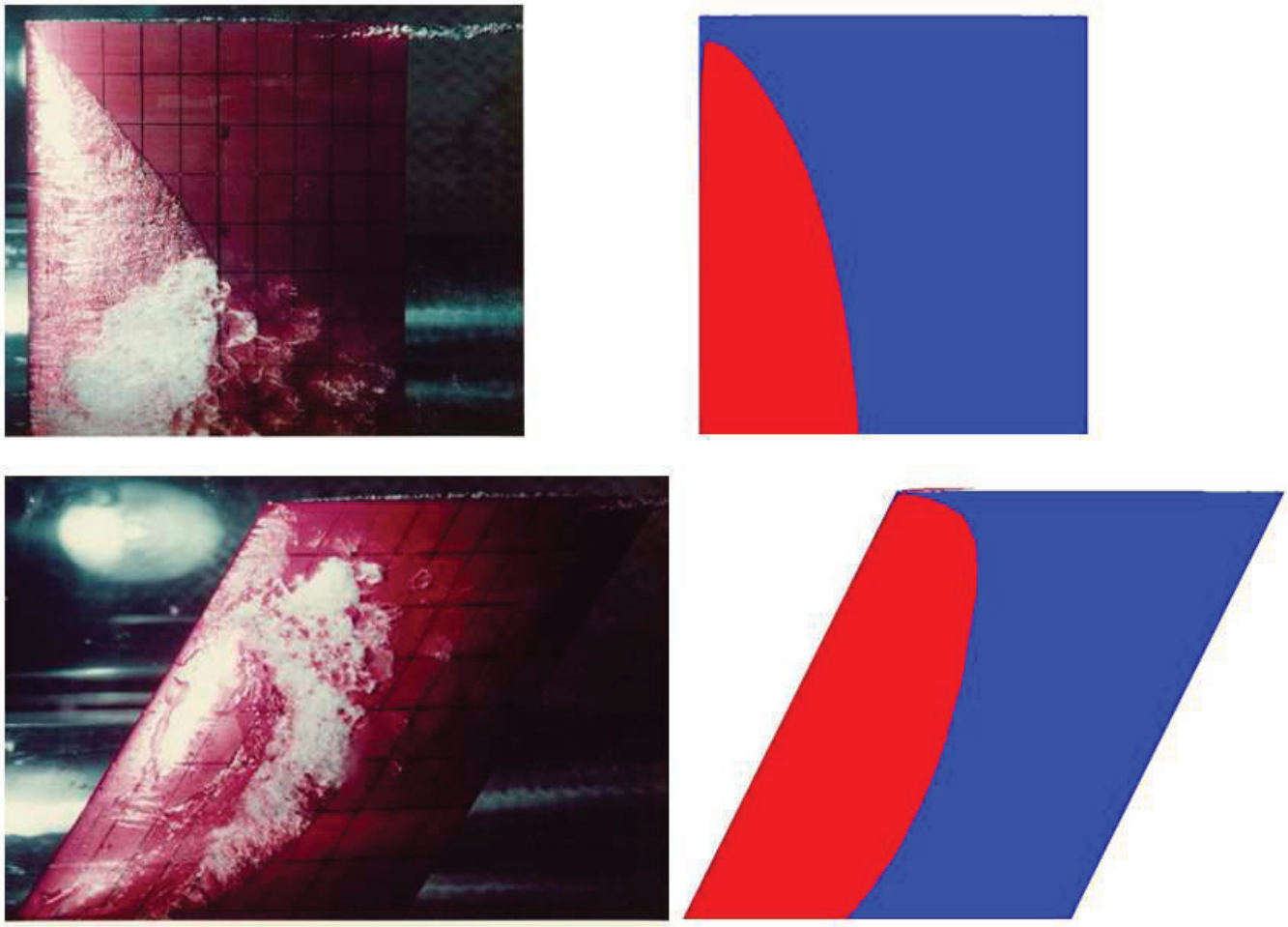

Figure 4.6: Snapshot from the experiment (Ukon, 1986) (left column) and iso-contour of $\alpha_v = 0.1$ from the computation (right column) for $\alpha = 6^o, \sigma = 0.628$ on the non-swept hydrofoil (top) and for $\alpha = 6^o, \sigma = 0.585$ on the swept hydrofoil (bottom)

condensing rate. With a reduced value of C_c, the solution is converged for both hydrofoils with $r_{\max} < 10^{-3}$ and the cavity is more extended. The converged values are $V_v^* = 0.0226$ and 0.0199 for the non-swept and swept hydrofoils, respectively. Although a lower value of σ is applied for the swept hydrofoil with the same values of α and U_∞, the cavity volume is smaller. It is because the effective flow speed for dynamic pressure is determined by the flow component normal to the leading edge and it is decreased according to the sweep angle.

In Figure 4.6, the snapshot from the experiment is compared to the iso-contour of $\alpha_v = 0.1$. The iso-contour in Figure 4.6 and the C_p distributions in Figure 4.7 and 4.8 are taken at the minimum vapor volume $V_{v,\min}$ from the computation with $C_e = 0.5, C_c = 10^{-4}$, because the cavity extent is maximum at $V_{v,\min}$. It is to be noted that only the outer 85% and 80% of the span are taken in the snapshots for the non-swept and swept hydrofoils, respectively, and the iso-contours are made accordingly. The vapor distribution over the entire span is shown in Figure 4.9.

The leading-edge sheet cavitation appears on both hydrofoils. On the non-swept hydrofoil, the chordwise extent of the cavity is increased from the tip to the root. As it gets closer to the root, the increasing rate becomes lower. On the swept hydrofoil, the cavity extent is increased from the tip to the midspan and it is decreased from the midspan to the root. It is not exactly symmetric along the midspan and the cavity at the root is more extended than at the tip. The maximum extent appears between 50% and 60% of the span from the tip.

The cavity at the root is less on the swept hydrofoil, compared to that on the non-swept one, because of the effective flow speed reduced by the sweep angle. Since the boundary layer builds up from the root to the tip on the swept hydrofoil, the cavity at the tip is more extended.

The sheet cavity interface is glass or transparent near the tip and foamy near the root according to the experiment report. When the cavity extent is less than about $0.5C$, the cavity interface looks smooth on the non-swept hydrofoil in the snapshot. When the cavity extent is further extended, cavitation starts with a smooth interface and it becomes rough and the cavity is detached in a form of weak cloud cavitation at the closure. The cavity interface from the computation is a smoothly curved surface without a noticeable microscopic characteristic.

On the swept hydrofoil, the cavity interface in about 40% of span from the root is smooth along the chordwise direction. As it goes to the tip, the rough cavity interface appears from the closure and it spreads. The scattering of cloud cavitation occurs, but it is too weak to recognize in the snapshot. As the boundary layer builds up from the root to the tip, the flow becomes more turbulent and the cavity interface becomes also rougher. Since the suction pressure at the tip is reduced by the tip flow, the cavity extent is decreased on both hydrofoils.

In the experiment, vortex cavitation appears at the trailing edge near the tip on both hydrofoils. Low pressure appears at the same position in the computation, but vortex cavitation

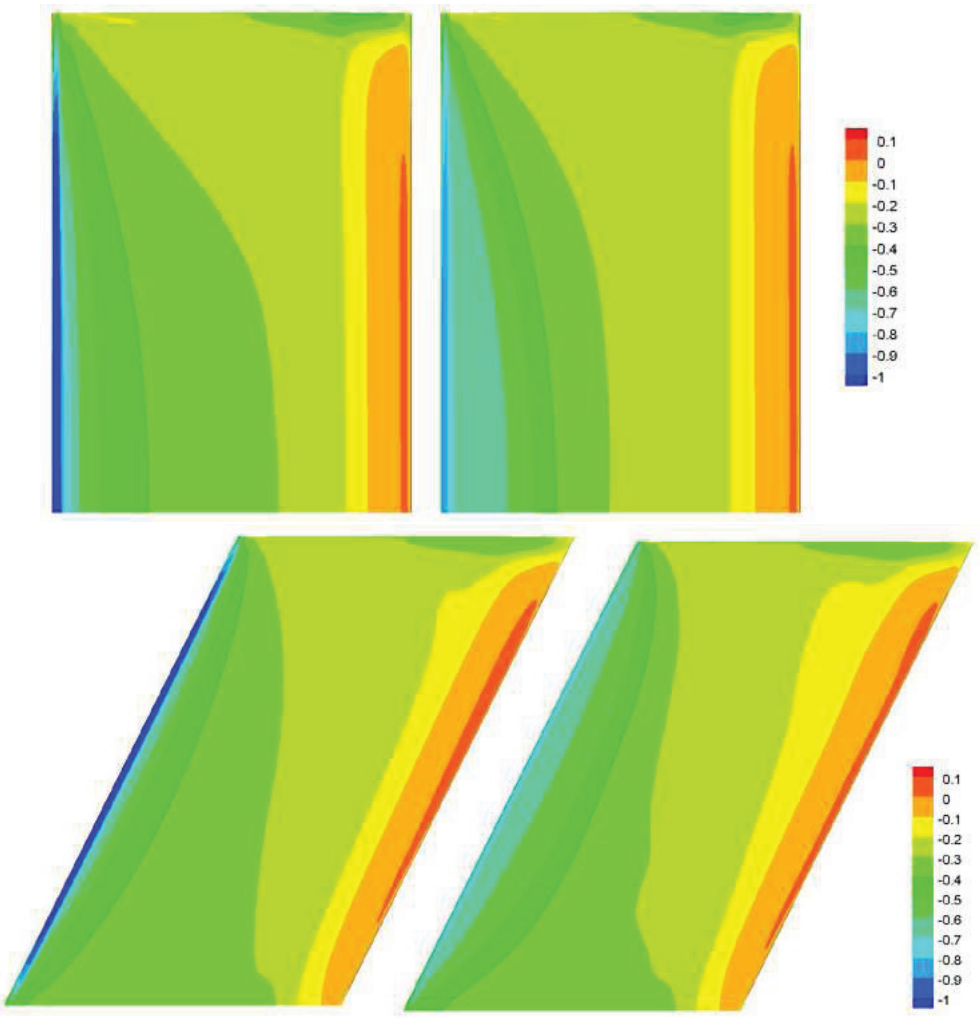

Figure 4.7: C_p on the suction surface for the fully-wetted (left column) and cavitating (right column) flows for $\alpha = 6^o, \sigma = 0.628$ on the non-swept hydrofoil (top) and for $\alpha = 6^o, \sigma = 0.585$ on the swept hydrofoil (bottom)

is not realized. It may be related to the difference in tip roundness and turbulent characteristics.

The distribution of C_p on the suction surface in Figure 4.7 is closely related to the cavity distribution. $C_p = -0.4 - -0.3$ corresponds to the iso-contour of $\alpha_v = 0.1$ in Figure 4.6. High suction pressure in the fully-wetted flow is lowered and the region of $-C_p$ around the cavitation number is more extended. The suction pressure in the region behind the cavity is slightly lower than in the same location for the fully-wetted flow.

The sectional distributions of $-C_p$ at two spanwise positions in Figure 4.8 do not show such a constant pressure region at $-C_p = \sigma$ as in 2D hydrofoil cases in the previous chapter, because sheet cavitation in this case is not intensive enough to generate a cavity consisting of dense vapor. $-C_p$ is gradually decreased at the cavity closure in the same way as α_v. On the non-swept hydrofoil, the decrease of $-C_p$ at $y/s_0 = 0.7$ is rather steep than at $y/s_0 = 0.4$. A lower slope at the cavity closure may be related to a rougher closure.

The comparison of the cavity extent in Figure 4.9 shows a reasonable agreement of the computed result with the experimental one, but the maximum chordwise extent from the computation is shorter by about $0.2C$ and $0.1C$ on the non-swept and swept hydrofoils, respectively. The cavity profile from the experiment in Figure 4.9 includes the scattering cloud cavity. When comparing the computed cavity extent to the steady sheet cavity, the difference in the maximum extent is less than $0.1C$ on both hydrofoils. The computed cavity at the tip of the swept hydrofoil is more extended, contrary to the shorter extent in the midspan.

While the converged value of V_v^* for $C_c = 0.5 \cdot 10^{-4}$ is between the maximum $V_{v,\max}^*$ and minimum $V_{v,\min}^*$ of V_v^* for $C_c = 10^{-4}$, the cavity extent for $C_c = 0.5 \cdot 10^{-4}$ is larger than those at $V_{v,\max}^*$ and $V_{v,\min}^*$ for $C_c = 10^{-4}$. As the 2D case in the previous chapter shows, the cavity closure can be more extended for a lower condensing rate. For $C_c = 10^{-4}$, the cavity closure fluctuates with the maximum amplitudes of $0.03C$ and $0.08C$ in chordwise extent for the non-swept and swept hydrofoils, respectively.

The iso-contours determined by different values of α_v for $C_c = 10^{-4}$ at $V_{v,\min}$ are also shown in Figure 4.9 (right). Since the vapor fraction is gradually decreased at the cavity closure, the iso-contour of a lower vapor fraction covers more area. The maximum cavity extent from $\alpha_v = 0.05$ is still shorter than that including the scattering cavitation from the experiment. The iso-contour from even a smaller value of α_v can be closer to the extent of scattering cavitation. At the tip on the swept hydrofoil, the extent from $\alpha_v = 0.05$ is further ahead, contrary to the rest of the span. It may be related to the difference in the tip flow.

For $C_c = 10^{-4}$, the maximum cavity extent corresponds to the minimum vapor volume $V_{v,\min}$ and vice versa. It is explained by the variation of the sectional vapor distribution in Figure 4.10. As the vapor volume is increased from $V_{v,\min}$, the cavity thickness is increased and the cavity extent is shortened. As the vapor volume is decreased, the cavity is sharpened and extended. While the duration between $V_{v,\max}$ and $V_{v,\min}$ is almost $0.5T$ for the swept

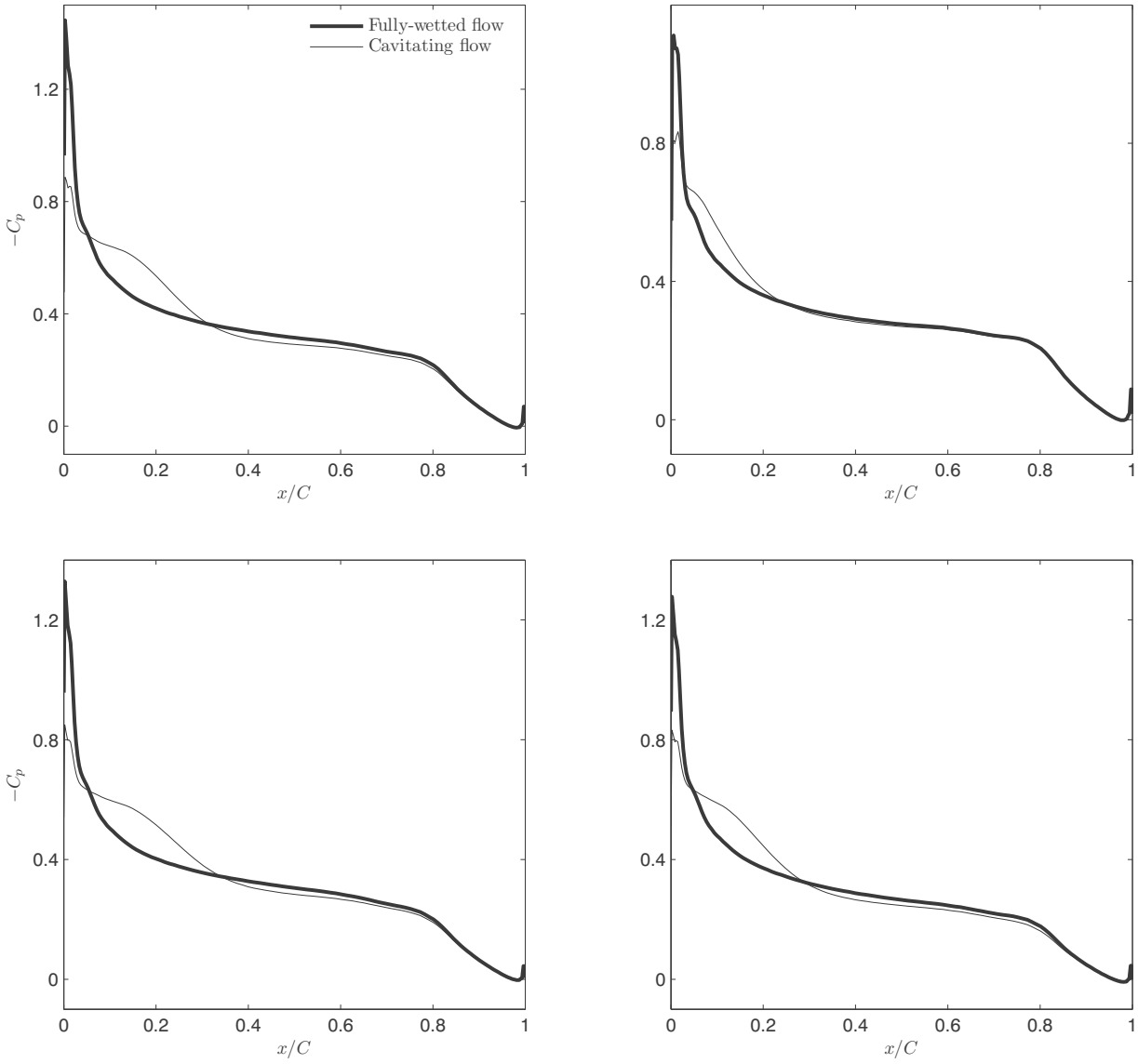

Figure 4.8: $-C_p$ on the suction surface for the fully-wetted and cavitating flows at $y/s_0 = 0.4$ (left column) and 0.7 (right column) for $\alpha = 6^o, \sigma = 0.628$ on the non-swept hydrofoil (top) and for $\alpha = 6^o, \sigma = 0.585$ on the swept hydrofoil (bottom)

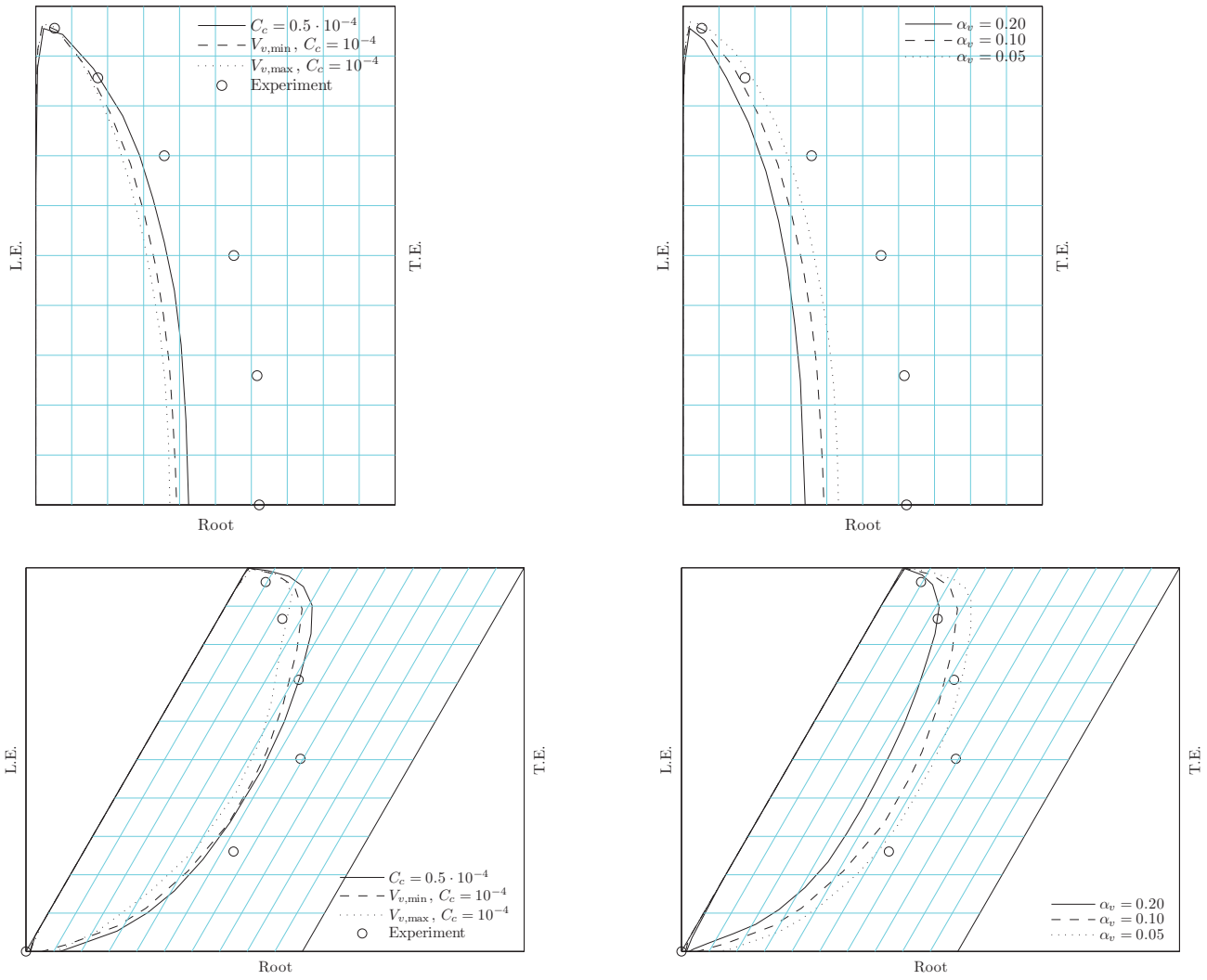

Figure 4.9: Cavity profiles from the experiment and computation with different values of C_c (left column) and with different values of α_v (right column) for $\alpha = 6^o, \sigma = 0.628$ on the non-swept hydrofoil (top) and for $\alpha = 6^o, \sigma = 0.585$ on the swept hydrofoil (bottom)

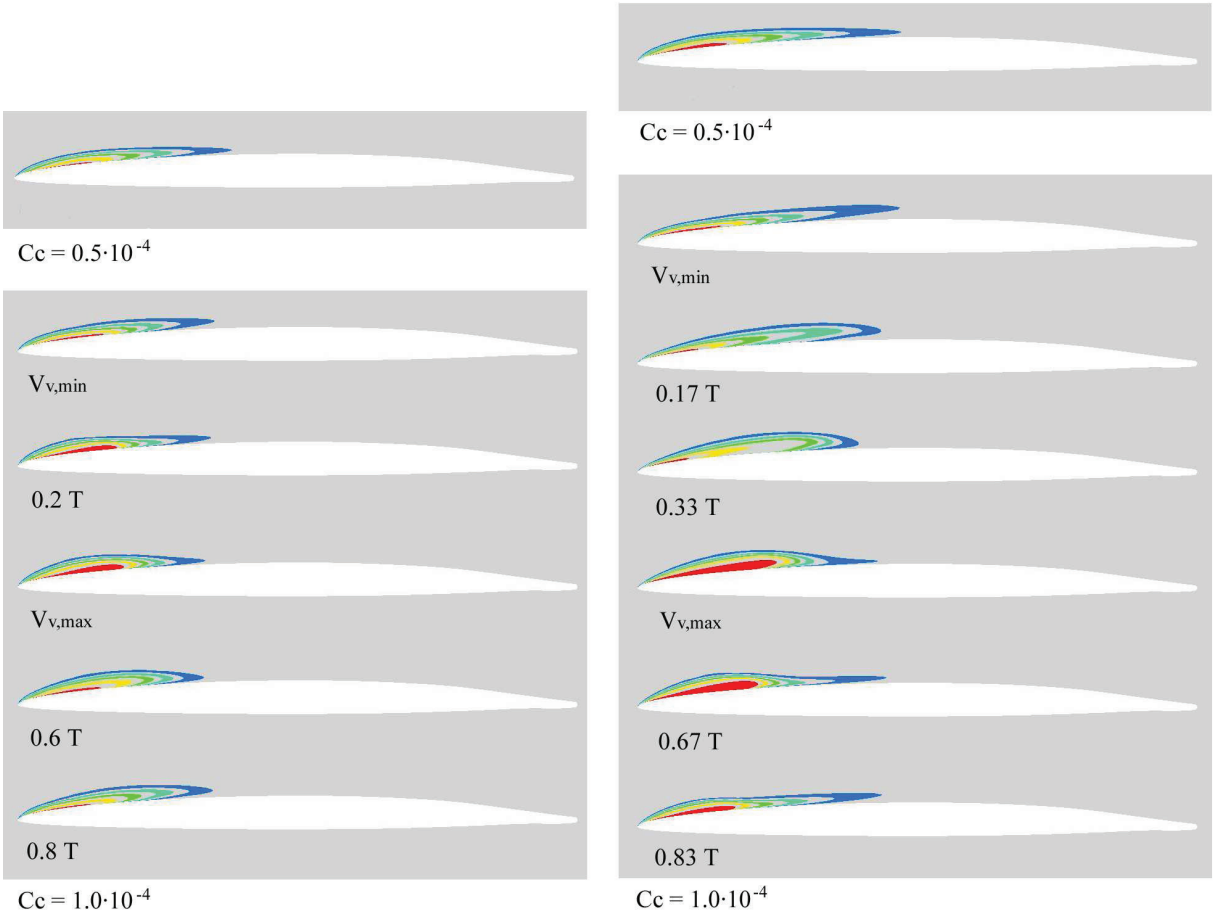

Figure 4.10: α_v at $y/s_0 = 0.7$ with two different values of C_c for $\alpha = 6^o, \sigma = 0.628$ on the non-swept hydrofoil (left column) and for $\alpha = 6^o, \sigma = 0.585$ on the swept hydrofoil (right column): outermost layer indicating $\alpha_v = 0.1$ with an interval of 0.1

hydrofoil, the increasing duration from $V_{v,\min}$ to $V_{v,\max}$ is $0.47T$ for the non-swept hydrofoil. α_v from the converged solution for $C_c = 0.5 \cdot 10^{-4}$ has a similar pattern with that at $V_{v,\min}$ for $C_c = 10^{-4}$.

Case 2

The next case is for a larger angle of incidence, $\alpha = 10^o, U_\infty = 6m/s, \sigma = 1.357$ with the non-swept hydrofoil and $\alpha = 10^o, U_\infty = 6m/s, \sigma = 1.396$ with the swept one. The computational grid has a stability problem for these cases, hence a coarse grid with twice the grid size and half the number of cells is used. The coefficients for the mass transfer rate are increased by six times to $C_e = 6.0$ and $C_c = 3.0 \cdot 10^{-4}$. Further increases of C_e and C_c with a constant value of C_e/C_c bring stability problems.

The dimensionless vapor volume on the non-swept hydrofoil in Figure 4.11 fluctuates periodically with $St = 1.108$. The amplitude of the vapor volume variation is gradually decreased to $\Delta V_v^* = 3.97 \cdot 10^{-3}$ and becomes steady. When the coefficient for the condensing rate is decreased to $C_c = 1.5 \cdot 10^{-4}$, the vapor volume is converged to $V_v^* = 4.45 \cdot 10^{-3}$, but it has intermittent irregular fluctuations.

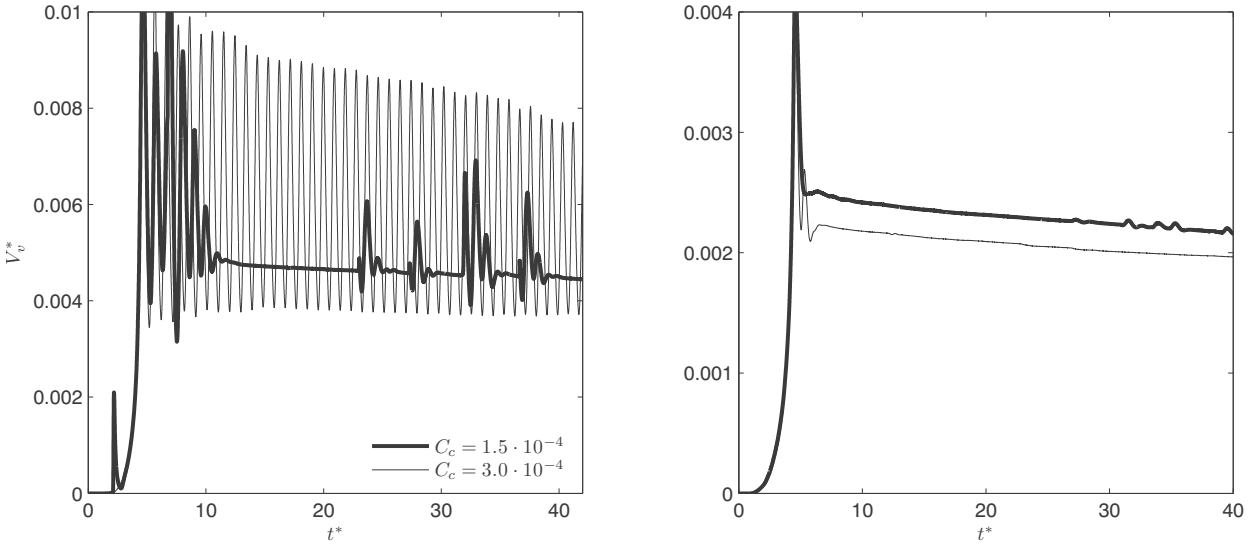

Figure 4.11: V_v^* as a function of t^* for $\alpha = 10^o, \sigma = 1.357$ on the non-swept hydrofoil (left) and for $\alpha = 10^o, \sigma = 1.396$ on the swept hydrofoil (right)

The cavitation on the swept hydrofoil is steady, converging to $V_v^* = 1.96 \cdot 10^{-3}$ and $2.16 \cdot 10^{-3}$ for $C_c = 3.0 \cdot 10^{-4}$ and $1.5 \cdot 10^{-4}$, respectively. The vapor volume is increased with small intermittent fluctuations for a lower value of C_c.

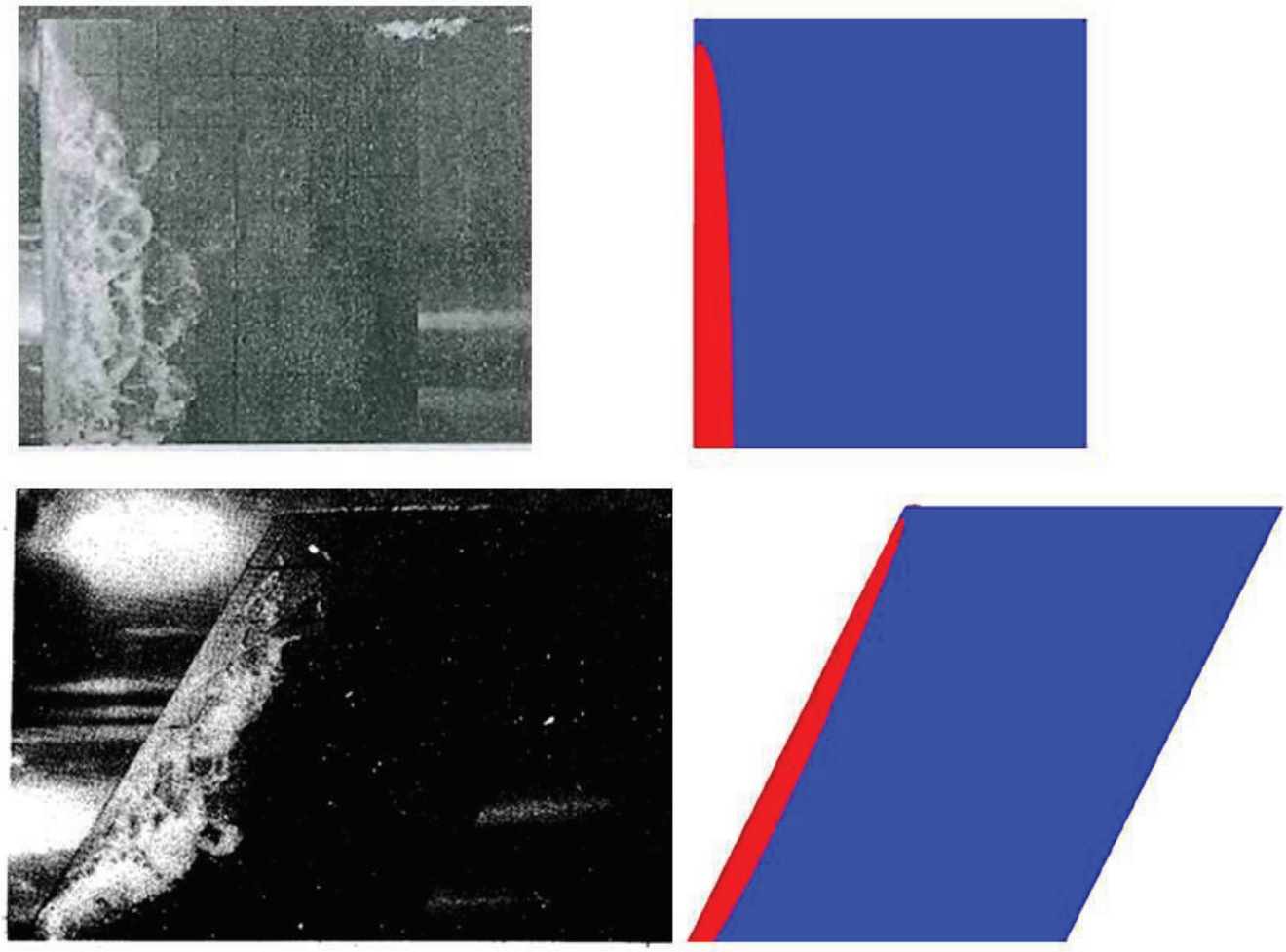

Figure 4.12: Snapshot from the experiment (Ukon, 1986) (left column) and iso-contour of $\alpha_v = 0.1$ from the computation (right column) for $\alpha = 10^o, \sigma = 1.357$ on the non-swept hydrofoil (top) and for $\alpha = 10^o, \sigma = 1.396$ on the swept hydrofoil (bottom)

Unsteady vortex core cavitation with cavity increasing and cavity break-off is reported on both hydrofoils in the experiment. While the computation shows unsteady cavitation on the non-swept hydrofoil, it does not appear on the swept hydrofoil, even though it is reported in the experiment that the unsteady phenomenon on the swept hydrofoil is more pronounced than on the non-swept hydrofoil.

The comparison between the snapshot from the experiment and the computed iso-contour of $\alpha_v = 0.1$ in Figure 4.12 shows that the cavity in the computation is less extended by $0.18C$ than in the experiment. The computation is made with $C_e = 6.0$ and $C_c = 3.0 \cdot 10^{-4}$. The maximum cavity extent is taken in the computed unsteady cavitation on the swept hydrofoil. When V_v is on the mid-point of the downslope from $V_{v,\max}$ to $V_{v,\max}$, the cavity extent is the maximum. Periodic characteristics like frequency and amplitude of the cavity extent variation from the experiment are not available. It is not reported on which stage of the unsteady cavitation the snapshot is taken.

The chordwise extent of the cavity on the non-swept hydrofoil is increased and the increasing rate is slowed down from the tip to the root in the similar way as for $\alpha = 6^o$. While the cavity surface in the experiment is smooth at the entire chordwise extent within 20% span from the tip, it is smooth at the fore part and rough from about $0.1C$ and the cavity is detached in scattering cloud cavitation at the closure in the rest of the span. The computed cavity covers about 50% of the sheet cavity from the experiment. Cavitation starts from 5% span from the tip, whereas it starts from the corner of the leading edge and the tip in the experiment. The computation does not realize cloud cavitation and tip vortex cavitation.

It is difficult to recognize the distribution of the glassy sheet cavity in the snapshot for the swept hydrofoil due to the image quality. The chordwise extent of the glassy cavity is increased from the tip to about 25% span. The cavity extent is more or less constant between 25% and 65% span and the portion of the rough cavity is increased. A small region of cloud cavitation appears at the cavity closure in about 60% span. The maximum cavity extent from the computation reaches 30% of that from the experiment. The cavity extent is increased from the tip to 65% span and it is decreased from there to the root.

In Figure 4.13, the comparison of the maximum and minimum extents $L_{c,\max}, L_{c,\min}$ on the non-swept hydrofoil for $C_c = 3.0 \cdot 10^{-4}$ shows a difference of $0.025C$ at the root and the difference is decreased from the root to the tip. The cavity distribution for $C_c = 1.5 \cdot 10^{-4}$ shows no significant difference from $L_{c,\max}$ for $C_c = 3.0 \cdot 10^{-4}$ within 40% span from the tip, but it is less extended than $L_{c,\max}$ in the rest of span. The cavity on the swept hydrofoil for $C_c = 1.5 \cdot 10^{-4}$ is a bit more extended near the tip and root than that for $C_c = 3.0 \cdot 10^{-4}$, but the maximum difference is $0.01C$.

The iso-contours of $\alpha_v = 0.05$ and 0.1 on the non-swept hydrofoil are more extended, by $0.022C$ and $0.011C$ at the root, than that of $\alpha_v = 0.2$ and the differences are slightly changed along the span. The iso-contours of $\alpha_v = 0.05$ and 0.1 on the swept hydrofoil are more extended, by $0.021C$ and $0.007C$, at the maximum extent. The change of the cavity extent by reducing the condensing rate or the volume fraction for defining the cavity contour is insignificant, compared to the difference from the experimental result.

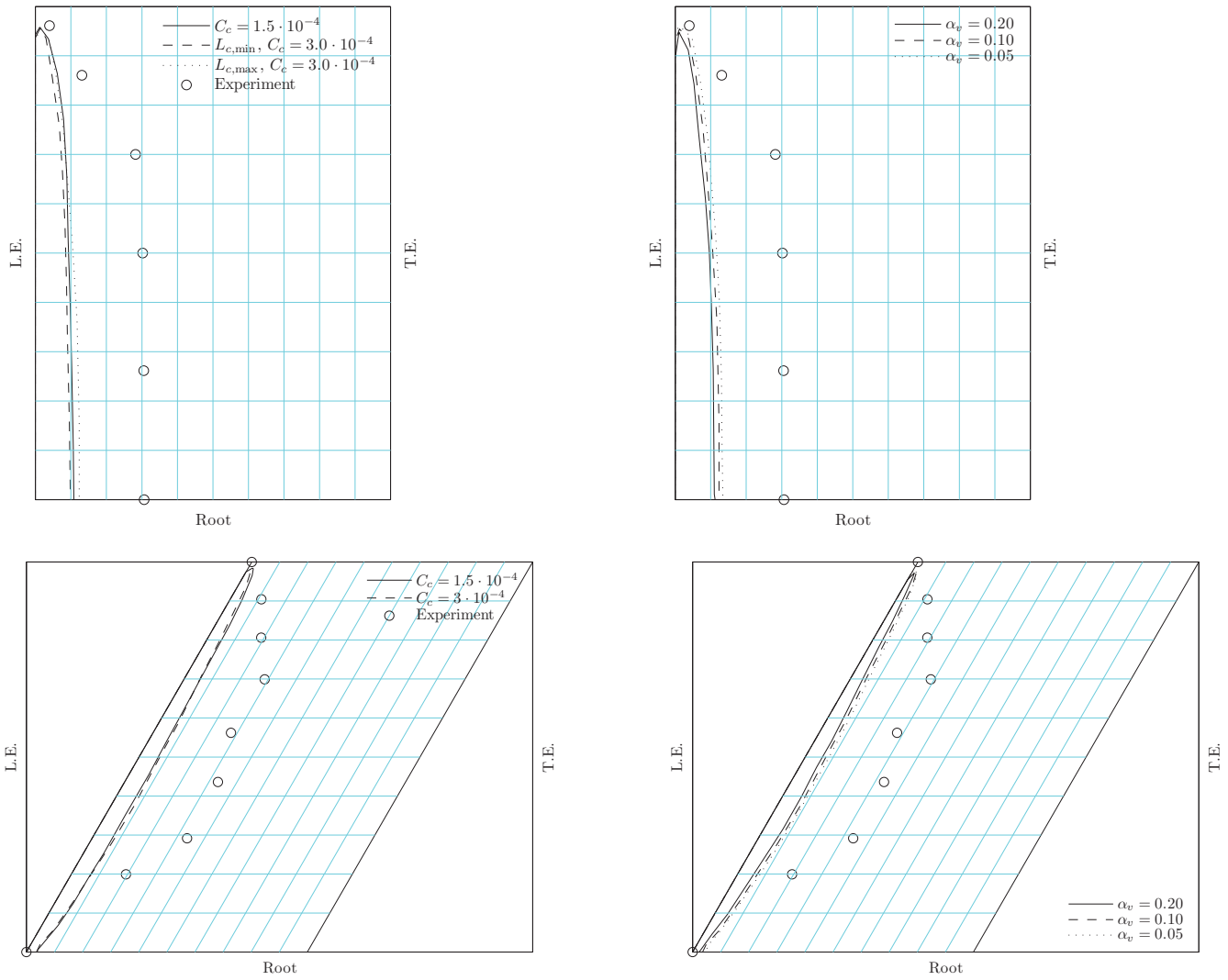

Figure 4.13: Cavity profiles from the experiment and computation with different values of C_c (left column) and with different values of α_v (right column) for $\alpha = 10^o, \sigma = 1.357$ on the non-swept hydrofoil (top) and for $\alpha = 10^o, \sigma = 1.396$ on the swept hydrofoil (bottom)

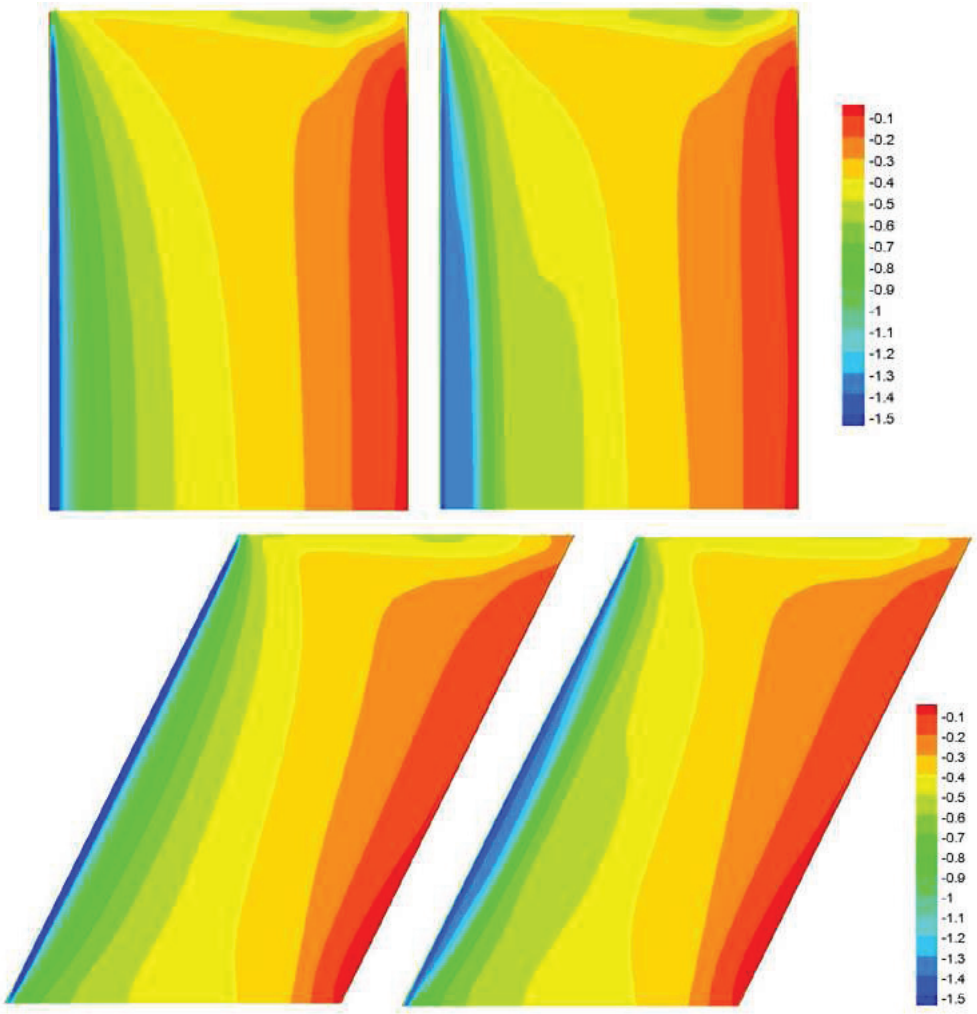

Figure 4.14: C_p on the suction surface for the fully-wetted (left column) and cavitating (right column) flows for $\alpha = 10^o, \sigma = 1.357$ on the non-swept hydrofoil (top) and for $\alpha = 10^o, \sigma = 1.396$ on the swept hydrofoil (bottom)

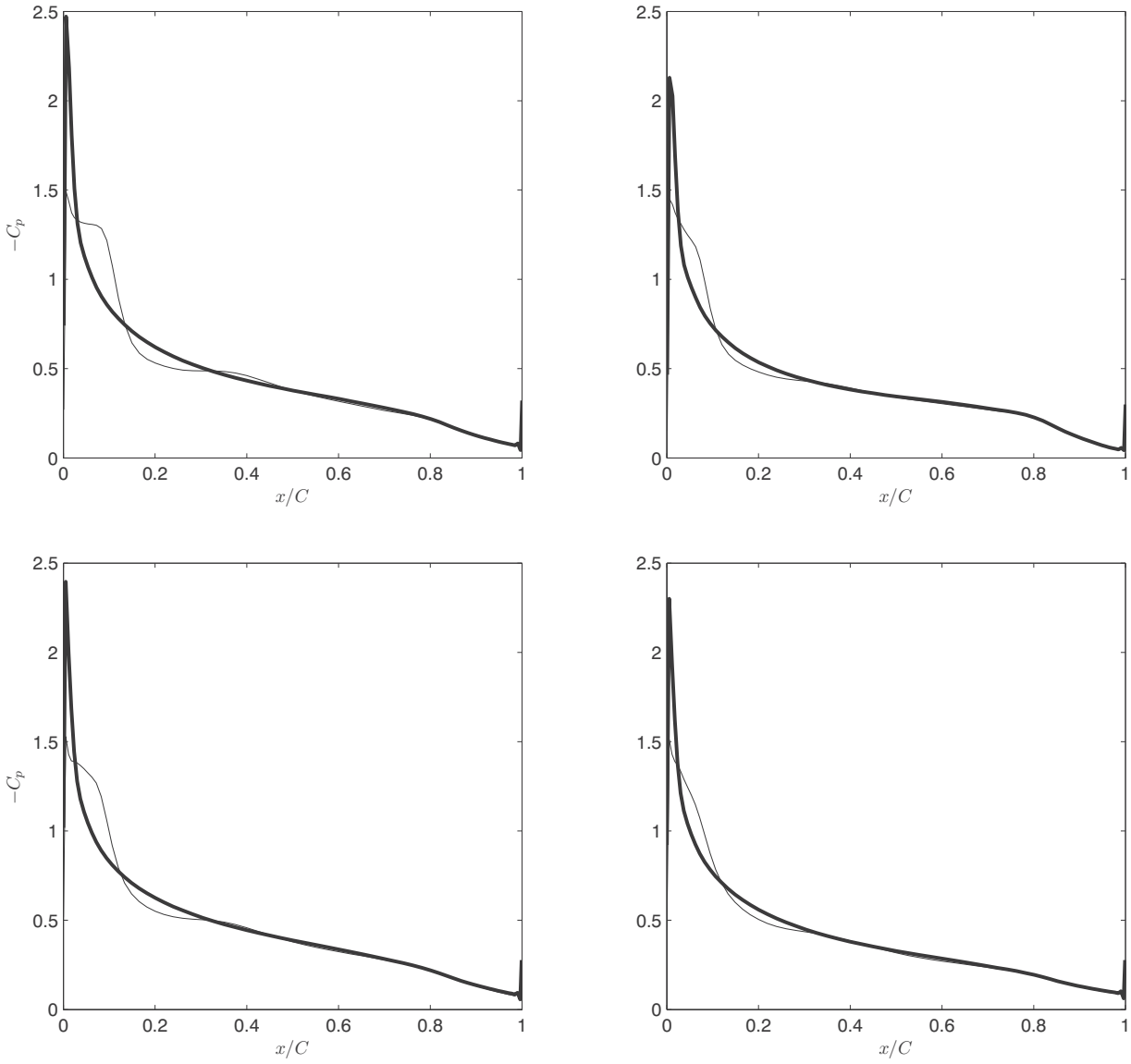

Figure 4.15: $-C_p$ on the suction surface for the fully-wetted and cavitating flows at $y/s_0 = 0.4$ (left column) and 0.7 (right column) for $\alpha = 10^o, \sigma = 1.357$ on the non-swept hydrofoil (top) and for $\alpha = 10^o, \sigma = 1.396$ on the swept hydrofoil (bottom)

It can be seen in Figure 4.14 that the high suction pressure is lowered and the region of the suction pressure near the vapor pressure is extended over the cavity region. The region of $C_p = -1.2$ agrees well with the cavity region. On the non-swept hydrofoil, the region of $C_p \simeq -\sigma$ is extended over 70% of the cavity extent within 50% span from the root and the sectional pressure distribution at $y/s_0 = 0.7$ in Figure 4.15 shows a constant pressure inside the dense vapor. When the vapor is not dense enough, the suction pressure inside the cavity is gradually decreased and the decrease becomes rapid at the cavity closure.

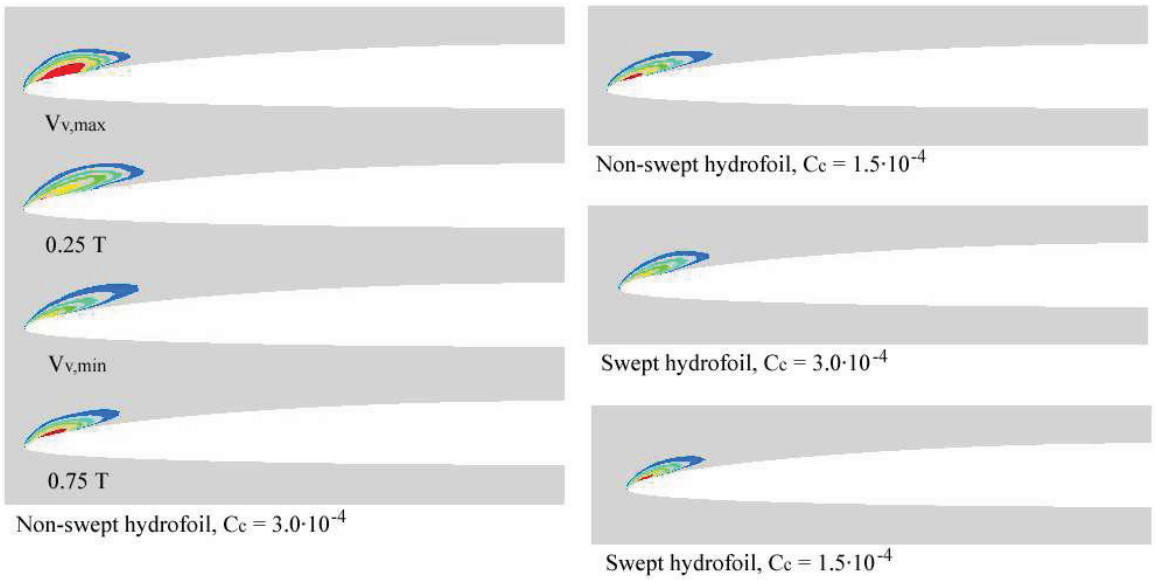

Figure 4.16: α_v at $y/s_0 = 0.7$ for $\alpha = 10^o, \sigma = 1.357$ on the non-swept hydrofoil and for $\alpha = 10^o, \sigma = 1.396$ on the swept hydrofoil: outermost layer indicating $\alpha_v = 0.1$ with an interval of 0.1

In Figure 4.16, the variation of the sectional vapor fraction distribution on the non-swept hydrofoil for $C_c = 3.0 \cdot 10^{-4}$ shows that the cavity is sharpened and stretched, as V_v is decreased from $V_{v,\max}$. The thickness and extent of the cavity are decreased from the mid-point of the decreasing duration. From $V_{v,\min}$, the extent is still decreased, but the thickness is increased. The extent is the shortest at the mid-point of the increasing duration. From there, the thickness and extent are increased. The α_v distribution for $C_c = 1.5 \cdot 10^{-4}$ is similar with that at $0.75T$ for $C_c = 3.0 \cdot 10^{-4}$. The cavity extent for $C_c = 1.5 \cdot 10^{-4}$ is more extended than that at $0.75T$ for $C_c = 3.0 \cdot 10^{-4}$, but less than at $0.25T$.

The cavity on the swept hydrofoil for $C_c = 3.0 \cdot 10^{-4}$ is thicker and longer than that for $C_c = 1.5 \cdot 10^{-4}$. The cavity core has a higher vapor fraction for a lower condensing rate, but the cavity is less extended due to the smaller thickness.

4.3 Conclusion for 3D cavitating flows

Numerical solutions are made for cavitating flows on 3D hydrofoils. The cases for two angles of attack on non-swept and swept hydrofoils are considered. The numerical solution is validated against the experiment only for the cavity profile. Periodic characteristics and variation patterns of unsteady cavitation from the computation are presented, but they are not compared to those from the experiment, because corresponding experimental data are not available.

The numerical solution shows qualitative and quantitative accuracy for steady and unsteady sheet cavitation for relatively low incident angles. The cavity extent is underestimated for relatively high incident angles. The numerical solution has low quantitative accuracy and stability problems for relatively high incident angles, but cavitation in such incidences is not general on open-water marine propellers. The numerical solution does not reproduce the scattering cloud and vortex cavitation appearing in the experiment. It may be related to the difference in turbulent characteristics.

While the total vapor volume for steady cavitation is less on the swept hydrofoil than that on the non-swept hydrofoil, the maximum vapor volume for unsteady cavitation is larger with a higher amplitude in variation. The sweep angle reduces the cavitation inception number, but it does not necessarily alleviate all cases of cavitation.

This page is intentionally left blank.

Chapter 5

Cavitating flows on marine propellers

We perform cavitation simulations on the conventional and highly-skewed propellers in the model scale and compare the numerical results with the experimental results from the cavitation tunnel tests. We perform simulations in the open-water and behind-hull conditions. The wake field behind the ship hull is generated by the non-homogeneously loaded actuator disk.

5.1 Propeller models

We consider the conventional and highly-skewed propellers used on the EU research project Leading Edge. The cavitation tests on these propeller models have been conducted on this project.

Both propellers are right-turning with four blades. The highly-skewed propeller is designed for a twin-screw ship. The propellers are inward-turning and the propeller on the port side is considered in the computation. The model-scale diameter is $D = 0.233m$ and $0.281m$ for the conventional and highly-skewed propellers, respectively. The conventional propeller is fixed-pitch with a pitch ratio of $P_{0.7R}/D = 0.701$. The highly-skewed propeller is controllable-pitch and the design pitch ratio of $P_{0.7R}/D = 1.224$ is considered. Main particulars for the propeller geometries are provided in Appendix A.4.

The computational model for the open-water condition is made for a single blade in a model scale. The computational domain for the conventional propeller in Figure 5.2 (top) is a 1/4 sphere consisting of an O-O grid topology in the near field and a H-C grid topology in the far field. The O-O topology allows the near-field mesh to be smooth around the propeller surface and the H-C topology makes two cyclic boundaries match each other point-to-point.

The cyclic boundary condition is applied to two surfaces on the azimuth plane. The frame of the flow domain rotates in the opposite direction to the actual propeller rotation. In the

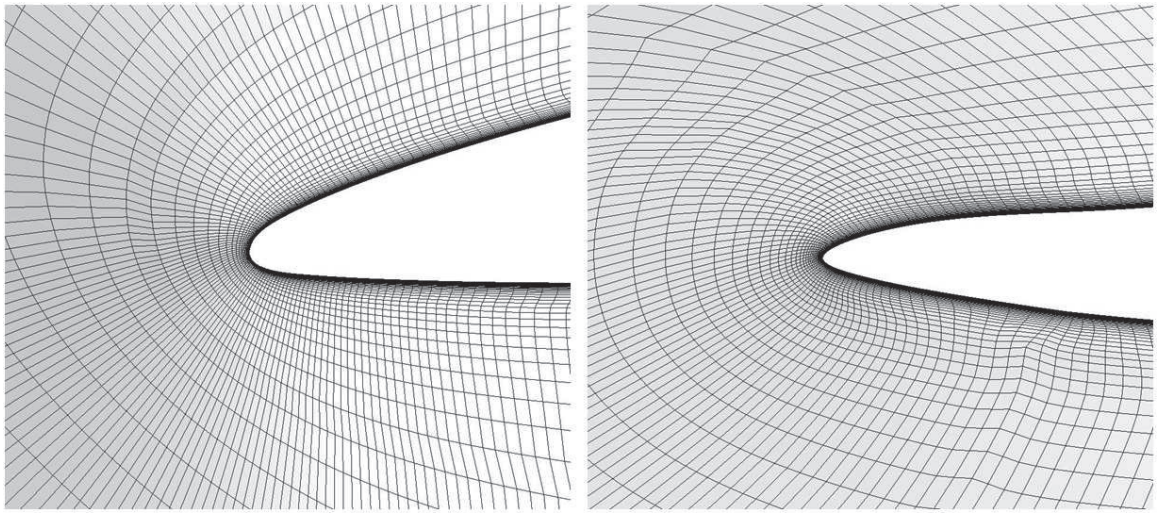

Figure 5.1: O-O grid around the leading edge of $r \simeq 0.5R$ for the conventional (left) and highly-skewed (right) propellers

present computational models, the frame rotates clockwise along the z-axis and the right side is the outlet cyclic boundary.

The O-O grid around the propeller surface in Figure 5.1 shows good orthogonality and smooth variation of the grid size. Grid size is contracted around the propeller edge to resolve the curvature well. Two cyclic boundaries are right-angled to be converted to a four-bladed model by making copies for the computation with inhomogeneous inflow. The transitional domain between the O-O and H-C topologies is meshed by interpolation with increasing the grid size hyperbolically from the near field to the far field. To avoid excessive skewness of the finite volume elements, the surface mesh is twisted chordwisely, as the block boundary in a thick line shows in Figure 5.2 (bottom). The surface mesh on the highly-skewed propeller in Figure 5.3 (bottom) is twisted in both spanwise and chordwise directions due to the high skewness. The full domain extends about $5D$ from the propeller hub. The axial inflow is in the positive z-direction.

The computational domain for the highly-skewed propeller in Figure 5.3 (top) is a 1/4 cylinder. Although the cylindrical domain has a redundant computational space, compared to the spherical domain, it has separate inlet and cyclic boundaries to avoid the risk that the inlet boundary has a conflict with rotating perturbation. In the spherical domain for the conventional propeller, the pressure in the inlet boundary can be perturbed by the rotating flow. When the perturbed inlet pressure is used as an ambient pressure, it can bring a problem in estimating the cavitation number.

The computational grids for the conventional and highly-skewed propellers consists of 12 and 18 blocks, respectively. The number of cells in each block is $64^3 = 2.6 \cdot 10^5$ with meshing each dimension of the block into 64 grids. The total number of cells is $3.1 \cdot 10^6$ and $4.7 \cdot 10^6$ for

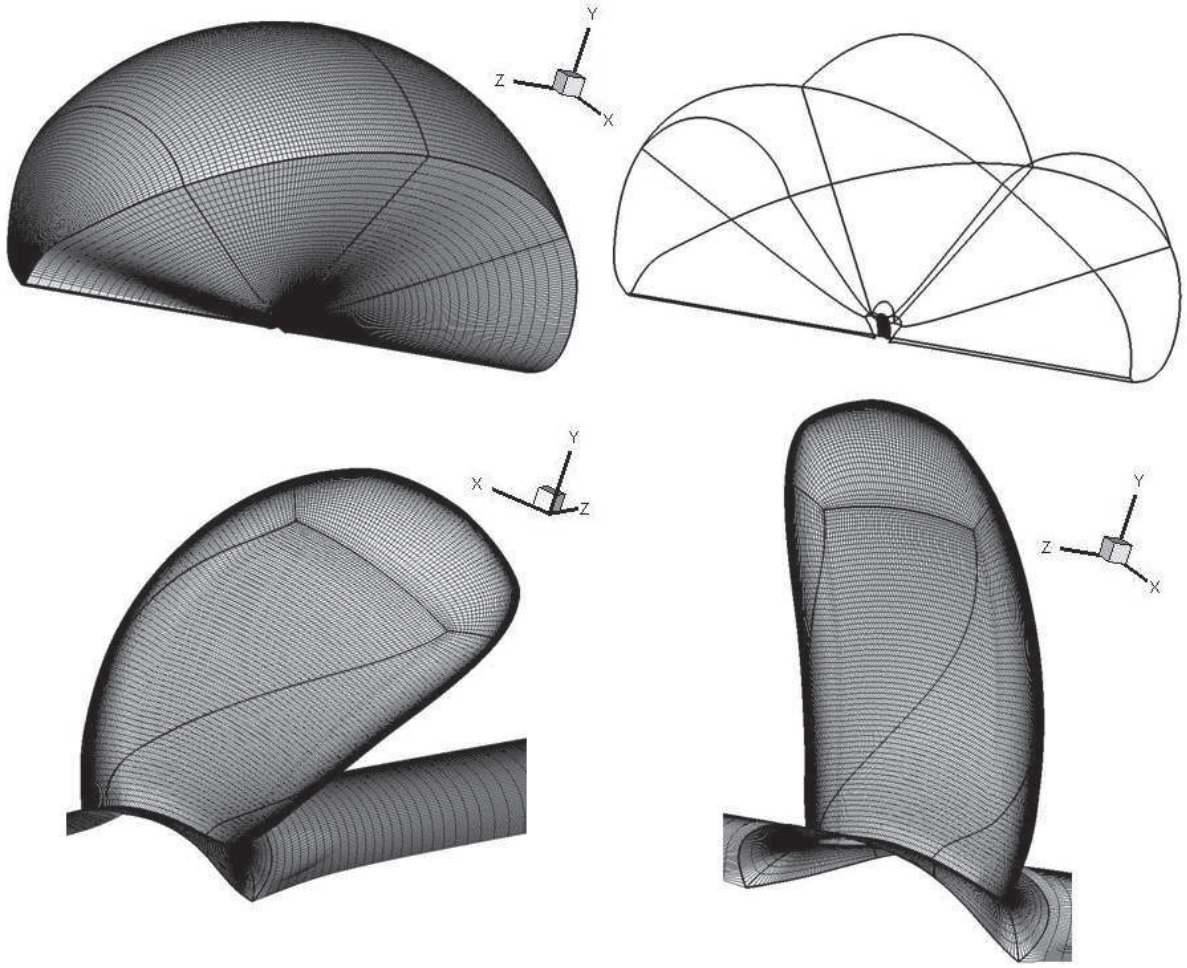

Figure 5.2: Computational grid (top left) for the conventional propeller, block structure (top right) and surface mesh on the suction side (bottom left) and pressure side (bottom right)

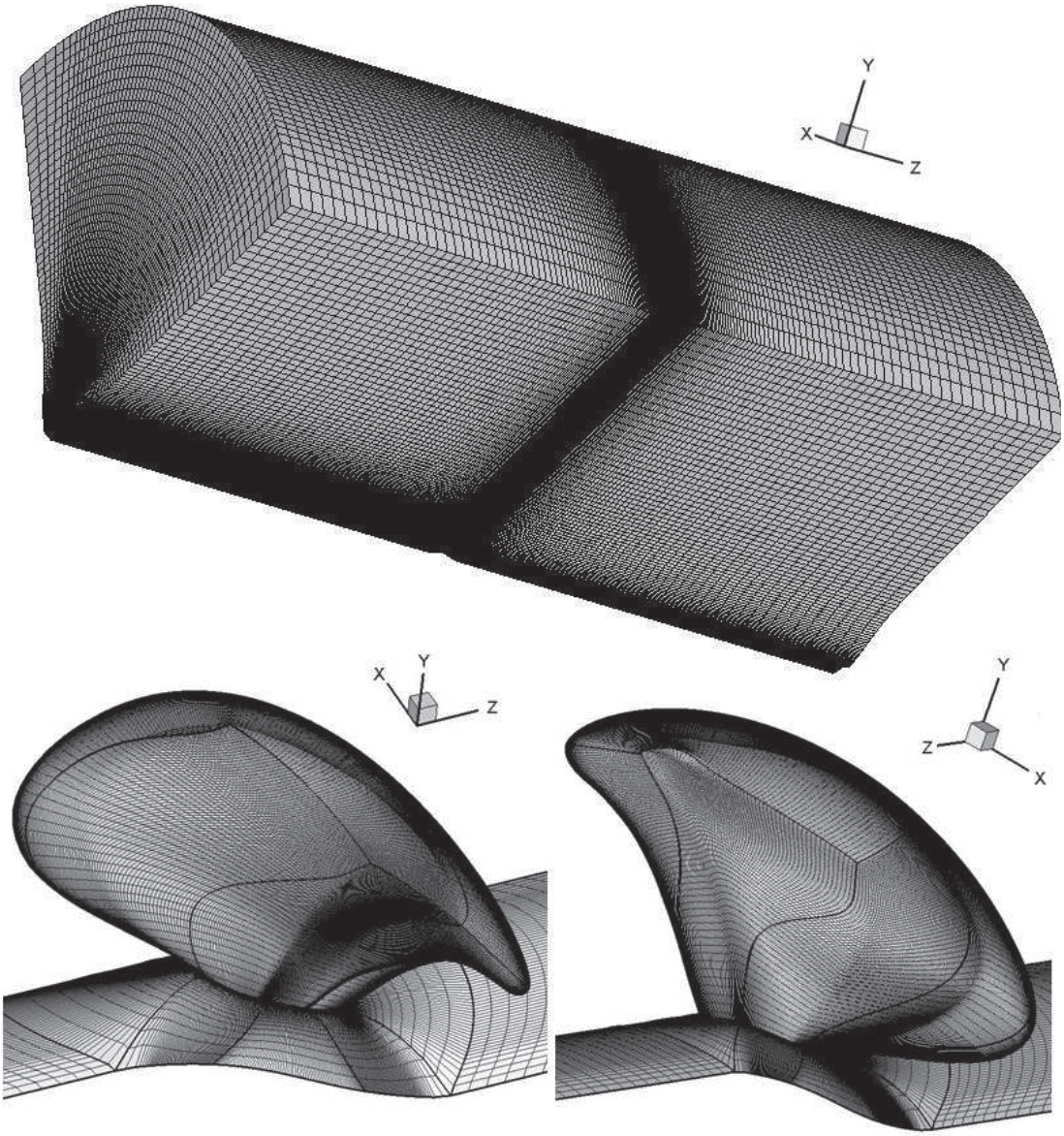

Figure 5.3: Computational grid (top) for the highly-skewed propeller and surface mesh on the suction side (bottom left) and pressure side (bottom right)

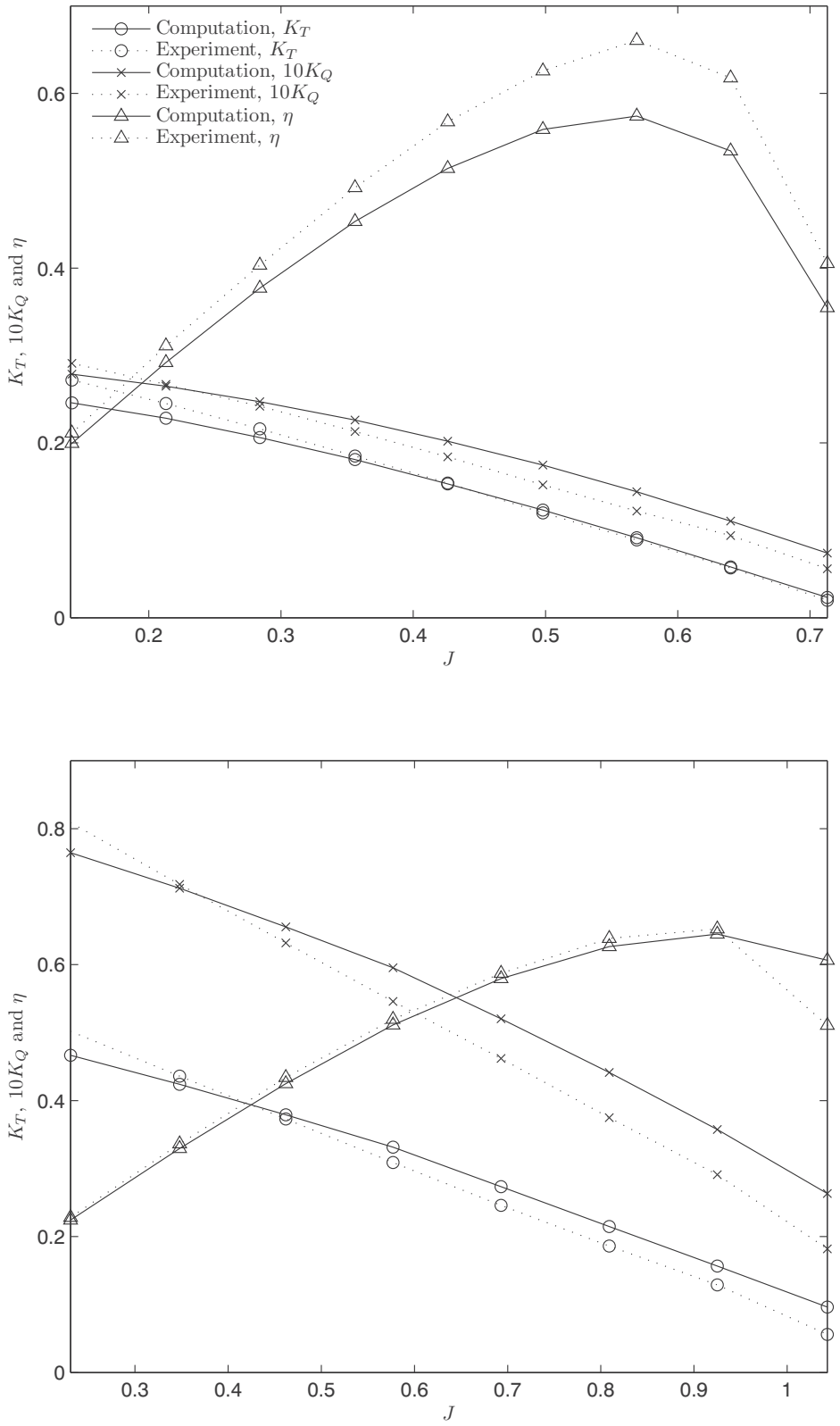

Figure 5.4: K_T, K_Q and η in open water and fully wetted flows for the conventional (top) and highly-skewed (bottom) propellers

the conventional and highly-skewed propellers, respectively. The first-cell height is $3 \cdot 10^{-6}$ and $1 \cdot 10^{-6}$, which result in $y^+ \simeq 0.1$ and 0.5, respectively.

The propeller hub is replaced by a cylinder with the same diameter extending over the entire domain, because force and moment acting only on the propeller blades are recorded in the model test by subtracting those acting on the bare hub from the total measurements. While the propeller surface has no-slip wall boundary condition, free-slip condition is applied to the hub cylinder surface.

In Figure 5.4, thrust coefficient K_T, torque coefficient K_Q and efficiency η from the computation are compared to those from the experiment. The experimental data are from the open water tests at the SSPA towing tank (Li and Lundstrom, 2002). Steady-state computations are made. The same rotation rate of $N = 14rps$ as in the experiment is applied to the computation. The uniform inflow velocity V in the computation is varied according to the advance ratio J in the same way for the advance speed of the test rig in the experiment. The non-dimensional variables are based not on the axial velocity but on the angular velocity as follows

$$K_T = \frac{T}{\rho_l N^2 D^4}, \qquad K_Q = \frac{Q}{\rho_l N^2 D^5}, \qquad \eta = \frac{J}{2\pi}\frac{K_T}{K_Q},$$
$$J = \frac{V}{N\,D}, \qquad \sigma_N = \frac{p_\infty - p_v}{0.5\rho_l N^2 D^2}, \qquad C_p = \frac{p - p_\infty}{0.5\rho_l N^2 D^2} \tag{5.1}$$

The comparison shows acceptable agreements in the range of J near the reference condition of the cavitation inception tests i.e. $J = 0.4 - 0.5$ and $0.75 - 0.85$ for the conventional and highly-skewed propellers, respectively. The reference loading is $K_T = 0.152$ and 0.176, which correspond to $J = 0.431$ and 0.829 in the model test. The discrepancy in K_T at the nearest point to the reference condition is 0.6% and 9.8% for the conventional and highly-skewed propellers, respectively. The discrepancy in K_Q is more than 15% for both propellers. K_Q from the computation is larger in most range than that from the experiment. Bulten and Oprea (2005) relate the discrepancy in K_Q to the overestimation of drag force due to an error in the evaluation of the pressure at the stagnation point. The discrepancies in K_T and K_Q are larger for the highly-skewed propeller probably due to the difference of the discretized geometry from the propeller model and the more complicated turbulent components corresponding to the complex geometry.

As J is reduced below 0.3, the deviations in K_T and K_Q are increased. The deviation at a lower value of J may be because higher gradients of flow variables at a higher loading are not resolved sufficiently by the applied grid. As J is increased, the deviations are constant for the conventional propeller and slowly increased for the highly-skewed propeller. The deviation at a higher value of J may be related to an increase in y^+ corresponding to an increase in V.

5.2 Open-water cavitating flows

Conventional propeller

We consider a case of the open-water cavitating flow on the conventional propeller for $J = 0.447, \sigma_N = 1.60$. The cavitation test on the conventional propeller has been conducted in the SSPA high-speed cavitation tunnel with a tunnel length of $2.5m$ and a $1m$-diameter circular section (Li and Lundstrom, 2002). Since the experiment is intended for detecting cavitation inception, cavitation in this case is not so prevailing over the blade surface.

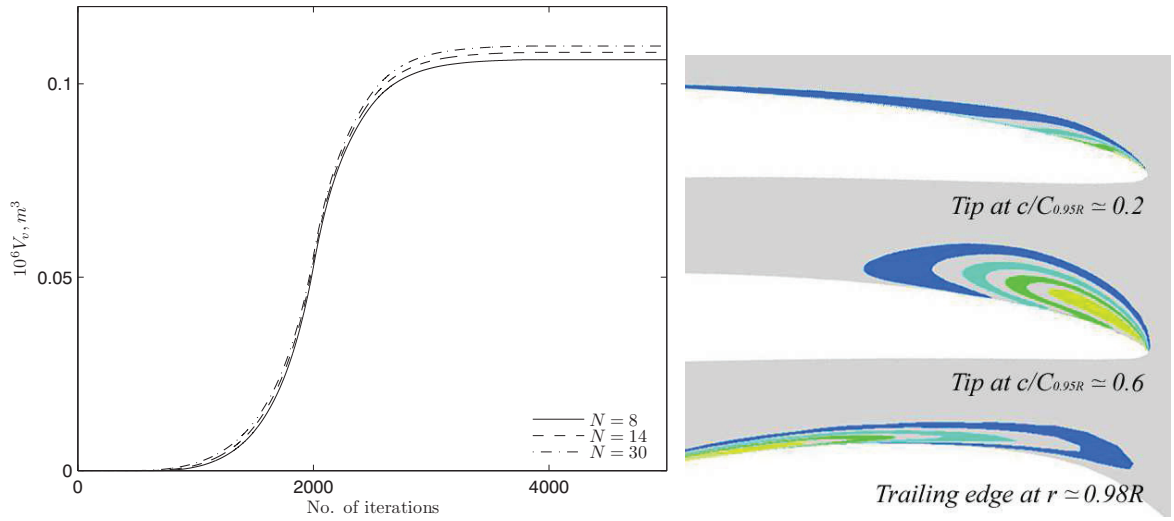

Figure 5.5: Total vapor volume as a function of iterations (left) with different values of N and α_v (right column) on the cross sections perpendicular to the tangential direction at $c/C_{0.95R} \simeq 0.2$ (top), 0.6 (middle) and perpendicular to the radial direction at $r \simeq 0.98R$ (bottom) on the conventional propeller for $J = 0.447, \sigma_N = 1.60$: outermost layer indicating $\alpha_v = 0.1$ with an interval of 0.1

The applied value of N is not stated in the experiment report, hence we apply three different values $N = 8, 14, 30rps$ to the computation. A steady-state computation is made with the same numerical properties as in the previous chapter. The solution is converged with the maximum normalized residual of less than 10^{-3}. The total vapor volume V_v in Figure 5.5 (left) is converged to a higher value for a higher rotation rate. Although J is fixed, higher values of N and V reduce the viscous drag, which contributes to more cavitation.

The computed results in Table 5.1 show that the reduced viscous drag leads to an increase in K_T and a decrease in K_Q, as Rn is increased for a higher value of N. When $N = 8rps$ is increased to $30rps$, the increase in K_T is 0.8% and the decrease in K_Q is 4.3% for the fully wetted flow. Since the drag is more effective on the torque, the change in K_Q is larger than that in K_T.

In the cavitating flow, K_T is decreased and K_Q is increased due to the increased form drag. The decrease in K_T is 0.2% and the increase in K_Q is 4.5% for $N = 8rps$. The sheet cavitation leads to the increased suction pressure, which contributes to the increase in K_T, hence the decrease due to the form drag in K_T becomes less. A higher value of N results in a stronger cavitation with more suction pressure, therefore K_T for $N = 30rps$ is not changed.

While K_T and K_Q from the open-water propulsion test have small differences of less than 0.5% from the computed results for $N = 14rps$, the difference of the computed K_T in the cavitating flow for $N = 30rps$ from the cavitation tunnel test result is 4.3%. Either a higher rotation rate or the wall interference in the cavitation tunnel test can lead to an increase in K_T.

	Fully wetted flow		Cavitating flow	
	K_T	K_Q	K_T	K_Q
Computation for $N = 8rps$	0.1443	0.01978	0.1440	0.02066
Computation for $N = 14rps$	0.1448	0.01940	0.1446	0.01992
Computation for $N = 30rps$	0.1454	0.01897	0.1454	0.01935
Open-water propulsion test	0.1444	0.01939	-	-
Open-water cavitation test	-	-	0.1520	-

Table 5.1: K_T and K_Q with different values of N on the fully wetted and cavitating flows around the conventional propeller for $J = 0.447$

In Figure 5.6, the iso-contour of $\alpha_v = 0.1$ from the computation with $N = 14rps$ is compared to the snapshot from the experiment. The open-water computation is conducted for one blade and the single-blade result is copied just for presenting the cavitation pattern on the whole propeller corresponding to the snapshot.

The distribution of the sheet cavity from the computation has a good agreement with that from the experiment. In the experiment, the sheet cavitation continues to be tip vortex cavitation and the vortex cavitation is extended to a quarter of a rotation. In the computation, the sheet cavitation is converted to the vortex cavitation, but the vortex cavitation is not extended from the blade tip. It is probably because the vortex flow with a low pressure core is not precisely generated due to a relatively low grid resolution at a distance from the propeller surface.

The pressure distribution on the suction side in the cavitating flow is compared with that in the fully wetted flow in Figure 5.7. In the cavitating flow, the suction peak at the tip is a bit lowered and the low pressure region of $C_p < -1.2$ is slightly more extended along the tip to the trailing edge, but the low pressure near the vapor pressure is not extended over the sheet cavity region, because the dense vapor of $\alpha_v > 0.5$ is not formed inside the sheet cavity, as shown in Figure 5.5 (right).

The chordwise distribution of C_p at $r = 0.95R$ on the suction side in Figure 5.8 does not show significant differences, although the sheet cavity is extended from the leading edge to $0.14C_{0.95R}$. C_p at $r = 0.98R$ shows that the suction peak is lowered and the low pressure

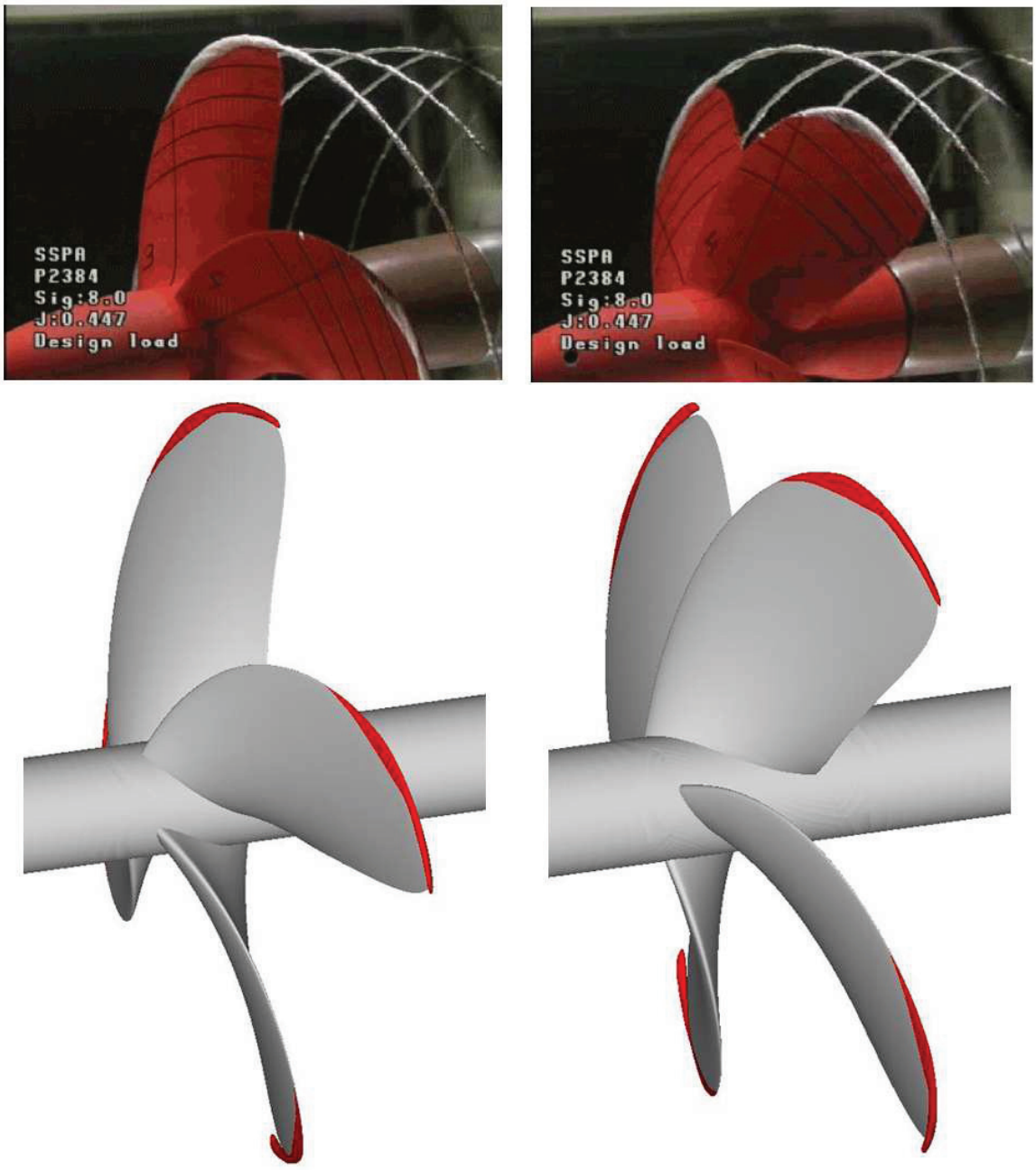

Figure 5.6: Snapshot from the experiment (Li and Lundstrom, 2002) (top) and iso-contour of $\alpha_v = 0.1$ from the computation (bottom) on the conventional propeller for $J = 0.447, \sigma_N = 1.60, N = 14rps$

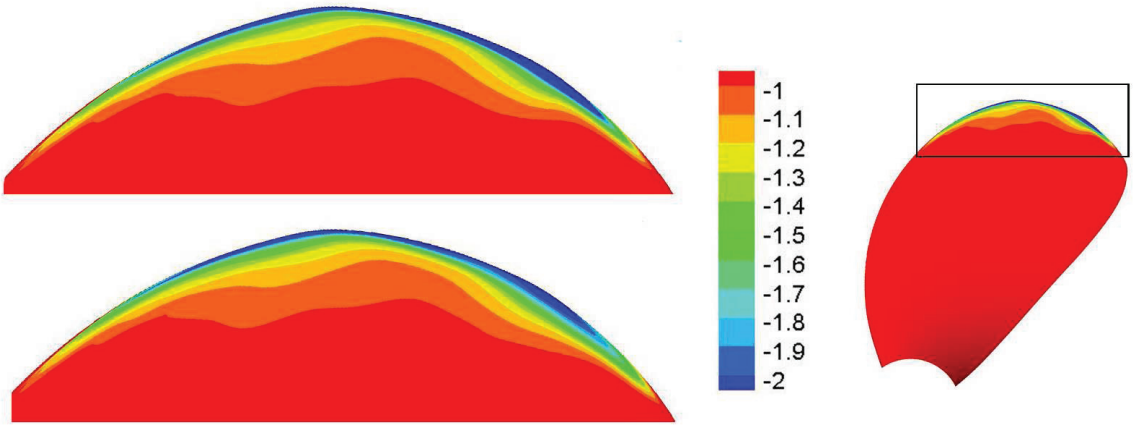

Figure 5.7: C_p on the suction side of the conventional propeller blade in the fully wetted (top) and cavitating (bottom) flows for $J = 0.447$

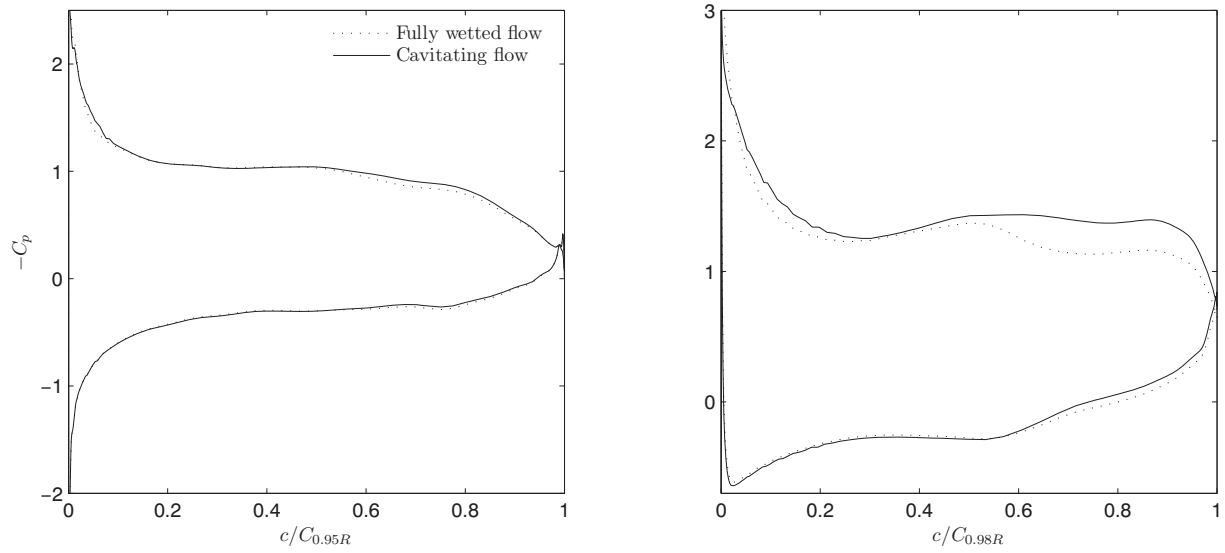

Figure 5.8: C_p on the blade surface of the conventional propeller at $r = 0.95R$ (left) and $0.98R$ (right) for $J = 0.447$

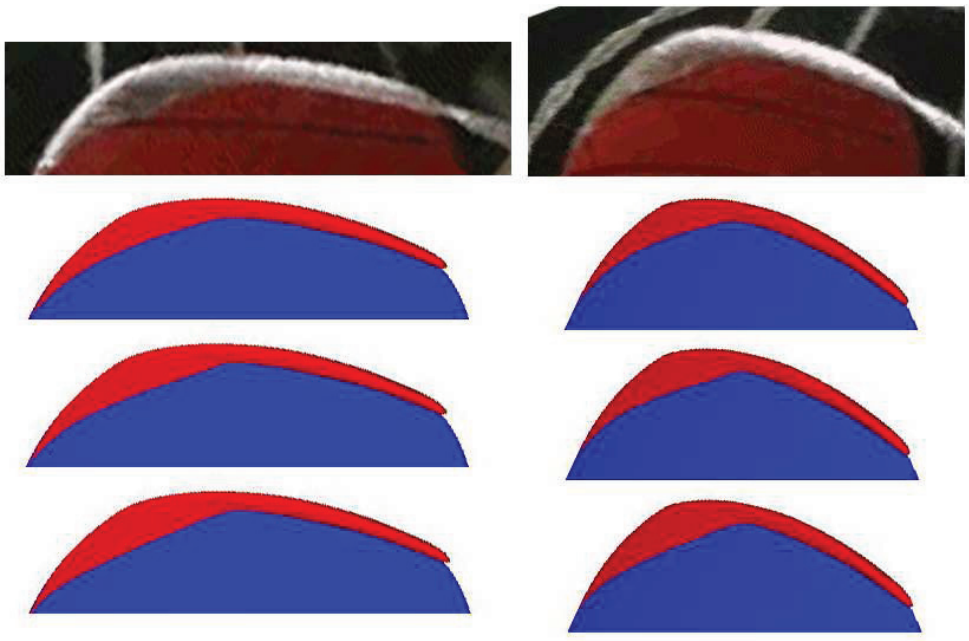

Figure 5.9: Cavity profiles from the experiment (topmost) and from the computation with $N = 8, 14, 30rps$ (from top to bottom) on the conventional propeller for $J = 0.447, \sigma_N = 1.60$ in different viewing angles (left and right columns)

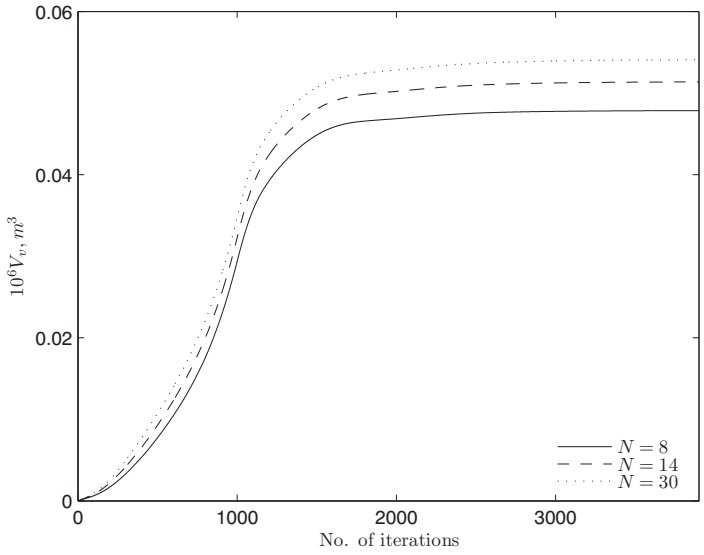

Figure 5.10: Total vapor volume as a function of iterations with different values of N on the highly-skewed propeller for $J = 0.603, \sigma_n = 2.271$

region at the leading edge is a bit extended. In the aft half of the chord, a constant pressure of $C_p \simeq -1.4$ appears on the suction side due to the effect of the tip vortex cavitation and C_p on the pressure side is slightly lowered.

The comparison of the iso-contours for different values of N in Figure 5.9 shows that the sheet cavity is more extended along the flow direction for a higher rotation rate, but the thickness and extent of the vortex cavity are not changed. The quantitative difference in the sheet cavity extent is so small, but the difference in the cavity distribution can be noticed by tracking the varying pattern of the chordwise extent. The sheet cavity extent for $N = 14rps$ has a better agreement with the snapshot than those for $N = 8, 30rps$. It does not imply that $N = 14rps$ is closer to N in the experiment, but that the turbulent characteristics for $N = 14rps$ are closer to those in the experiment.

Highly-skewed propeller

We consider a case of the open-water cavitating flow on the highly-skewed propeller for $J = 0.603, \sigma_n = 2.271$. The cavitation test on the highly-skewed propeller have been conducted in the HSVA medium cavitation tunnel with a length of $2.2m$ and a $0.57m$ square section (Lydorf, 2005).

While the highest rotation rate of $N = 30rps$ in this facility is applied to the tunnel test to minimize scale effects, the computations are made with three different values of N for a fixed value of J in the same way as in the previous computations for the conventional propeller, to investigate the effects of Rn on the cavitation according to N.

Figure 5.10 shows that the converged value of the total vapor volume is increased for a higher rotation rate. The increase of V_v from $N = 8rps$ is 7.4% for $N = 14rps$ and 13.0% for $N = 30rps$. It also shows the viscous drag effects on the cavitation.

	Fully wetted flow		Cavitating flow	
	K_T	K_Q	K_T	K_Q
Computation for $N = 8rps$	0.3110	0.05765	0.3108	0.05802
Computation for $N = 14rps$	0.3127	0.05709	0.3127	0.05740
Computation for $N = 30rps$	0.3151	0.05642	0.3154	0.05671
Open-water propulsion test	0.2949	0.05272	-	-
Open-water cavitation test	-	-	0.3224	-

Table 5.2: K_T and K_Q with different values of N on the fully wetted and cavitating flows around the highly-skewed propeller for $J = 0.603$

As N is increased, K_T is increased and K_Q is decreased due to the reduced viscous drag in the same way as for the conventional propeller. When N is increased from $8rps$ to $30rps$, the increase in K_T is 1.3% and the decrease in K_Q is 2.1% in the fully wetted flow. While the change magnitude in K_Q is relatively large compared to that in K_T on the conventional

propeller, the difference in the change magnitude becomes smaller on the highly-skewed propeller due to the skewness of the blade geometry.

K_T in the cavitating flow has a decrease for $N = 8rps$ and an increase for $N = 30rps$, but these changes are as small as less than 0.1%. The more extended sheet cavity for $N = 30rps$ leads to more suction pressure, which results in the increase in K_T. K_Q in the cavitating flow has a small increase of $0.5 - 0.6\%$.

K_T from the cavitation test is 9.3% larger than that from the propulsion test. Such a difference in K_T may be caused by the higher Rn, the increased suction pressure corresponding to the sheet cavitation and the wall interference in the cavitation tunnel. The difference in this case is more pronounced than the case for the conventional propeller, because the sheet cavity is more extended, and the higher ratio of the propeller disk area to the tunnel section area and the higher value of J can lead to more wall interference.

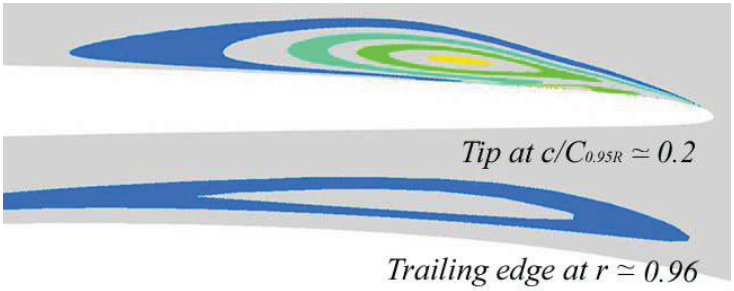

Figure 5.11: α_v on the cross sections perpendicular to the tangential direction at $c/C_{0.95R} \simeq 0.5$ (top) and perpendicular to the radial direction at $r \simeq 0.96R$ (bottom) on the highly-skewed propeller for $J = 0.603, \sigma_N = 2.271$: outermost layer indicating $\alpha_v = 0.1$ with an interval of 0.1

A snapshot from the experiment is compared with the computed iso-contour in Figure 5.12. In the experiment, sheet cavitation starts from the leading edge at $r \simeq 0.72R$ and it continues along the blade edge. As the sheet cavity is detached from the blade surface, it is extended in a form of tip vortex cavitation. In the computation, cavitation starts at an inner radius of $r \simeq 0.60R$ and the sheet cavity is extended along the same trace as in the experiment. The sheet cavitation is transformed into the vortex cavitation, but the vortex cavitation is not extended as much as in the experiment. The underestimation of the vortex cavitation extent seems to be related to the low grid resolution in a distance from the blade surface. The sheet cavity from the computation shows a less radial extent and it starts to be slender earlier than in the experiment. The difference in the sheet cavity extent may be related to the turbulence characteristics.

In Figure 5.11 (bottom), the distribution of α_v on the cross section along the tip vortex cavitation shows that the vortex cavity consisting of the low vapor fraction of $\alpha_v < 0.3$ is slightly detached from the blade surface. Since the cross section is not aligned exactly along the axis of the vortex cavitation, the thickness is on the increase and decrease. The

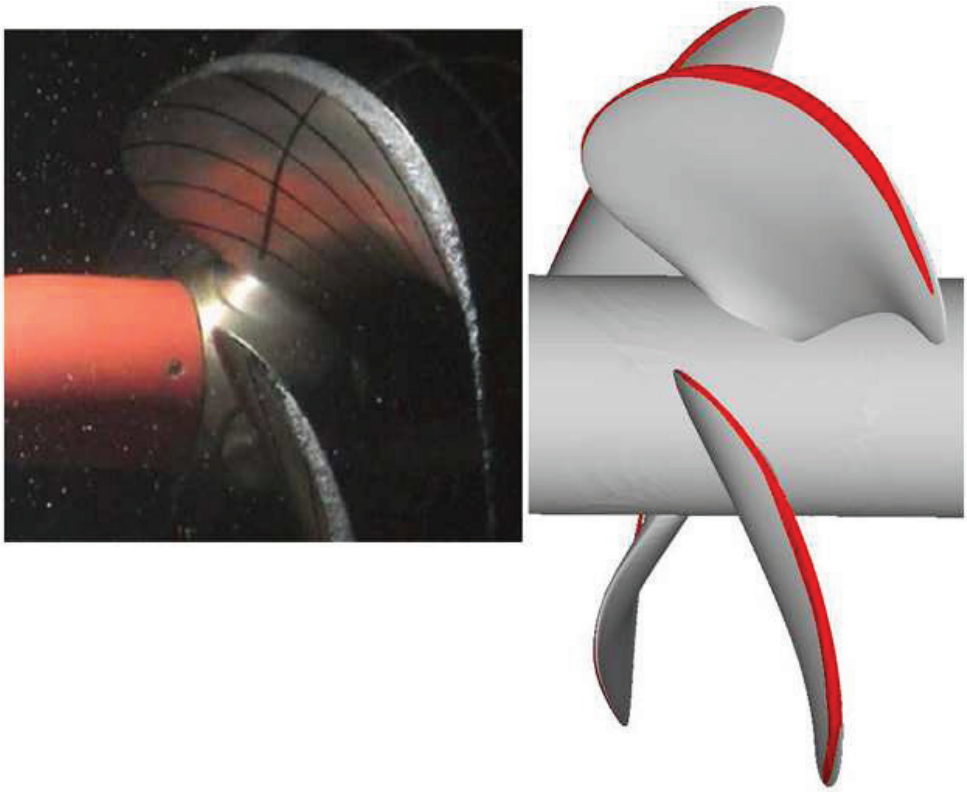

Figure 5.12: Snapshot from the experiment (Lydorf, 2005) (left) and iso-contour of $\alpha_v = 0.1$ from the computation (right) on the highly-skewed propeller for $J = 0.603, \sigma_N = 2.271, N = 30rps$

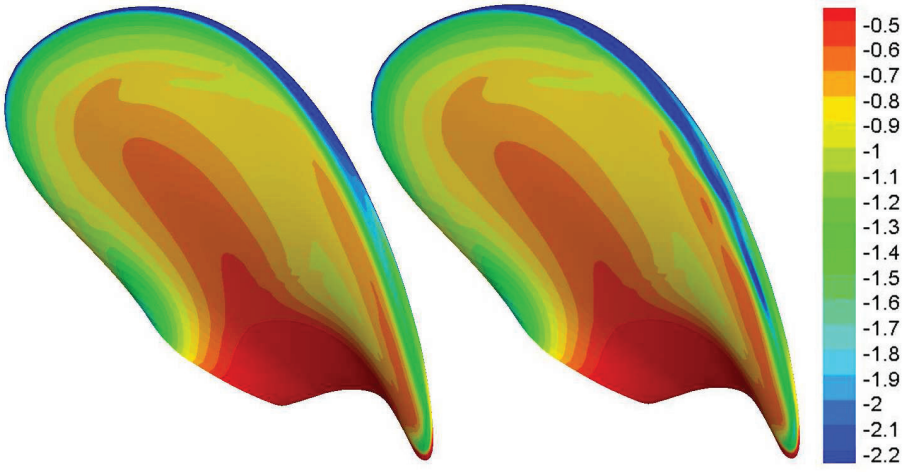

Figure 5.13: C_p on the suction side of the highly-skewed propeller blade in the fully wetted (left) and cavitating (right) flows for $J = 0.603$

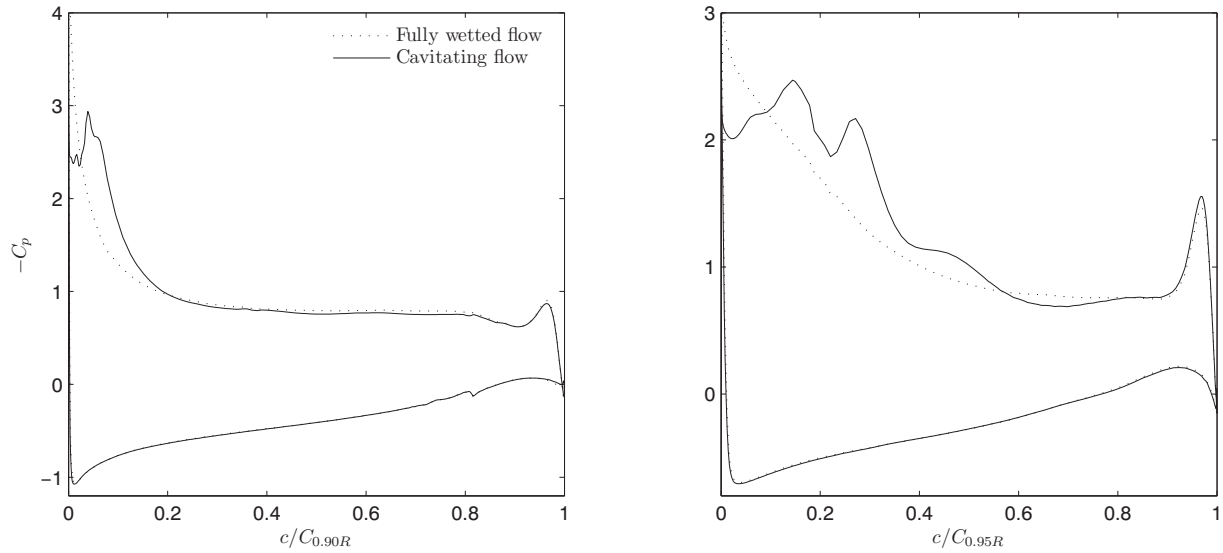

Figure 5.14: C_p on the blade surface of the highly-skewed propeller at $r = 0.90R$ (left) and $0.95R$ (right) for $J = 0.603$

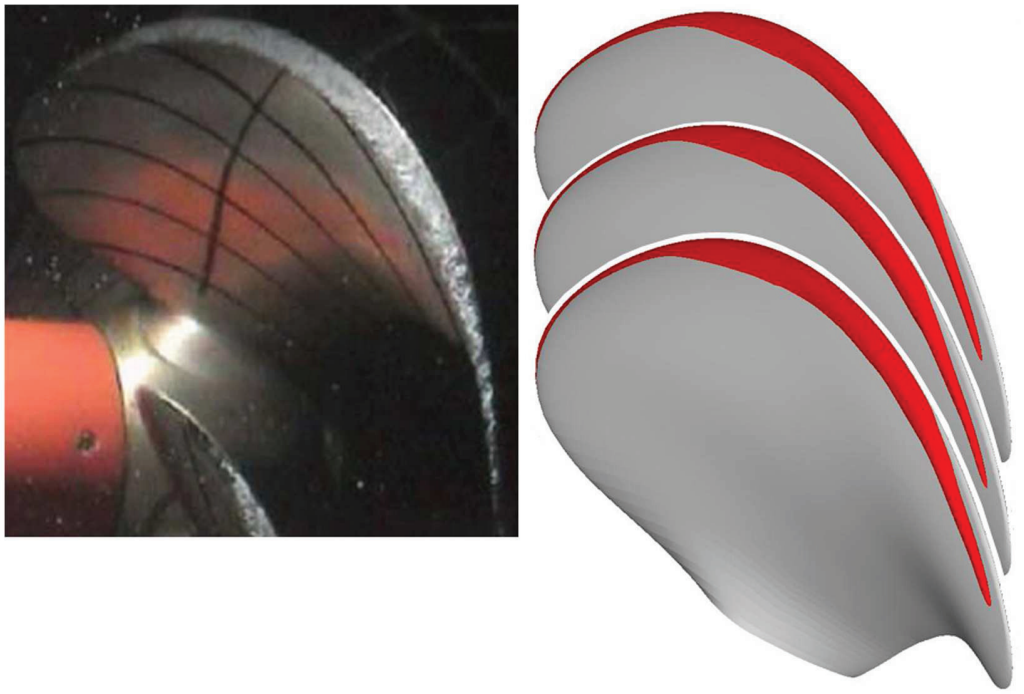

Figure 5.15: Cavity profiles from the experiment (left) and from the computation (right) with $N = 8, 14, 30rps$ (from top to bottom) on the highly-skewed propeller for $J = 0.603, \sigma_N = 2.271$

maximum thickness of the sheet cavity is about $1.5mm$ in Figure 5.11 (top) and less than $1mm$ in Figure 5.11 (bottom).

In Figure 5.13, the pressure distribution on the suction side in the cavitating flow shows a difference in the region under the sheet/vortex cavitation along the blade edge. The low pressure region of $C_p < -1.8$ is more extended along the trailing edge and the radial extent of the low pressure region is slightly increased. The suction pressure varies up and down especially in the region of the sheet cavity detachment and the vortex cavitation.

In Figure 5.14, the chordwise distributions of C_p on the suction side at $r = 0.90R$ and $0.95R$ shows that the suction peak in the fully wetted flow is lowered and the high suction region of $C_p < -1.8$ is extended in the cavitating flow. The pressure in the cavitation region is not constant around the vapor pressure and it fluctuates due to a varying vapor fraction inside the cavity.

It can be seen in Figure 5.15 that the pointed end of the vortex cavitation is more extended and the radial extent of the sheet cavity is slightly larger for a higher rotation rate.

5.3 Actuator disk for wake field modeling

5.3.1 Numerical implementation

Instead of modeling a ship hull, a wake field measured behind a ship model is applied to the propeller inflow to reduce computational cost. The inlet boundary of the computational domain for a propeller is located far upstream to avoid the interaction of inlet boundary condition with propeller flow and the grid near the inlet is rather coarse than near the propeller surface. When the wake field is applied to the inlet boundary, a considerable amount of the wake field can be diffused before reaching close to the propeller and a well-preserved wake field cannot impact on the propeller flow. Therefore, we adopt the momentum source method introduced by Mikkelsen et al. (2007).

An actuator disk of the momentum sources representing local body forces generates a corresponding wake field slightly upstream of the propeller plane. Based on the Rankine-Froude momentum theory, the local loading $\mathbf{F} = (F_r, F_\theta, F_z)$ on the actuator disk for generating the local wake $\mathbf{w} = (w_r, w_\theta, w_z)$ is estimated by

$$F_r = \rho \Delta A (V + w_z) w_r \tag{5.2}$$
$$F_\theta = \rho \Delta A (V + w_z) w_\theta \tag{5.3}$$
$$F_z = 0.5 \rho \Delta A (V^2 - w_z^2) \tag{5.4}$$

where the subscripts r, θ, z denote the radial, tangential, axial directions, respectively, and ΔA is the local area element perpendicular to the axial direction and V is the inflow velocity.

By dividing the local loading $\mathbf{F}$ by the local volume ΔV, the force per volume $\mathbf{f} = (f_r, f_\theta, f_z)$ is found. Each component of $\mathbf{f}$ is distributed to several cells along the direction of that component by the Gaussian distribution. When $\mathbf{f}$ is applied to a cell without distribution, the generated wake field can differ depending on the grid structure and the shock wave can lead to the numerical instability. $\mathbf{f}$ is applied to the momentum conservation equations as a body force. The Cartesian expression (2.2) of the momentum conservation equation is converted to the cylindrical expression including the frame rotation and the body force as follows

$$\begin{aligned}
&\frac{\partial \rho u_r}{\partial t} + \frac{1}{r}\left(\frac{\partial \rho r u_r u_r}{\partial r} + \frac{\partial \rho u_\theta u_r}{\partial \theta} + \frac{\partial \rho r u_z u_r}{\partial z}\right) - \frac{\rho \hat{u}_\theta^2}{r} \\
&\qquad = f_r + \frac{1}{r}\left(\frac{\partial r\tau_{rr}}{\partial r} + \frac{\partial \tau_{\theta r}}{\partial \theta} + \frac{\partial r\tau_{zr}}{\partial z}\right) - \frac{\tau_{\theta\theta}}{r} - \frac{\partial p}{\partial r} \\
&\frac{\partial \rho u_\theta}{\partial t} + \frac{1}{r}\left(\frac{\partial \rho r u_r \hat{u}_\theta}{\partial r} + \frac{\partial \rho u_\theta \hat{u}_\theta}{\partial \theta} + \frac{\partial \rho r u_z \hat{u}_\theta}{\partial z}\right) + \frac{\rho u_r \hat{u}_\theta}{r} \\
&\qquad = f_\theta + \frac{1}{r}\left(\frac{\partial r\tau_{r\theta}}{\partial r} + \frac{\partial \tau_{\theta\theta}}{\partial \theta} + \frac{\partial r\tau_{z\theta}}{\partial z}\right) + \frac{\tau_{r\theta}}{r} - \frac{1}{r}\frac{\partial p}{\partial \theta} \\
&\frac{\partial \rho u_z}{\partial t} + \frac{1}{r}\left(\frac{\partial \rho r u_r u_z}{\partial r} + \frac{\partial \rho u_\theta u_z}{\partial \theta} + \frac{\partial \rho r u_z u_z}{\partial z}\right) \\
&\qquad = f_z + \frac{1}{r}\left(\frac{\partial r\tau_{rz}}{\partial r} + \frac{\partial \tau_{\theta z}}{\partial \theta} + \frac{\partial r\tau_{zz}}{\partial z}\right) - \frac{1}{r}\frac{\partial p}{\partial \theta}
\end{aligned} \tag{5.5}$$

where $\hat{u}_\theta$ is the sum of the frame rotating velocity and the relative tangential velocity u_θ and the stress tensor is

$$\begin{aligned}
\tau_{rr} &= 2(\mu + \mu_t)\left(\frac{\partial u_r}{\partial r}\right), & \tau_{\theta\theta} &= 2(\mu + \mu_t)\left(\frac{1}{r}\frac{\partial u_\theta}{\partial \theta} + \frac{u_r}{r}\right), \\
\tau_{zz} &= 2(\mu + \mu_t)\left(\frac{\partial u_z}{\partial z}\right), & \tau_{r\theta} &= (\mu + \mu_t)\left(\frac{1}{r}\frac{\partial u_r}{\partial \theta} + \frac{\partial u_\theta}{\partial r} - \frac{u_\theta}{r}\right), \\
\tau_{zr} &= (\mu + \mu_t)\left(\frac{\partial u_r}{\partial z} + \frac{\partial u_z}{\partial r}\right), & \tau_{\theta z} &= (\mu + \mu_t)\left(\frac{1}{r}\frac{\partial u_z}{\partial \theta} + \frac{\partial u_\theta}{\partial z}\right)
\end{aligned} \tag{5.6}$$

The cylindrical expression (5.5) is transformed to the curvilinear expression, of which the integral form is solved by the same numerical scheme as explained in Chapter 2.

5.3.2 Wake field modeling

The conventional and highly-skewed propellers are designed for a single-screw tanker and a twin-screw ferry, respectively. The wake distributions on the propeller plane behind those ship models have been measured by MARIN (Kuiper, 2004). The measurements are for the

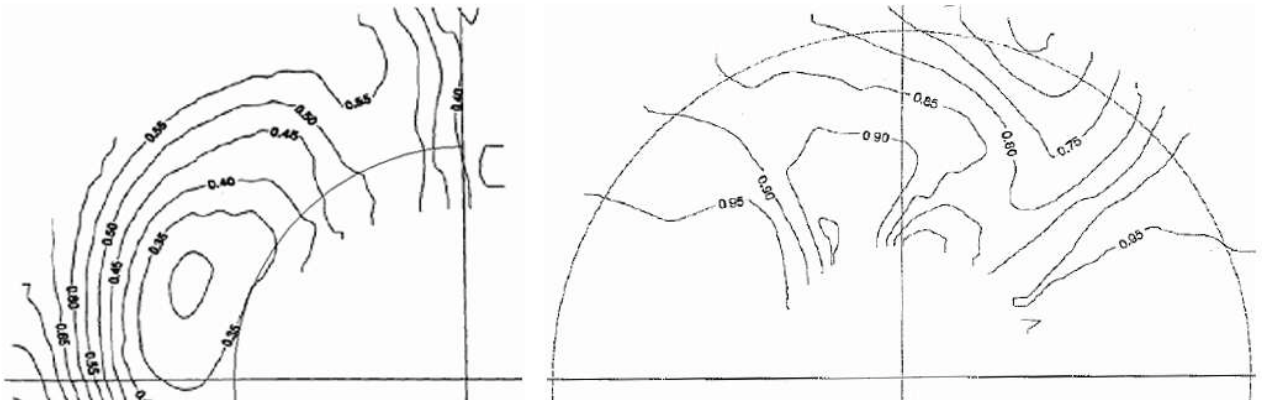

Figure 5.16: u_z/V from the measurements behind the tanker (left) and ferry (right): the circle indicates the propeller tip radius

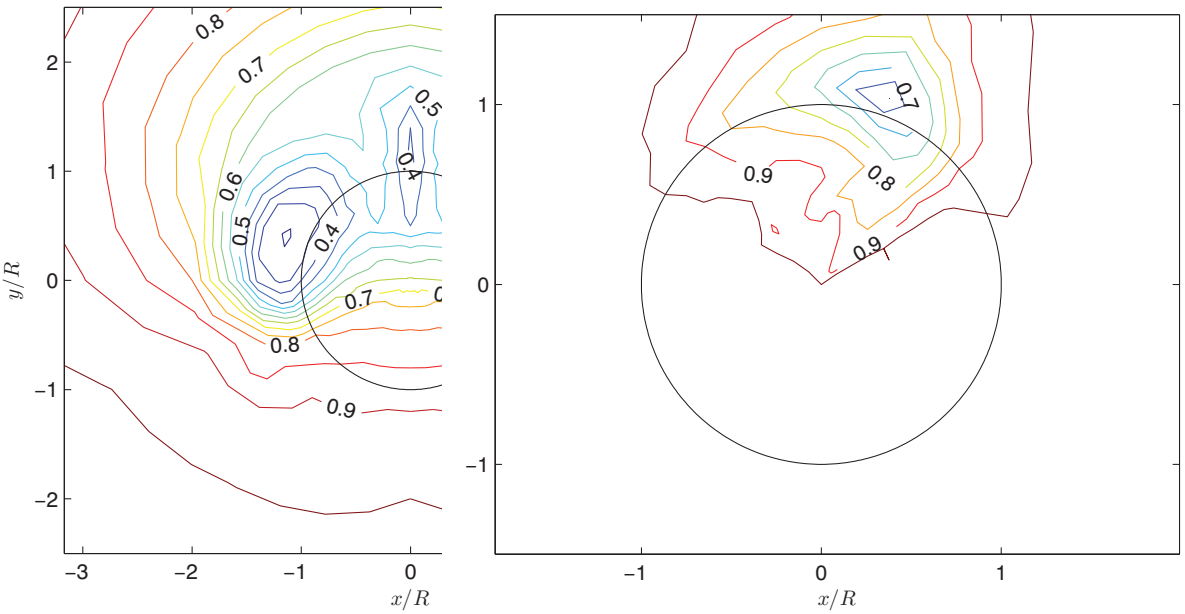

Figure 5.17: u_z/V of the input wake field for the tanker (left) and ferry (right)

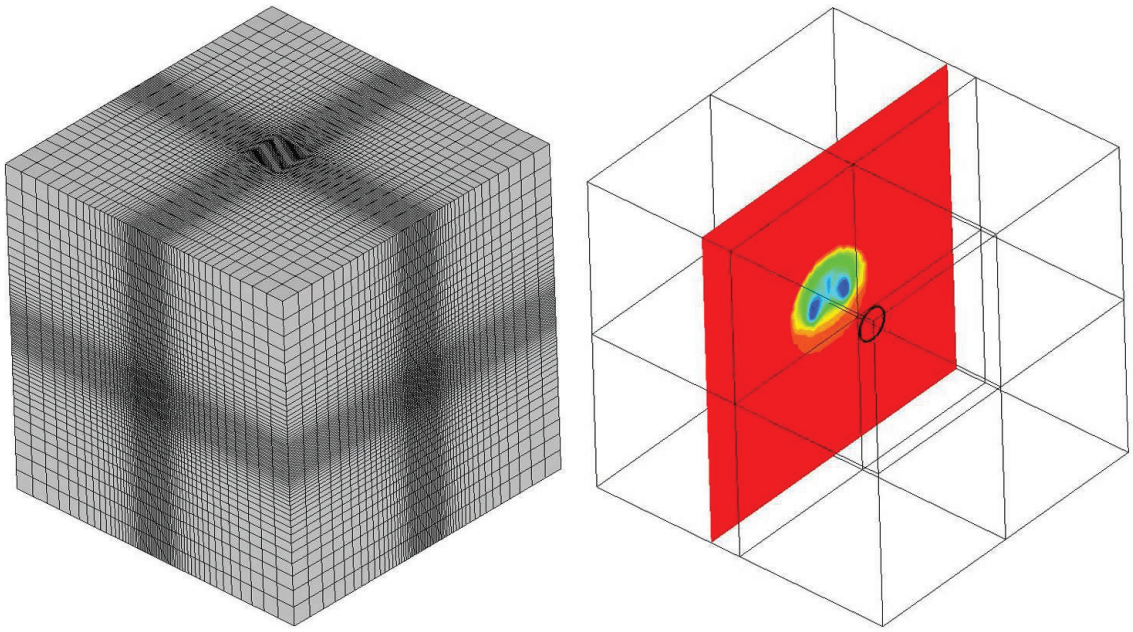

Figure 5.18: Rectangular grid for testing the actuator disk (left) and block structure with a sectional distribution of the axial velocity and a circle indicating the propeller disk area at the location of the actuator disk (right)

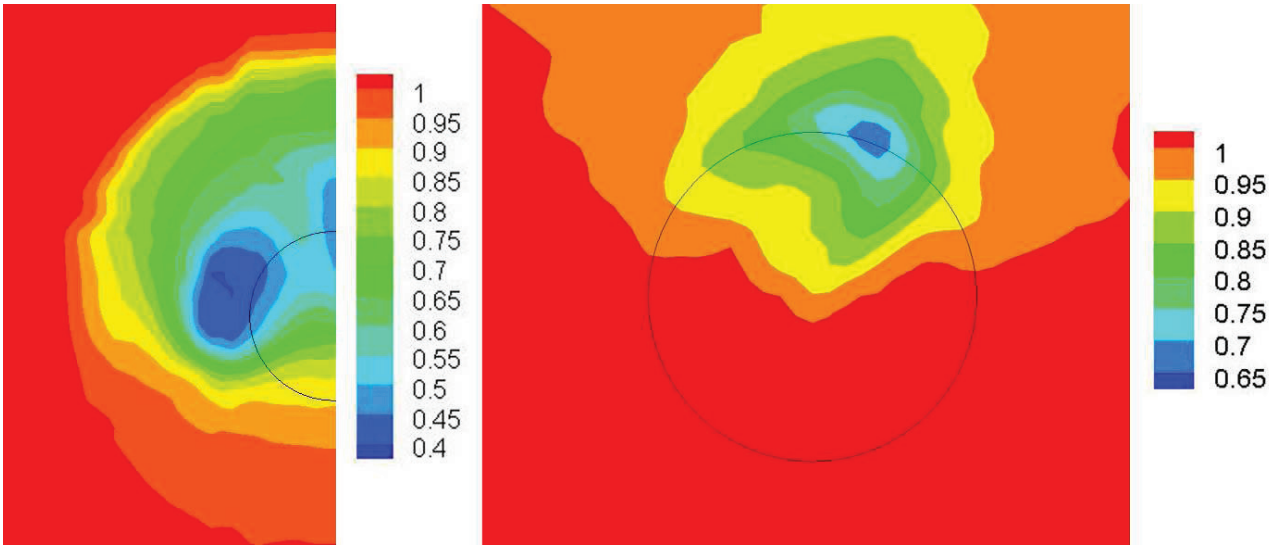

Figure 5.19: u_z/V a diameter downstream from the actuator disk for the tanker (left) and ferry (right)

ship speeds of $V = 1.56m/s$ with the tanker and $2.61m/s$ with the ferry. Although all the components of the wake field can be included in the actuator disk, we consider only the axial component, which is more dominant than the other components.

The normalized axial velocity $(V - w_z)/V$ from the measurement is shown in Figure 5.16. Since it is reported in the experiment that the wake from the tanker has a significant wake peak in the upper part of the propeller plane, the wake field only on the upper part is applied to the actuator disk. The wake from the tanker is almost symmetric and it has a wake peak at the upright angle and in the tip region at $90^o - 130^o$. The wake field from the ferry is on the port side propeller plane and the left side corresponds to the port side. The wake peak is in the tip region at 200^o and the lower part has almost no wake. 0^o indicates the 6 o'clock position.

The input wake field in Figure 5.17 is applied to the points at every 10^o along the tangential direction and almost at every $0.1R$ within $1.5R$ and every $0.5R - 1R$ from $1.5R$ to $5R$ along the radial direction. Since the wake fields in the inner radius for the tanker and outside the propeller disk area for the ferry are not available in the measurements, those parts are made by referring to the wake fields of another tanker and ferry.

Prior to applying the actuator disk to the propeller flow, we test it in the structured rectangular grid only with an axial inflow. The propeller diameter D covers about 24 cells and the computational domain is extended to $5D$, as shown in Figure 5.18. The grid size is gradually increased from the centre to the outer boundary and the actuator disk is located one propeller radius upstream from the centre of the domain. Steady-state computations are made to be converged until the maximum normalized residual drops below 10^{-3}.

In Figure 5.19, the distribution of the normalized axial velocity on the cross section a diameter downstream from the actuator disk shows a fairly good agreement with the input wake field for the actuator disk. While the computed wake level for the ferry is almost identical to the input, the computed wake level within $1.5R$ for the tanker is about $0.1 - 0.2V$ smaller than the input. The wake level can be adjusted with maintaining the overall distribution by scaling.

5.4 Cavitating flows in the behind-hull condition

Conventional propeller

We consider a case for $J_a = 0.4, \sigma_n = 2.2$ on the conventional propeller, where J_a is based on the entrance velocity V_a to the propeller and the axial inflow velocity V is lowered by the behind-hull wake field. The value of J is not reported in the experiment. J corresponding to J_a can be found by integrating the axial wake field on the propeller disk area from the measurements, but the wake field in the computation can differ from the measurements to

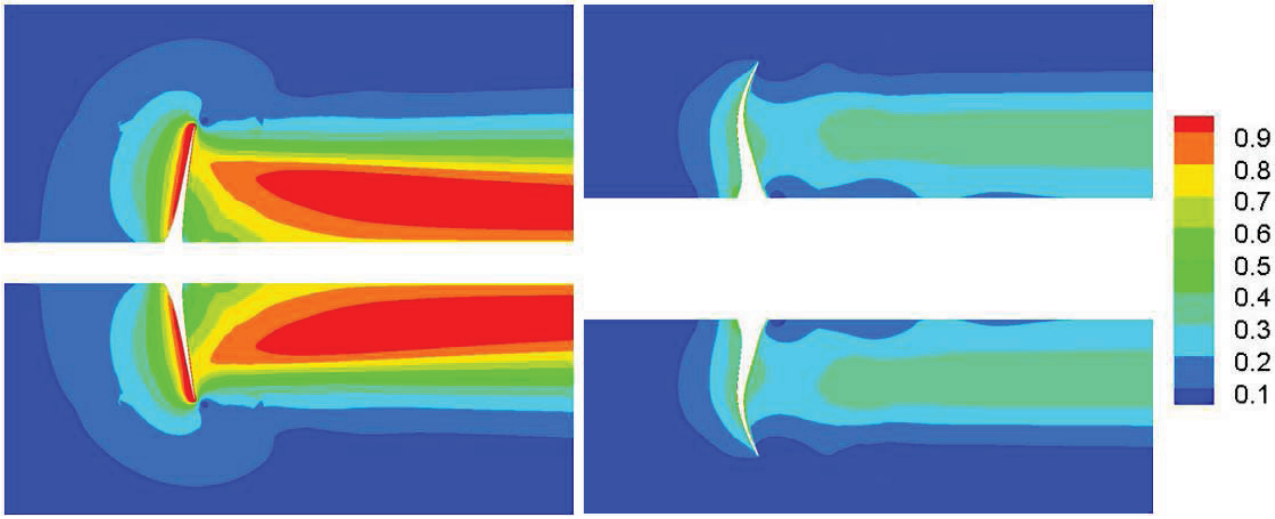

Figure 5.20: Normalized wake magnitude around the conventional propeller for $J = 0.58$ (left) and the highly-skewed propeller for $J = 0.915$ (right)

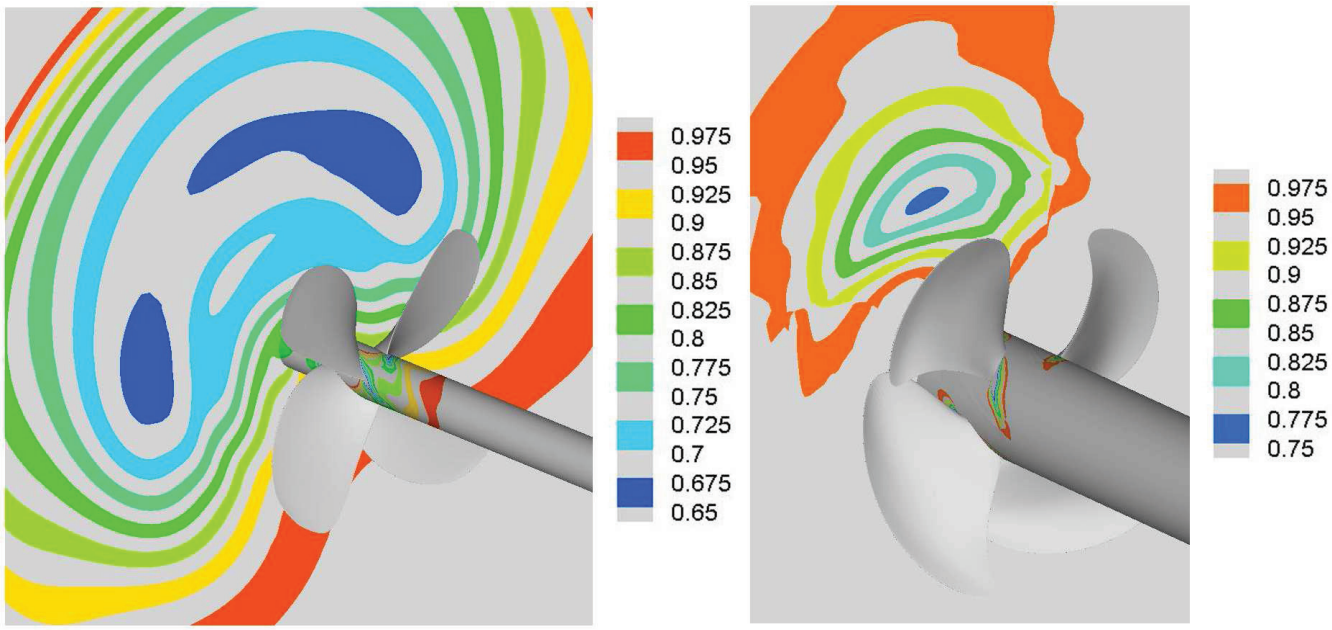

Figure 5.21: Normalized axial velocity component u_z/V at the transverse section $0.5R$ upstream from the propeller plane for the conventional propeller with $J_a = 0.4$ (left) and the highly-skewed propeller with $J = 0.915$ (right)

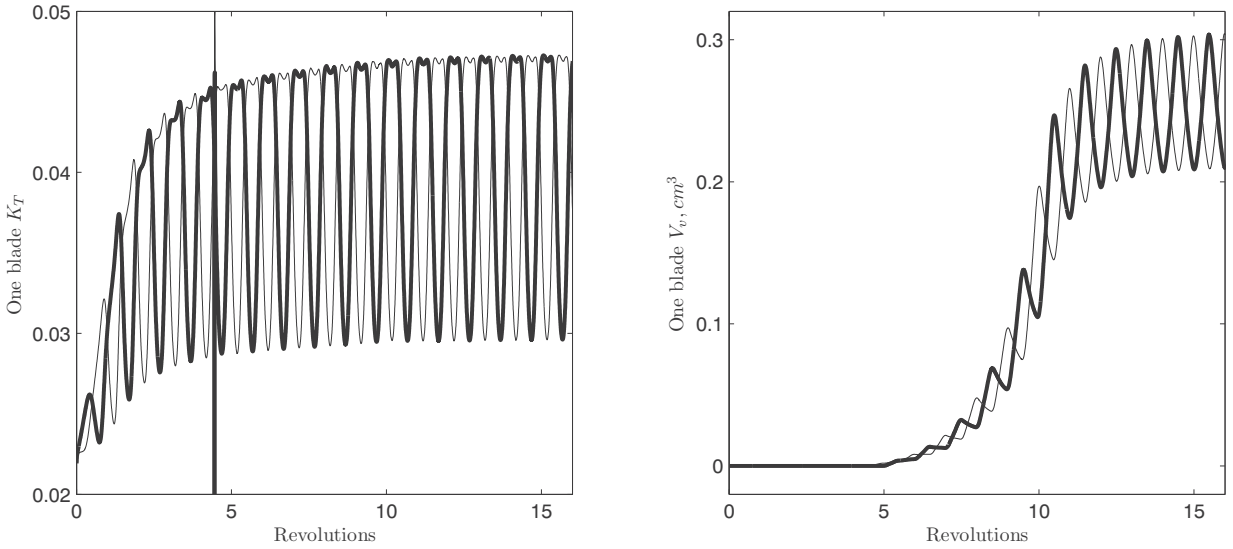

Figure 5.22: K_T (left) and V_v (right) on each of two opposite blades as a function of the revolutions on the conventional propeller for $J_a = 0.4, \sigma_n = 2.2$

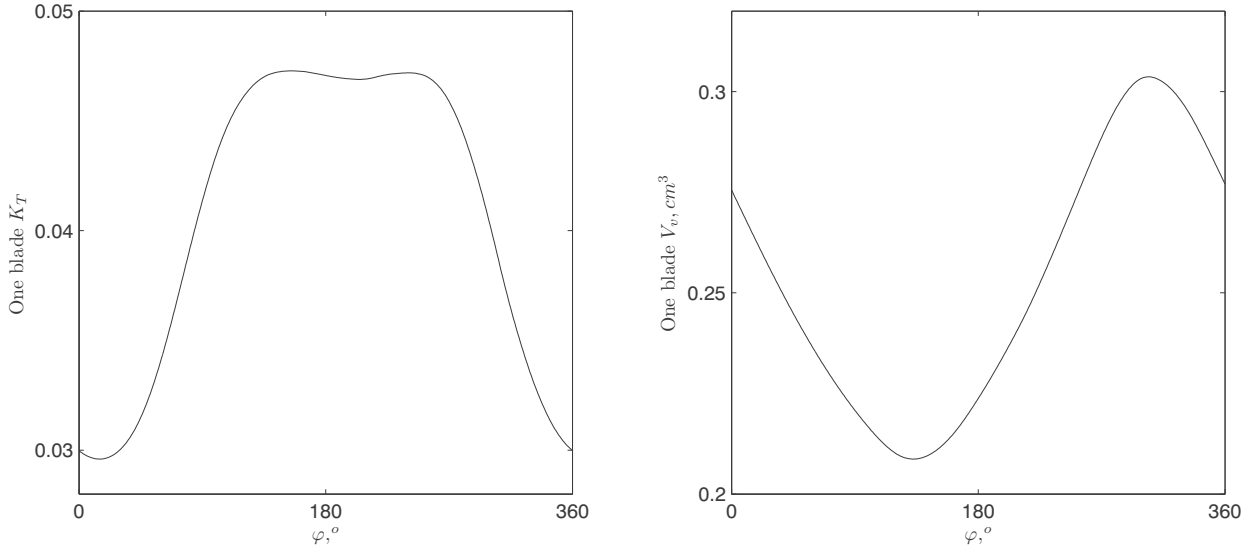

Figure 5.23: K_T (left) and V_v (right) on a blade as a function of the blade angle on the conventional propeller for $J_a = 0.4, \sigma_n = 2.2$

some extent. Therefore, we find J resulting in the same loading condition as $K_T = 0.164$ from the cavitation tunnel test. In the computation with the actuator disk, $J = 0.6$ results in $K_T = 0.162$.

First, we make a steady-state computation without the actuator disk to estimate the extent of the upstream wake from the propeller flow. We include the hydrostatic pressure effects on the cavitation by adding the relative hydrostatic pressure $\rho g z_c$ to the vapor pressure, where z_c is the vertical distance from the propeller centerline to the local point and z_c is positive on a point above the centerline.

In Figure 5.20 (left), the normalized wake magnitude $\sqrt{u_r^2 + u_\theta^2 + (V - u_z)^2}/V$ on the cross section along the axial direction shows that the wake magnitude of $0.1V$ is extended about $1R$ upstream from the propeller plane. We place the actuator disk $1R$ upstream from the propeller plane so that the actuator disk is closely located to the propeller as much as it is outside the propeller flow to reduce the diffusion of the wake field and to avoid numerical conflicts between the propeller flow and the actuator disk.

We start an unsteady-state computation from the converged result of the steady-state computation without the actuator disk. The actuator disk is turned on and the computation continues in a fully wetted flow for four or five rotations so that the wake field spreads over the propeller. Then the cavitation number is gradually decreased to the intended value. The time step is set to $\Delta t = 1/360N$ so that the propeller rotates one degree at each time step.

After the wake field generated by the actuator disk is fully developed over the propeller, the distribution of the axial velocity component on the transverse section between the actuator disk plane and the propeller plane is shown in Figure 5.21. The applied wake field is blurred by the rotating propeller flow. Since the upstream wake from the propeller flow is stronger for the conventional propeller, compared to the highly-skewed propeller, the peak of the applied wake is more reduced. However, the overall distribution of the applied wake is kept to be effective in the propeller flow.

K_T and V_v on each of two opposite blades as a function of the revolutions are shown in Figure 5.22. As the wake flow is developed over the propeller, the variation amplitude of K_T is increased. When the cavitation number starts to be decreased, a pulse from the numerical noise appears in the K_T variation. As σ_n is decreased, both K_T and V_v are slightly increased. After $\sigma_n = 2.2$ is reached, the variation amplitudes in K_T and V_v are converged to 0.018 and $0.095cm^3$, respectively, with a period corresponding to a revolution.

In Figure 5.23, the variations of K_T and V_v in a single cycle show the maximum at the blade angle of $\varphi = 135^o$ and the minimum at $\varphi = 0^o$. The blade angle φ is zero for the generator line on the 6 o'clock position.

In Figure 5.23 (left), the variations of K_T with respect to the blade angle show that K_T is rapidly increased, as the blade enters the wake field at $\varphi = 60^o - 100^o$. The highest value of K_T is kept in the upper part of $\varphi = 155^o - 240^o$. K_T is rapidly decreased, as the blade exits the wake field at $\varphi = 280^o - 320^o$. The variation curve of K_T is almost symmetric around

$\varphi = 200^o$, because the blade angle φ is zero for the generator line on the 6 o'clock position and the generator line is about 20^o ahead of the mid-chord locus.

In Figure 5.23 (right), the increase of V_v appears later than that of K_T and the changing rate is rather constant. V_v becomes maximum at $\varphi = 305^o$ and minimum at $\varphi = 135^o$, which appear $100^o - 120^o$ after the highest and lowest points of K_T. It can imply that it takes a certain time for a cavity to be formed.

In Figure 5.24 and 5.25, the computed cavitation profile is compared with the snapshot from the experiment. In the experiment, the cavitation appears at $\varphi = 150^o - 180^o$ and disappears at $\varphi = 280^o - 330^o$. In the computation, the cavity extent is changing, but the cavitation exists continuously around the whole revolution.

In the experiment, the sheet cavitation starts from the leading edge of $r = 0.75R$ at $\varphi = 180^o$. As it goes to the outer radius, the chordwise extent of the sheet cavity is increased and the sheet cavitation at the blade tip is transformed to the tip vortex cavitation. At $\varphi = 240^o$, the sheet cavitation almost vanishes and the vortex cavitation is more extended and the bursting of the vortex cavitation occurs. At $\varphi = 270^o$, the vortex cavitation is slightly shortened without bursting.

In the computation, the sheet cavitation has a similar starting point, but the chordwise extent is less at $\varphi = 180^o$, compared to the experimental result. At $\varphi = 240^o$, the sheet cavity size is even slightly increased in contrast to almost no sheet cavitation in the experiment. The tip vortex cavity is formed, but the extent is quite short and it does not vary significantly at different blade angles.

The considerable difference from the experiment except for $\varphi = 180^o$ seems to be mainly due to the difference of the applied wake field. The cavitation test for the conventional propeller with the ship model has not been done within the EU Project Leading Edge. Only limited information for the test of the wake-field measurement is available and the consistence of the ship model in the wake-field measurement and the cavitation test is in question.

The distribution of C_p on the suction side of the blade in Figure 5.26 (right) shows that high suction pressure of $C_p < -2.0$ appears along the leading edge of the outer radii and the blade tip at $\varphi = 180^o$. At $\varphi = 270^o$, the high suction region is slightly more extended along the leading edge and the tip. While no high suction pressure appears at $\varphi = 0^o$ and 90^o, the sheet cavity of a similar size to that at $\varphi = 180^o$ still exists. It implies that the sheet cavity formed at the upper part of the propeller plan does not vanish at the lower part around $\varphi = 0^o$. It is difficult to conclude that no complete desinence of the cavity in the computation is simply due to the underestimation of the condensing rate, because the overall pressure distribution, induced by the applied wake field in the computation, can differ from that in the experiment.

$-C_p$ at $r = 0.8R$ and $0.9R$ in Figure 5.27 shows high suction and pressure at the leading edge except for $\varphi = 0^o$, because the incident angle is increased due to the decelerated axial velocity in the wake field at $\varphi = 90^o - 270^o$. As the blade enters the higher wake field at

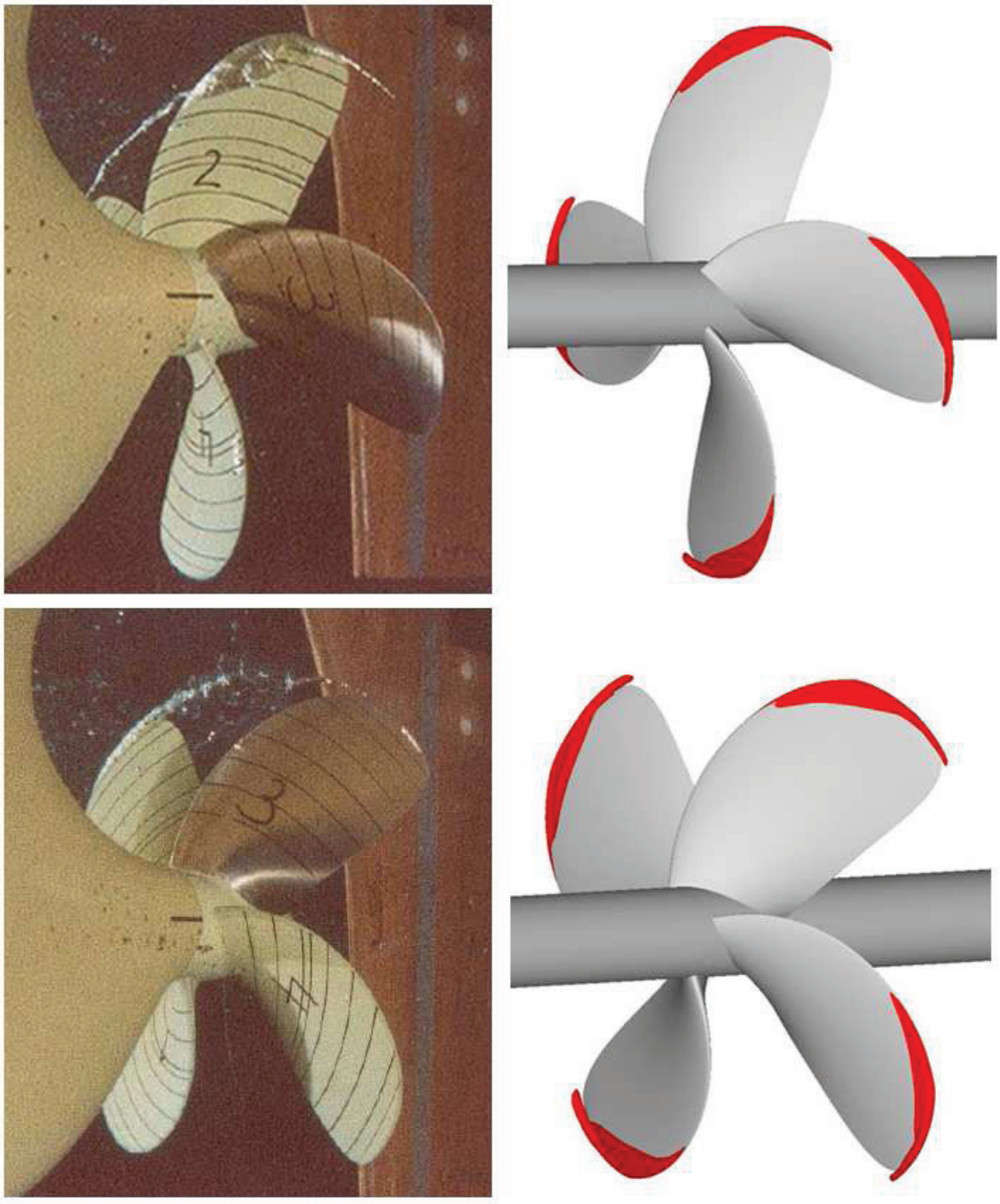

Figure 5.24: Snapshots from the experiment (left column) and iso-contours of $\alpha_v = 0.1$ from the computation (right column) at $\varphi = 180^o$ (top) and 240^o (bottom) on the conventional propeller for $J_a = 0.4, \sigma_n = 2.2$

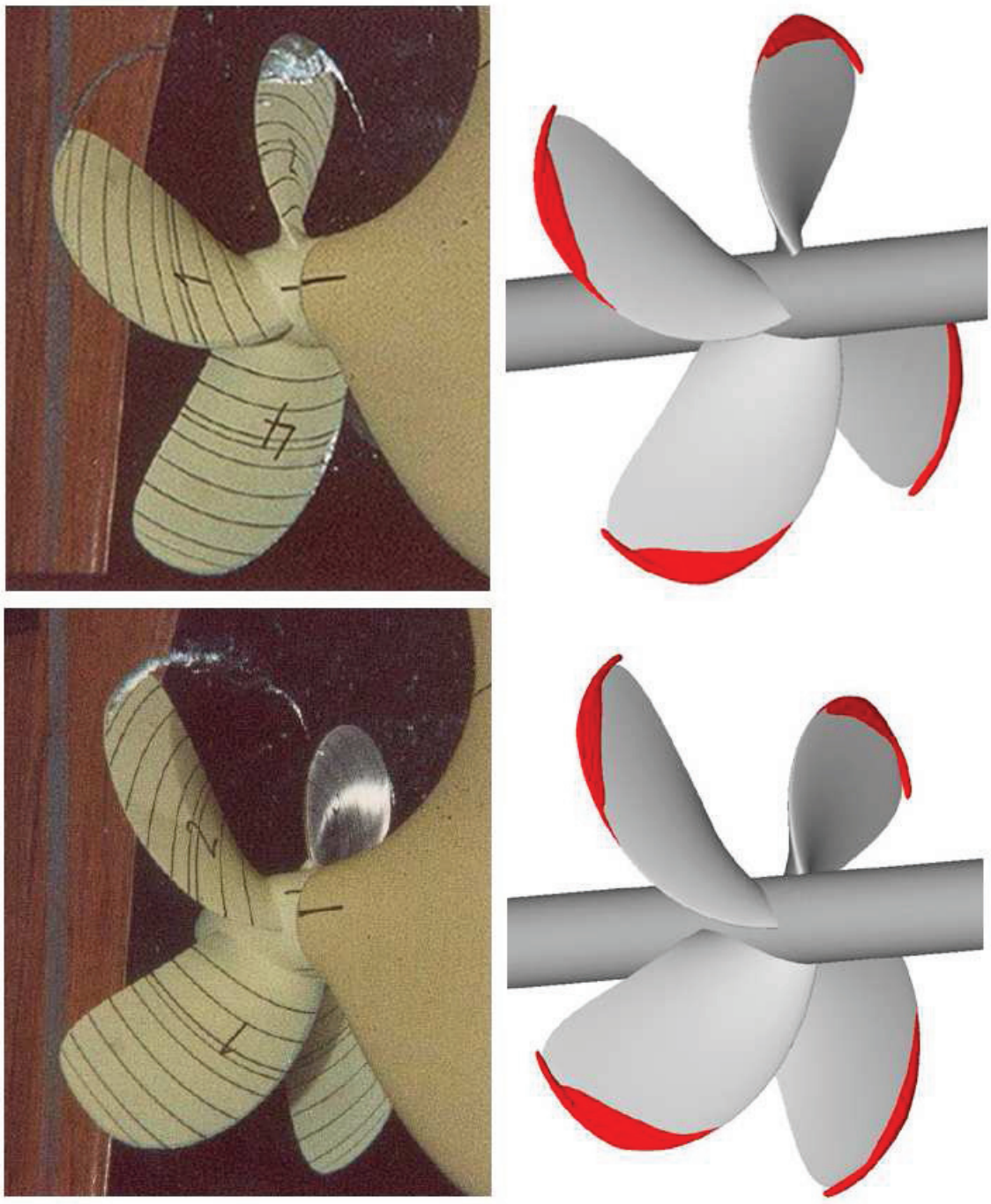

Figure 5.25: Snapshots from the experiment (left column) and iso-contours of $\alpha_v = 0.1$ from the computation (right column) at $\varphi = 180^o$ (top) and 240^o (bottom) on the conventional propeller for $J_a = 0.4, \sigma_n = 2.2$

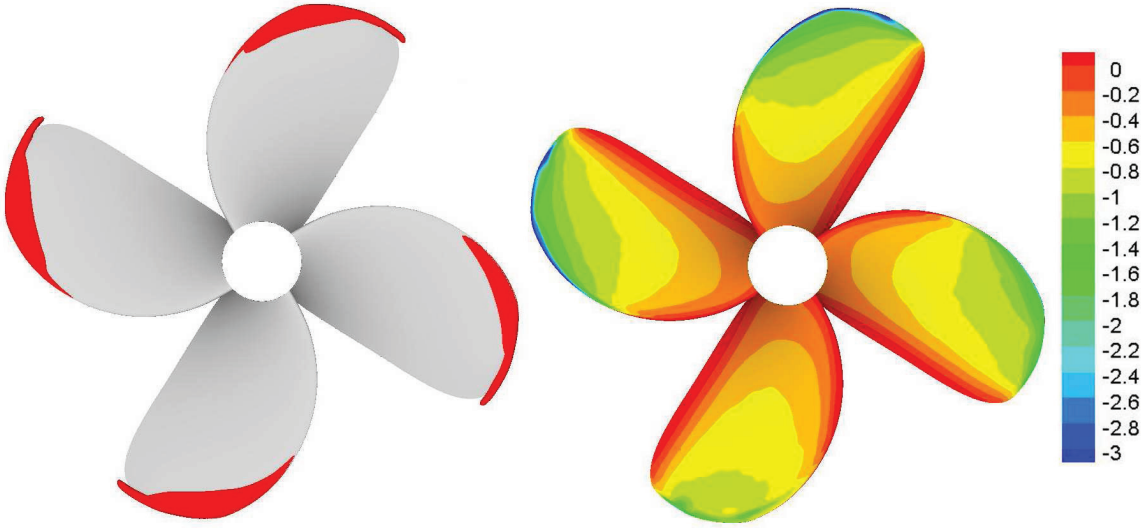

Figure 5.26: Computed cavity profile (left) and C_p (right) on the suction side of the conventional propeller blade for $J_a = 0.4, \sigma_n = 2.2$

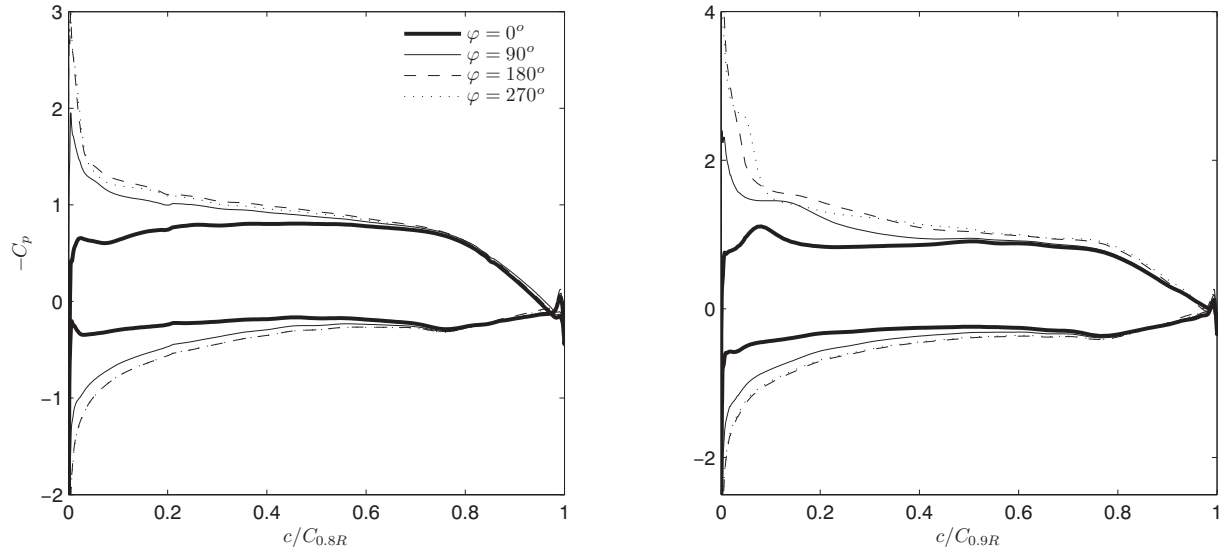

Figure 5.27: C_p on the blade surface of the conventional propeller in different blade angles at $r = 0.8R$ (left) and $0.9R$ (right) for $J_a = 0.4, \sigma_n = 2.2$

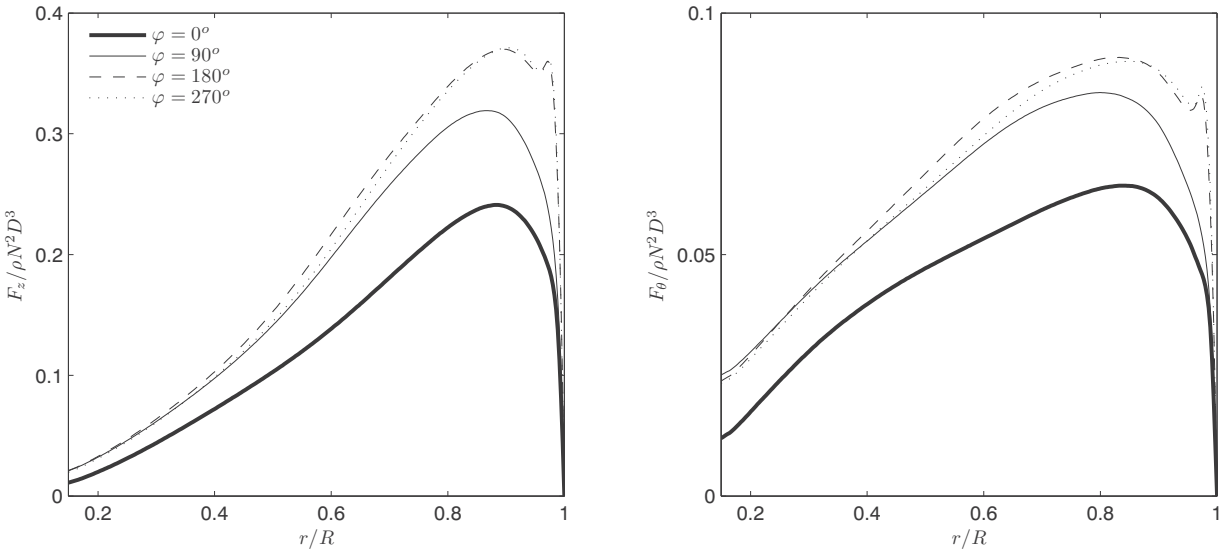

Figure 5.28: Axial (left) and tangential (right) loadings as functions of the radial distance on the conventional propeller for $J_a = 0.4, \sigma_n = 2.2$

$\varphi = 180^o$ and 270^o, the suction/pressure peaks become even higher than $\varphi = 180^o$. Those peaks at $r = 0.9R$ are more pronounced, compared to those at $r = 0.8R$.

$-C_p$ on the suction side at $r = 0.9R$ shows a bump around $c/C_{0.9R} = 0.08$ at $\varphi = 0^o$ and a constant pressure of $C_p = -1.45$ around $c/C_{0.9R} = 0.1$ at $\varphi = 90^o$. Although the overall pressure on the suction side is above the vapor pressure at $\varphi = 0^o$ and 90^o, the pressure at the leading edge seems to be altered by the existing cavity. While the suction pressure at $r = 0.9R$ is smoothly lowered from the peak at $\varphi = 180^o$, $C_p = -2.6$ in the down-slope is slightly extended at $\varphi = 270^o$. As the leading edge continues to be under the high suction from $\varphi = 180^o$ to 270^o, the vapor fraction in the cavity is increased and the pressure inside the cavity gets closer to the vapor pressure. However, the pressure inside the cavity is not lowered to $C_p = -\sigma_N$ at $\varphi = 270^o$, because the vapor fraction in the cavity does not become sufficiently high.

The axial and tangential loadings in Figure 5.28 show that the maximum is at $r \simeq 0.9R$ for the axial loading and $r \simeq 0.85R$ for the tangential loading. F_z, F_θ are the force per unit length from the integration along the chord. The magnitude level over the entire blade varies with respect to the blade angle. Both loadings are increased, as the blade enters the wake field at $\varphi = 90^o$. The highest loadings are maintained at $\varphi = 180^o$ and 270^o inside the wake field and are lowered at $\varphi = 0^o$ outside the wake field.

The overall distributions of both loadings do not differ significantly at different blade angles, but an irregular increase appears near the blade tip at $\varphi = 180^o$ and 270^o, which is related to the tip vortex boosting the suction pressure.

Highly-skewed propeller

We consider a case for $J = 0.915, \sigma_n = 1.49$ on the highly-skewed propeller. The cavitation test for the highly-skewed propeller in the behind-hull condition has been conducted in the largest cavitation tunnel of the HSVA, which is $11m$ long, $2.8m$ wide and $1.6m$ high and allows the installation of the ship model (Johannsen, 2004). The loading condition in the cavitation tunnel corresponds to $K_T = 0.176$ in the propulsion test. The value of J corresponding to $K_T = 0.176$ is found from the propulsion test result (Mrugowski, 2003). The same rotation rate of $N = 30rps$ as in the cavitation tunnel test is applied to the computation.

The upstream wake from the highly-skewed propeller without the actuator disk is less extended than that from the conventional propeller, as shown in Figure 5.20. The actuator disk is placed $1R$ upstream from the propeller plane.

The variations of K_T and V_v on each blade in Figure 5.29 have regular periodicity with amplitudes of 0.026 and $0.027cm^3$, respectively. The average of K_T on all four blades is $K_T = 0.183$, which is 4% larger than that from the propulsion test. In the open-water condition, the discrepancy in K_T is $15 - 21\%$ for $J = 0.81 - 0.93$. The discrepancy in the behind-hull condition seems to be coincidentally canceled out due to the difference in the wake field.

In Figure 5.30, the variations in a single cycle with respect to the blade angle show that both K_T and V_v are increased, when the blade is in the upper region. As the blade enters the wake region, K_T is increased. While the peak in the applied wake field is at $\varphi = 200^o$, the highest point of K_T is at $\varphi = 190^o$, because the inflow is convected with the propeller rotation. V_v is rapidly increased at $\varphi = 180^o - 220^o$ and the maximum of V_v is at $\varphi = 245^o$. The maximum of V_v appears later than the peak of K_T, which can imply that the cavity takes time to be formed, as mentioned above. V_v is rather slowly decreased from the maximum. V_v is not decreased to zero, because the root cavitation exists around the whole revolution.

In Figure 5.31, the computed cavity profile is compared with the snapshot from the experiment. At $\varphi = 180^o$, the sheet cavity starts from the leading edge of $r \simeq 0.95R$ and it is extended along the tip and converted to the tip vortex cavitation in the experiment. In the computation, the cavity starts from the leading edge of $r \simeq 0.80R$ and the cavity extent along the tip is shorter and the vortex cavitation does not appear. The radial extent of the cavity from the computation is also shorter than that from the experiment. While the cavity interface in the experiment has a rough pattern as in the sheet cavitation with a high incident angle, the computed cavity has a smooth interface.

At $\varphi = 210^o$, the computed cavity starts at almost the same radial position as at $\varphi = 180^o$ and the radial and chordwise extents are slightly larger than at $\varphi = 180^o$. However, the extent of the computed cavity is still shorter than that from the experiment. While the tip vortex cavitation from the experiment is more extended at $\varphi = 210^o$, the computation still reproduces no vortex cavitation. The cavitation starting point in the fore part, the

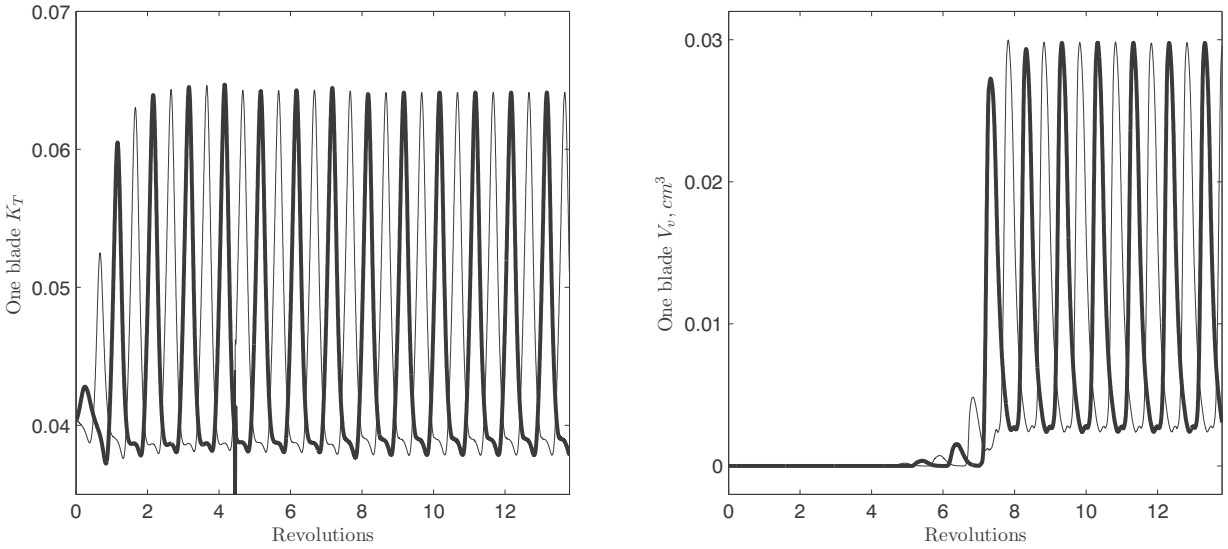

Figure 5.29: K_T (left) and V_v (right) on each of two opposite blades as a function of the revolutions on the highly-skewed propeller for $J = 0.915, \sigma_n = 1.49$

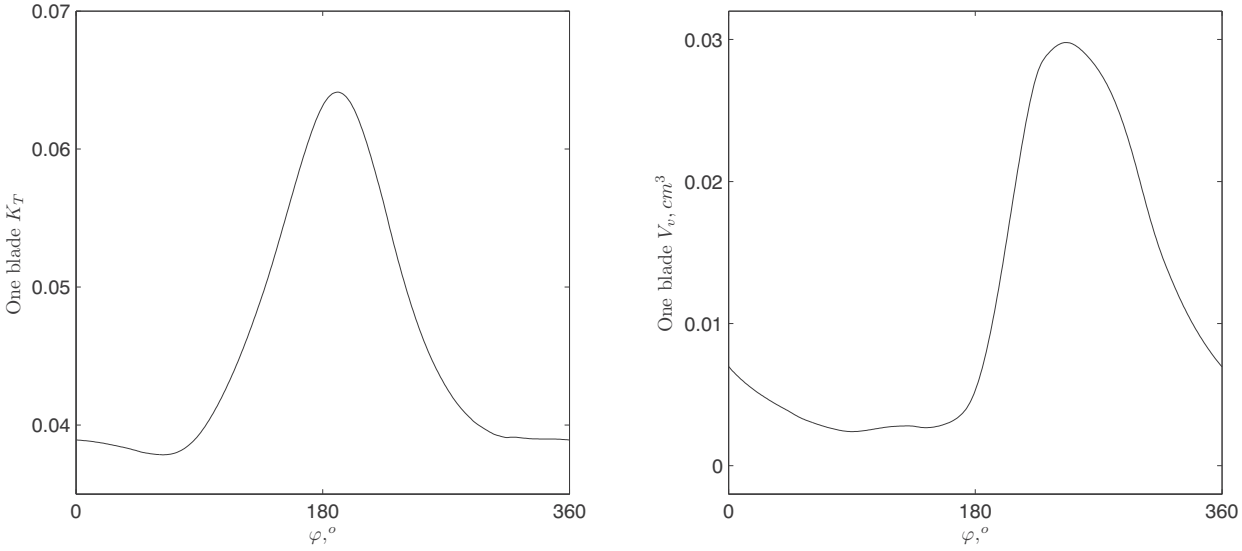

Figure 5.30: K_T (left) and V_v (right) on a blade as a function of the blade angle on the highly-skewed propeller for $J = 0.915, \sigma_n = 1.49$

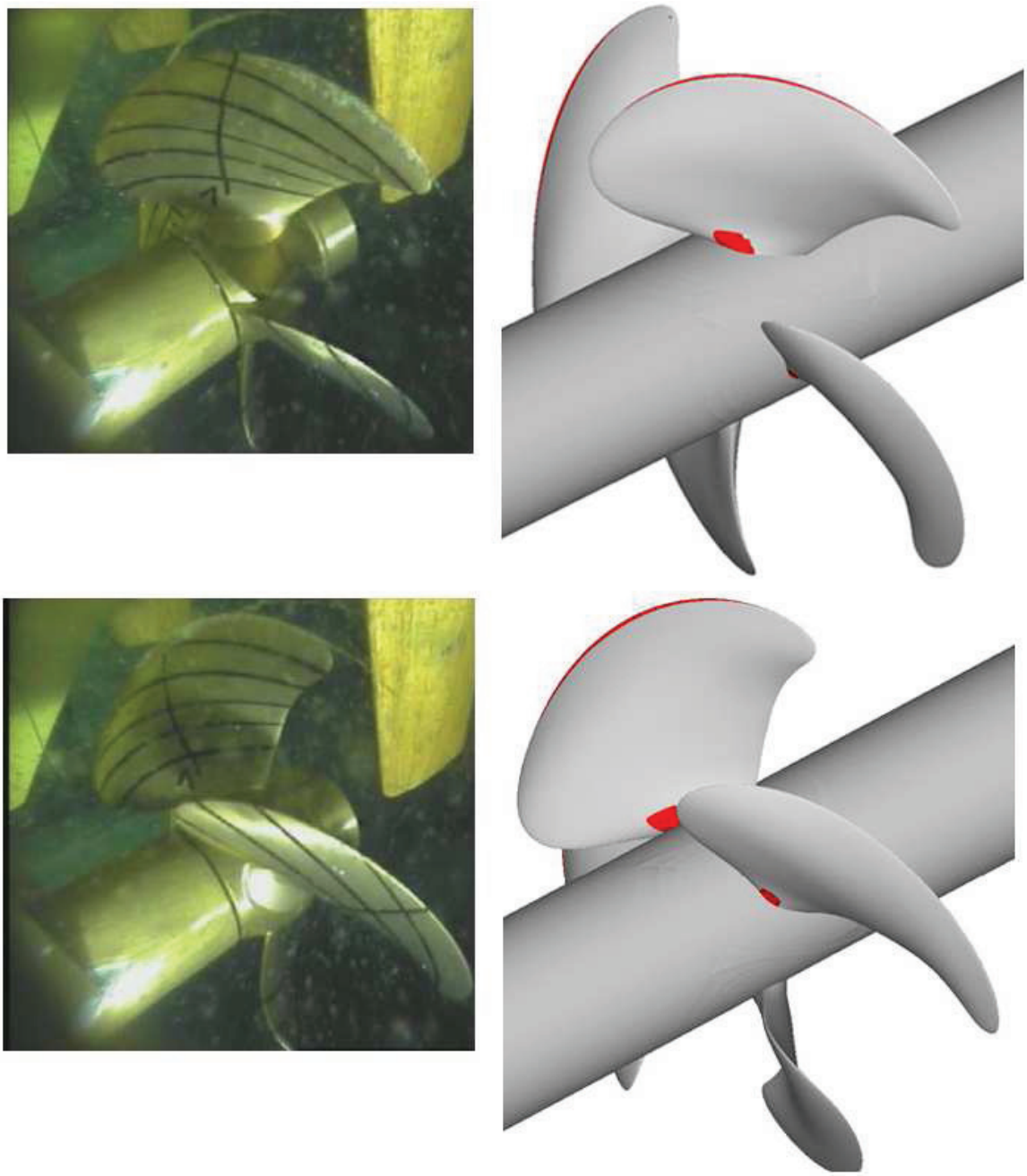

Figure 5.31: Snapshots from the experiment (Johannsen, 2004) (left column) and iso-contours of $\alpha_v = 0.1$ from the computation (right column) at $\varphi = 180^o$ (top) and 210^o (bottom) on the highly-skewed propeller for $J = 0.915, \sigma_n = 1.49$

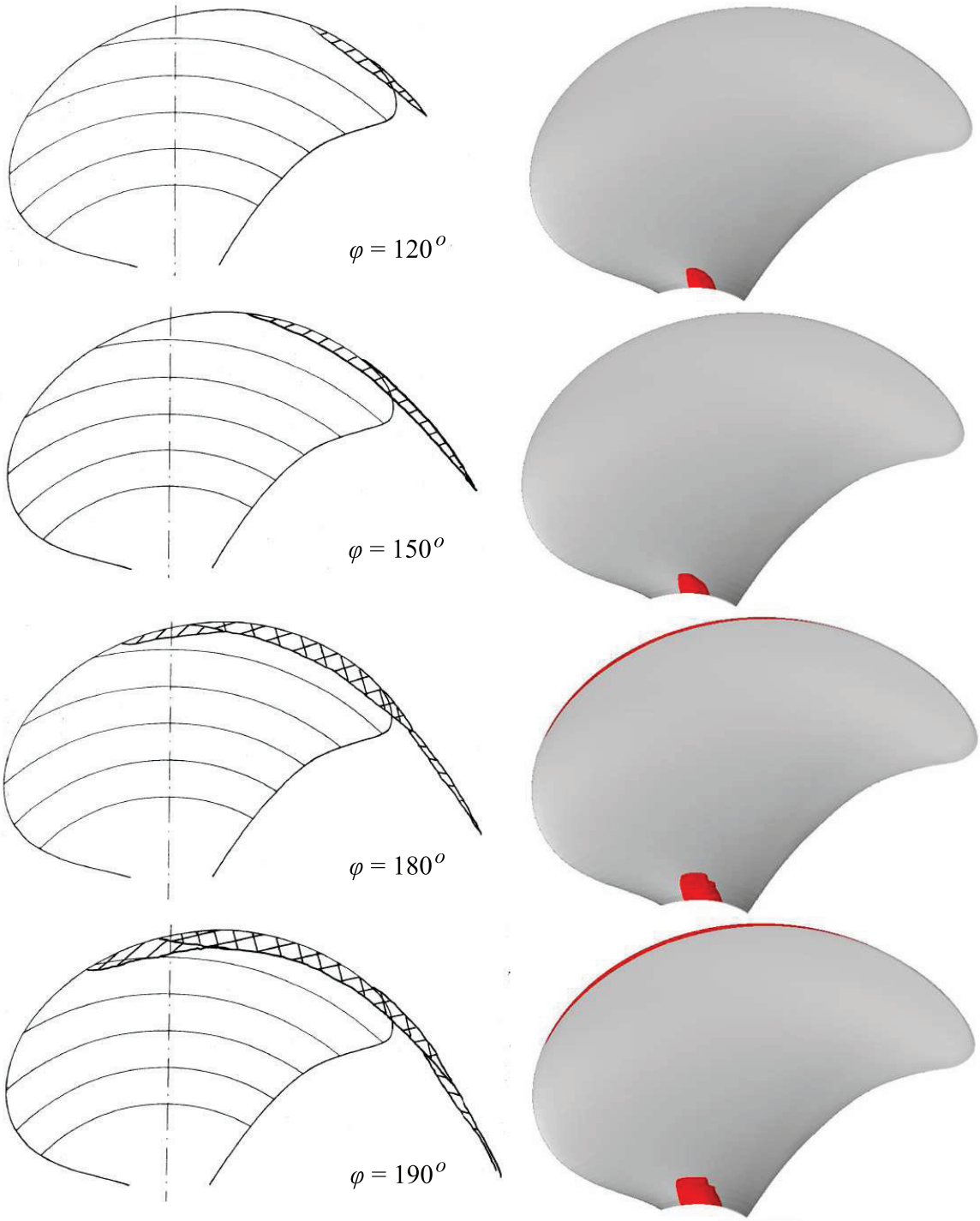

Figure 5.32: Sketches of the cavity profile from the experiment (Johannsen, 2004) (left) and iso-contours of $\alpha_v = 0.1$ from the computation (right) on the suction side of the highly-skewed propeller for $J = 0.915, \sigma_n = 1.49$

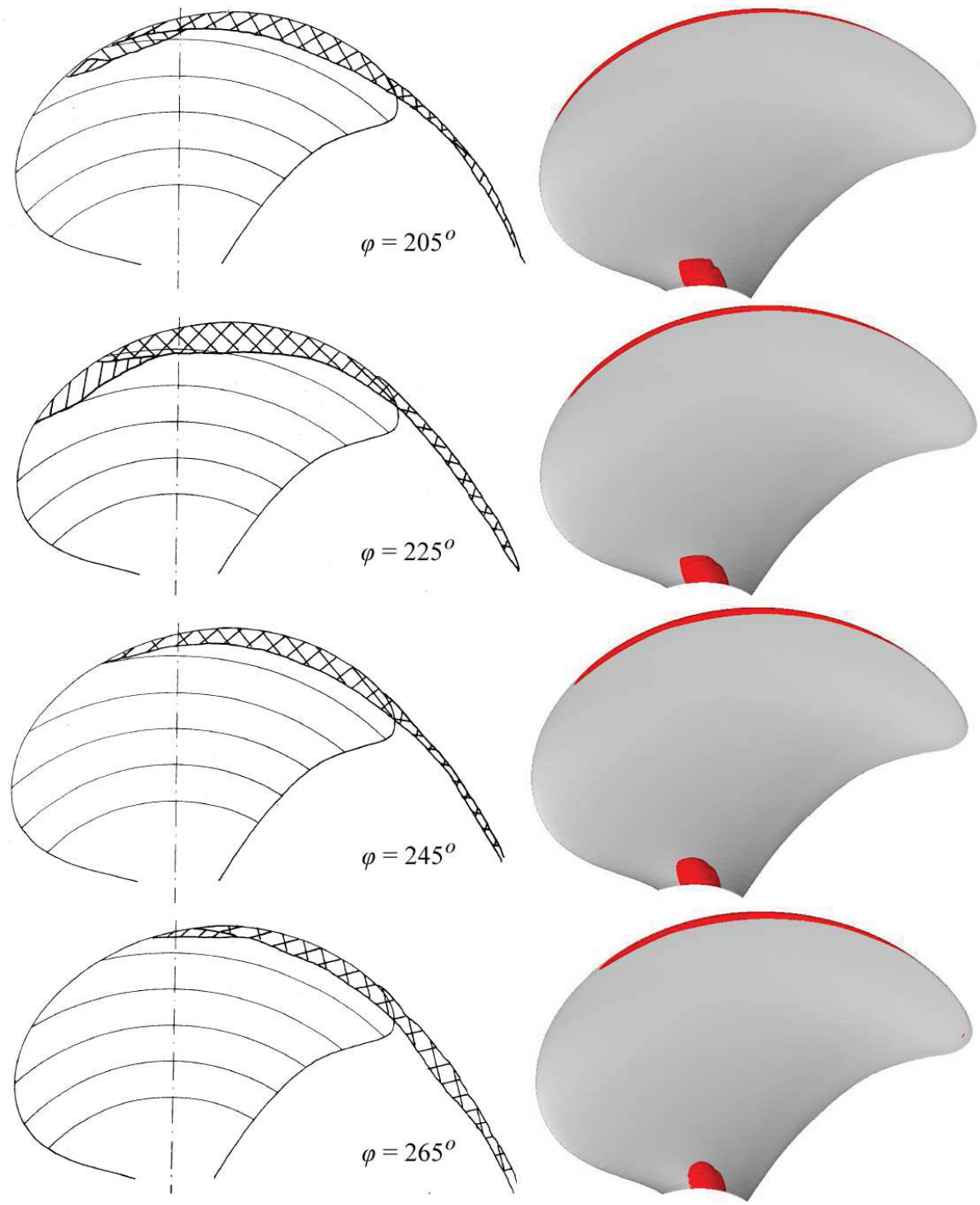

Figure 5.33: Sketches of the cavity profile from the experiment (Johannsen, 2004) (left) and iso-contours of $\alpha_v = 0.1$ from the computation (right) on the suction side of the highly-skewed propeller for $J = 0.915, \sigma_n = 1.49$

underestimation of the cavity extent and no vortex cavitation in the computation seem to be caused by the differences in the behind-hull wake field and the turbulent characteristics.

In Figure 5.32 and 5.33, the variation of the cavity profile from the experiment with respect to the blade angle is compared with that from the computation. In the sketches of the experimental result, the area marked with diagonal lines indicates unstable and fluctuating cavitation and the one with double diagonal lines indicates stable cavitation. The computational result shows no fluctuating cavitation with a higher frequency than the propeller rotation rate.

In the experiment, the unstable cavitation appears at $\varphi = 120^o - 150^o$ and some part of the cavity becomes stable at $\varphi = 150^o - 180^o$. In the computation, the stable cavitation appears from $\varphi = 165^o$. While the starting point of the stable cavitation moves forward and the radial extent is increased from $\varphi = 180^o$ to 225^o in the experiment, the starting point does not move significantly and the radial and chordwise extent of the sheet cavity is increased in the computation. The cavitation starting point moves backward and the radial extent is decreased from $\varphi = 225^o$ to 265^o in the experiment. The starting point of the computed cavity also moves backward, but the radial extent is increased. The radial extent of the computed cavity is decreased from $\varphi = 265^o$ and it vanishes at $\varphi \simeq 340^o$. It is reported in the experiment that the cavity vanishes at $\varphi = 330^o$.

The computed cavity distribution has some difference from the experimental result and the tip vortex cavitation is not reproduced in the computation, but the variation patterns with respect to the blade angle have similarity.

In the experiment, the tip vortex cavitation appears at $\varphi = 90^o$ and disappears at $\varphi = 330^o$. The unstable and intermittent sheet cavitation appears at $\varphi = 120^o$ and the sheet cavitation becomes stable at $\varphi = 150^o - 180^o$. The sheet cavitation vanishes at $\varphi = 270^o - 330^o$.

While the intermittent root cavitation on the suction side is reported on the region of the maximum blade thickness around $\varphi = 180^o$ in the experiment, the root cavitation on the suction side exists around the whole revolution in the computation and it starts from the maximum thickness region and the extent is the maximum at $\varphi = 190^o - 200^o$. The difference in the root cavitation is probably due to the blade mount on the hub, which is not included in the computational model.

Figure 5.34 shows that the low pressure of $C_p < -1.2$ at $\varphi = 180^o$ appears in the blade tip region of the suction side, which corresponds to the area covered by the sheet cavitation. While the sheet cavity is more extended along the chordwise and radial directions at $\varphi = 270^o$, the pressure at the blade tip is increased to $C_p > -1.0$ except for the trailing edge in the outer radii of $0.9R \leq r \leq 0.95R$. It implies that it takes a time corresponding to about 1/4 revolution that the cavitation is fully developed. At $\varphi = 0^o$ and 90^o, the pressure in the tip region is higher than that in the inner radii.

In Figure 5.35, the pressure distribution on the suction side does not differ significantly at $\varphi = 0^o$ and 90^o. The distribution of C_p at $\varphi = 0^o$ and 90^o shows almost no effect of incident

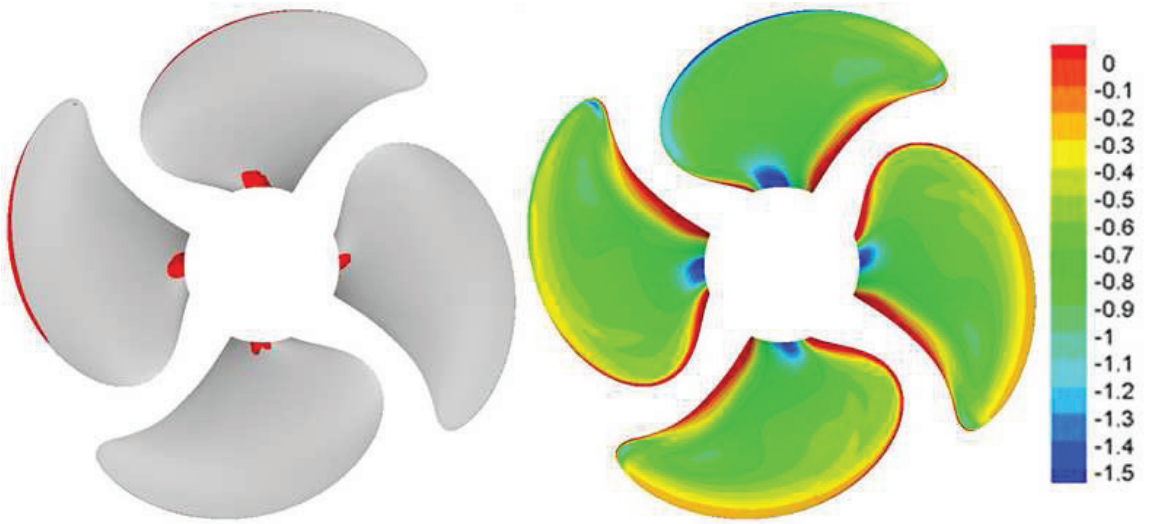

Figure 5.34: Cavitation profile (left) and C_p (right) on the suction side of the highly-skewed propeller blade for $J = 0.915, \sigma_n = 1.49$

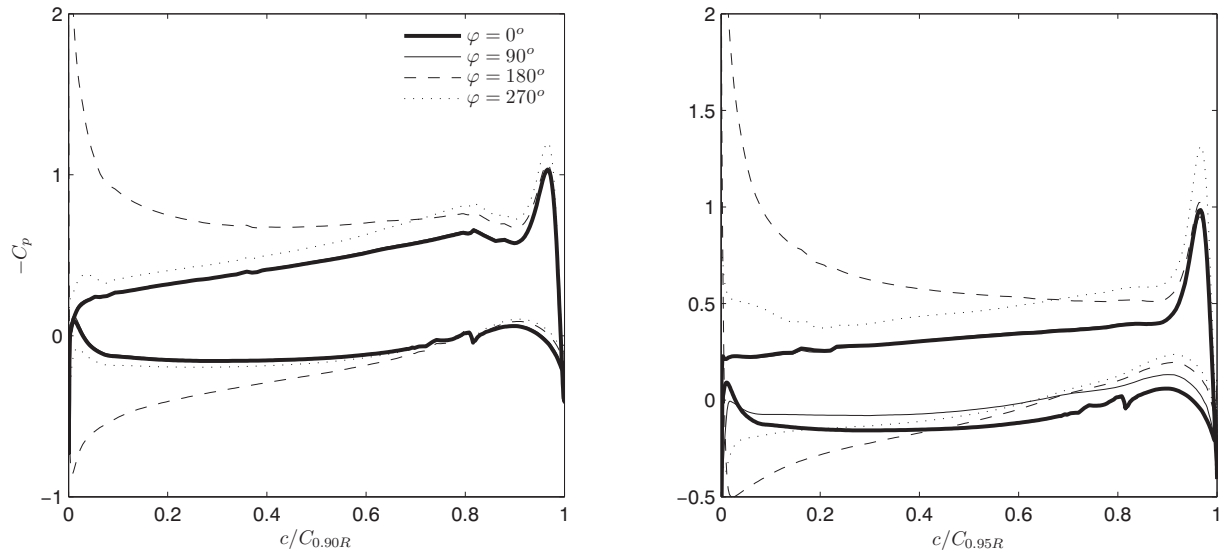

Figure 5.35: C_p on the blade surface of the highly-skewed propeller in different blade angles at $r = 0.90R$ (left) and $0.95R$ (right) for $J = 0.915, \sigma_n = 1.49$

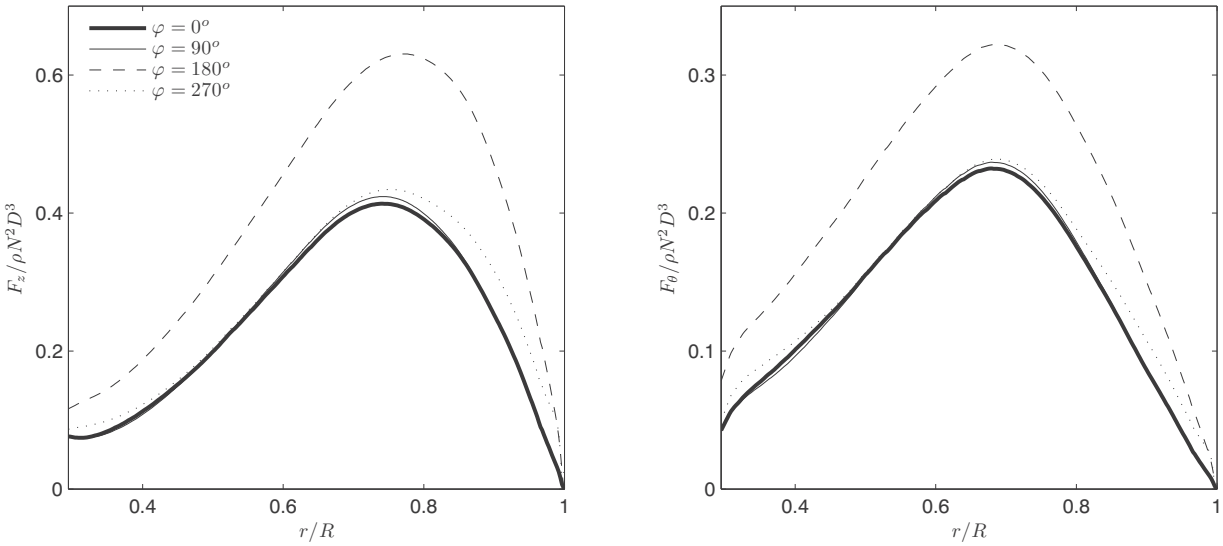

Figure 5.36: Axial (left) and tangential (right) loadings as functions of the radial distance on the highly-skewed propeller for $J = 0.915, \sigma_n = 1.49$

angle. C_p on the pressure side at the outer radius of $r = 0.95R$ is decreased at $\varphi = 90^o$. As the blade enters the high wake region at $\varphi = 180^o$, the peaks of suction and pressure appear at the leading edge. The suction peak at $r = 0.95R$ is higher than that at $r = 0.90R$. As the blade gets out of the wake at $\varphi = 270^o$, the peaks at the leading edge are lowered, but the suction peak at the trailing edge becomes higher.

The axial and tangential loadings in Figure 5.36 show that the maximum is at $r \simeq 0.75R$ for the axial loading and $r \simeq 0.7R$ for the tangential loading. The magnitude of the overall loading is increased at $\varphi = 180^o$ inside the wake field. Since the blade is outside the wake field at $\varphi = 0^o$ and 90^o, the magnitude does not differ. The weak wake is left at the outer part at $\varphi = 270^o$, the loading at outer radii is slightly higher, compared to that at $\varphi = 0^o$ and 90^o.

5.5 Conclusion for cavitating flows around marine propellers

Numerical solutions are made for the cavitating flows around the conventional and highly-skewed propellers in the open-water and behind-hull conditions. The cavitation profiles from the computation are compared with those from the experiment. The considered cases involve steady and unsteady sheet/vortex cavitation in the open-water and behind-hull conditions.

1. The numerical results in the open-water condition show reasonable quantitative and

qualitative accuracy for the steady sheet cavitation on both propellers, but the computed sheet cavity on the highly-skewed propeller has a less radial extent probably due to the difference in the turbulence characteristics.

2. The tip vortex cavitation is shortly extended or even not generated in the computation probably due to the low grid resolution in a distance from the blade surface.

3. The computations for different rotation rates with a fixed advance ratio show that a higher Reynolds number with a reduced viscous drag induces a larger extent of sheet cavity.

4. The cavity distribution on the conventional propeller in the wake peak of the behind-hull condition shows a fairly good agreement, but the variation pattern with respect to the blade angle has a considerable difference from the experimental result. It seems to be related to the difference in the wake field.

5. The variation pattern of the cavity on the highly-skewed propeller with respect to the blade angle in the behind-hull condition shows an acceptable agreement with the experimental result.

6. The actuator disk is proved to be an efficient way to apply a behind-hull wake field to the propeller in a well-preserved state.

This page is intentionally left blank.

Chapter 6

Conclusion and outlook

The four cavitation models have been implemented in the RANS solver. The momentum conservation equation with variable fluid properties and the pressure correction equation accounting for the continuity equation and the mass transfer rate are solved with the $k-\omega$ SST turbulence model. In three cavitation models, the vapor transport equation is solved for either the vapor/liquid volume fraction or the vapor mass fraction, and the definition of the source term, related to the mass transfer rate, differs for each model. The mixture fluid properties are updated according to the vapor fraction. In a fourth cavitation model, the local pressure is directly linked to the mixture fluid properties by a barotropic state law.

The validation for the cavitating flows on a 2D hydrofoil has shown that the three cavitation models with the vapor transport equation have numerical stability and equivalently good accuracy for steady and unsteady sheet cavitation. The cavitation model with the barotropic state law has shown stability problem for unsteady-state computation and comparatively lower accuracy in the present implementation.

The cavitation simulations on the 3D hydrofoils and the conventional and highly-skewed propellers are compared with the experimental results. The comparison shows that the numerical model has acceptable accuracy and robustness for steady and unsteady sheet cavitation on complicated geometries. The hydrodynamic characteristics of cavitation phenomenon like lift/drag variation with respect to the cavity extent, re-entrant jet at the sheet cavity closure, periodic oscillation of the unsteady sheet cavitation and thrust variation in propeller cavitation are demonstrated in the numerical simulation.

The cavitation simulations on propellers have been performed in the open-water and behind-hull conditions. The behind-hull wake field is applied to a plane at a radius upstream from the propeller by using the actuator disk instead of modeling a whole ship hull. The computed cavity profile in the behind-hull condition shows a reasonable agreement with the experimental result and the variation pattern of the cavitation in the inhomogeneous wake field is reproduced in the simulation with close similarity.

The overall numerical results suggest the possibility of the cavitation model in the RANS solver to be used for practical applications in the propeller cavitation analysis as a complementary tool to the cavitation tunnel test and the other numerical methods. The further research using this numerical method can be extended into the scale effects on propeller cavitation, the cavitation-induced pressure fluctuation on the ship structure and the geometrical optimization of the cavitating propeller and aft-ship.

The outstanding issue remains for the simulation of cloudy and vortex cavitation, which is related to the turbulent characteristics and the grid resolution. The higher accuracy of the LES and DES in the prediction of the turbulent components may improve the simulation of the cloudy and vortex cavitation. While the structured hexahedral mesh has been adopted in the present work, the unstructured mesh will enable a locally finer mesh around the blade tip, which can enhance the simulation of the tip vortex cavitation without a significant reduction of the computational efficiency.

References

[1] Abdel-Maksoud, M., Menter, F., Wuttke, H., "Viscous flow simulation for conventional and high-skew marine propellers", Ship Technology Research, Vol.45, 1998

[2] Bensow, R. E., "Simulating a cavitating propeller in wake flow", 12th NuTTS, 2009

[3] Brandner, P.A., *Introductory lecture on cavitation*, Cavitation Tunnel Laboratory, AMC, 2003

[4] Brennen, C. E., *Cavitation and bubble dynamics*, Oxford Univ. Press, 1995

[5] Brennen, C. E., Colonius, T., Wang, Y. C., Preston, A. "Cloud cavitation phenomena", 21th Symp. on Naval Hydrodyn., pp.239-253, 1999

[6] Breslin, J. and Andersen, P., *Hydrodynamics of ship propellers*, Cambridge University Press, 1994

[7] Bulten, N. W. H. and Oprea, I. A., "Consideration on deviation in torque prediction for propellers and waterjets with RANS codes", RINA Marine CFD Conf., Southampton, 2005

[8] Carlton, J., *Marine propellers and propulsion*, Butterworth-Heinmann Ltd., 2nd Ed., 2007

[9] Choi, J., Hsiao, C. T., Chahine, G., Ceccio, S., "Growth, oscillation and collapse of vortex cavitation bubbles", J. Fluid Mech., 2009

[10] Coutier-Delgosha, O., Reboud, J. L., Delannoy, Y., "Numerical simulation of the unsteady behavior of cavitating flows", Int. J. Numer. Meth. Fluids, 2003

[11] Crimi, P., "Experimental study of the effects of sweep on hydrofoil loading and cavitation", J. Hydronautics, Vol.4, No.1, 1970

[12] de Lange, D. F., de Bruin, G. J., "Sheet cavitation and cloud cavitation, re-entrant jet and three-dimensionality", Applied Scientific Research, 58:91-114, 1998

[13] Goncalves, E., Patella, R. F., "Numerical simulation of cavitating flows with homogeneous models", Computers & Fluids, 2009

[14] Farhat, M. and Avellan, F., "On the detachment of a leading edge cavitation", CAV2001, A8.004

[15] Ferziger, J. H. and Peric, M., *Computational methods for fluid dynamics*, Springer, 3rd Ed., 2002

[16] Franc, J. P., *The Rayleigh-Plesset equation: a simple and powerful tool to understand various aspects of cavitation*, CISM Inter. Centre for Mech. Sc., Springer, 496:pp.1-41, 2007

[17] Frikha, S., Coutier-Delgosha, O., Astolfi, J. A. "Influence of the cavitation model on the simulation of cloud cavitation on 2D foil section," Int. J. of Rotating Machinery, 2008

[18] Hirt, C. W. and Nichols, B. D., "Volume of fluid (VOF) method for the dynamics of free boundaries", J. of Comp. Ph., 39:201-225, 1981

[19] Hoeijmakers, H. W. M., Janssens, M. E., Kwan, W., "Numerical simulation of sheet cavitation", Cav '98, pp.257-262, Grenoble, France, 1998

[20] Hsiao, C. T., Chahine, G., "Prediction of tip vortex cavitation inception using coupled spherical and nonspherical bubble models and Navier-Stokes computations", J. Mar. Sci Technol., 2004

[21] Huang, J., Han, C., "Influences of gas nucleus scale on cavitation", Applied Mathematics and Mechanics (English Ed.), Vol.13, No.4, pp.359-367, 1992

[22] Johannsen, C., *Leading edge- Part2: Cavitation tests for a ferry equipped with skew propellers*, HSVA Report K51/03, 2004

[23] Kim, S. E., Brewton, S., "A multiphase approach to turbulent cavitating flows", 27th Symp. on Naval Hydrodynamics, 2008

[24] Kuiper, G., "Cavitation research and ship propeller design", Applied Sc. Research, 1998

[25] Kuiper, G., *Leading edge: Data of selected propellers*, Report No.16206-2-RD, Marin, 2004

[26] Kunz, R. F., Boger, D. A., Stinebring, D. R., Chyczewski, T. S., Lindau, J. W., Gibeling, H. J., Venkateswaran, S., Govindan, T. R., "A preconditioned Navier-Stokes method for two-phase flows with application to cavitation prediction", Computers & Fluids, 2000

[27] Li, D. Q., Lundstrom, P., *Leading edge: open water characteristics and cavitation inception tests of a conventional propeller and a highly skewed propeller*, SSPA report, 2002

[28] Lindau, J. W., Kunz, R. F., Boger, D. A., Stinebring, D. R., Gibeling, H. J., "High Reynolds number unsteady, multiphase CFD modeling of cavitating flows", J. of Fluids Engineering, 2002

[29] Lindau, J. W., Boger, D. A., Medvitz, R. B., Kunz, R. F., "Propeller cavitation breakdown analysis", J. of Fluids Engineering, 2005

[30] Lindell, P., *Cavitation tunnel tests with final design propeller*, SSPA Report 3790-1, 2005

[31] Lindenau, O. and Bertram, V., "RANSE simulation of cavitating flow at a foil", Ship Technology Research, Vol.50, 2003

[32] Lydorf, U., *Leading edge: Cavitation inception test of a highly skewed propeller*, HSVA Report K56-05, 2005

[33] Maquil, T., *Simulation von instationaren kavitierenden Stromungen mit Hilfe von Mischungsbruchansatzen*, Kleine Studienarbeit, TUHH, 2007

[34] Menter, F. R., Kuntz, M., Langtry, R., "Ten years of industrial experience with the SST turbulence model", 4th Int. Symp. on Turbulence, Heat and Mass Transfer, Begell House, New York, 2003

[35] Merkle, C. L., Feng, J. Z., Buelow, P. E., "Computational modeling of the dynamics of sheet cavitation", CAV '98, pp.307-311, Grenoble, France, 1998

[36] Michelsen, J. A., *Block structured multigrid solution of 2D and 3D elliptic PDE's*, Technical Report AFM 94-06, DTU, Lyngby, 1994

[37] Michelsen, J. A., *General curvilinear transformation of the Navier-Stokes equations in a 3D polar rotating frame*, ET-AFM 98-01, DTU, Lyngby, 1998

[38] Mikkelsen, R., *Actuator disc methods applied to wind turbines*, PhD Thesis, DTU, Lyngby, 2003

[39] Mikkelsen, R., Andersen, P., Sørensen, J. N., "Modeling of behind condition wake flow in RANS computation on a conventional and high skew propeller", 10th NuTTS, 2007

[40] Mrugowski, A., *Leading edge- Part1: Propulsion tests for a ferry equipped with skew propellers*, HSVA Report WP 102/03, 2003

[41] Philipp, A. and Lauterborn, W., "Cavitation erosion by single laser-produced bubbles", J. Fluid Mech., 1998

[42] Rhee, S. H., Kawamura, T., Li, H. "Propeller cavitation study using an unstructured grid based Navier-Stokes solver", J. of Fluids Engineering, 2005

[43] Saad, Y., *Iterative methods for sparse linear systems*, Siam, 2003

[44] Sato, K., Saito Y. "Unstable cavitation behavior in a circular-cylindrical orifice flow", CAV2001, A9.003

[45] Saurel, R., Lemetayer, O., "A multiphase model for compressible flows with interfaces, shocks, detonation waves and cavitation", J. Fluid Mech., 2001

[46] Senocak, I., Shyy, W., "Interfacial dynamics-based modelling of turbulent cavitating flows, part-1: Model development and steady-state computations", Int. J. Numer. Meth. Fluids, 2004

[47] Senocak, I. and Shyy, W., "Interfacial dynamics-based modelling of turbulent cavitating flows, part-2: Time-dependent computations", Int. J. Numer. Meth. Fluids, 2004

[48] Shen, Y. J. and Dimotakis, J. S., "The influence of surface cavitation on hydrodynamics forces", 22nd ATTC, 1989

[49] Shin, K. W., Andersen, P., Shen, W. Z., "Analysis of numerical models for cavitation on 2D hydrofoil", 12th NuTTS, 2009

[50] Simonsen, C. D. and Carstens, R., *Numerical flow simulation of model ship with appendages: Method, validation and investigation of the flow around hull, rudder and propeller*, DCMT Report, 2009

[51] Singhal, A. K., Athavale, M. M., Li, H., Jiang, Y., "Mathematical basis and validation of the full cavitation model", J. of Fluids Engineering, Vol.124, pp.617-624, 2002

[52] Sørensen, N. N., $k-\omega$ *turbulence models implementation and testing*, Risø-R-864(EN), Roskilde, 1995

[53] Sørensen, N. N., *General purpose flow solver applied to flow over hills*, Risø-R-827(EN), Roskilde, 2003

[54] Special commitee on cavitation induced pressures: final report and recommendations to the 23rd ITTC, Vol.II, 2002

[55] Special committee on cavitation: final report and recommendations to the 25th ITTC, Vol.II, 2008

[56] Special commitee on water quality and cavitation: final report and recommendations to the 23rd ITTC, Vol.II, 2002

[57] Suslick, K. S., "Sonoluminescence and sonochemistry", Encyclopedia of Physical Sc. and Tech., 3rd Ed., 2001

[58] Takekoshi, Y., Kawamura, T., Yamaguch, H., Maeda, M., Ishi, N., Kimura, K., Taketani, T., and Fujii, A., "Study on the design of propeller blade sections using the optimization algorithm", J. Mar. Sci. Technol., 2005

[59] Tamura, Y. and Matsumoto, Y., "Improvement of bubble model for cavitating flow simulations", J. of Hydrodynamics, 21(1):41-46, 2009

[60] Terwisga, T., Wijngaarden, E., Bosschers, J. and Kuiper, G., "Achievements and challenges in cavitation research on ship propellers", Int. Shipbuilding Progress, 2007

[61] Ukon, Y., "Cavitation characteristics of a finite swept wing and cavitation noise reduction due to air injection", Int. Symp. Propeller and Cavitation, Wuxi, pp.383-390, 1986

[62] Wang, G., Senocak, I., Shyy, W., Ikohagi, T., Cao, S., "Dynamics of attached turbulent cavitating flows", Progress in Aerospace Sciences, 2001

[63] Wikstrom, N., "Modeling of cavitating flow around a stationary/moving wing profile", 43rd AIAA Aerospace Sciences Meeting, 2005

[64] Zwart, P. J., Gerber, A. G., Belamri, T., "A two-phase flow model for predicting cavitation dynamics", ICMF, 2004

This page is intentionally left blank.

Appendix A

A.1 SST $k-\omega$ model with the modified definition of μ_t

The SST model (Menter et al., 2003) is based on the $k-\omega$ model with some modifications using a blending function. To obtain μ_t, two transport equations are solved for the turbulent kinetic energy k and specific dissipation rate ω, respectively, as follows

$$\frac{\partial}{\partial t}(\rho k) + \frac{\partial}{\partial x_j}(\rho u_j k) - \frac{\partial}{\partial x_j}\left((\mu + \sigma_{k0}\mu_t)\frac{\partial k}{\partial x_j}\right) = \min(\mu_t P_k, 10\beta^*\rho k\omega) - \beta^*\rho k\omega \quad \text{(A.1)}$$

$$\frac{\partial}{\partial t}(\rho \omega) + \frac{\partial}{\partial x_j}(\rho u_j \omega) - \frac{\partial}{\partial x_j}\left((\mu + \sigma_{\omega 0}\mu_t)\frac{\partial \omega}{\partial x_j}\right) = \alpha_0\rho P_k - \beta_0\rho\omega^2 + \frac{2\rho\sigma_{\omega 2}(1-F_1)}{\omega}\frac{\partial k}{\partial x_i}\frac{\partial \omega}{\partial x_i} \quad \text{(A.2)}$$

where

$$P_k = \frac{\partial u_i}{\partial x_j}\left(\frac{\partial u_i}{\partial x_j} + \frac{\partial u_j}{\partial x_i}\right), \qquad F_1 = \tanh(\arg_1^4), \qquad \arg_1 = \min\left(\arg_2, \frac{4\rho\sigma_{\omega 2}k}{CD_{k\omega}d^2}\right) \quad \text{(A.3)}$$

$$\arg_2 = \max\left(\frac{2\sqrt{k}}{\beta^*\omega d}, \frac{500\mu}{\rho d^2\omega}\right), \qquad CD_{k\omega} = \max\left(\frac{2\rho\sigma_{\omega 2}}{\omega}\frac{\partial k}{\partial x_i}\frac{\partial \omega}{\partial x_i}, 10^{-10}\right) \quad \text{(A.4)}$$

and where d is the distance from the wall and the constants with a subscript 0 are computed by a blend of the corresponding constant from the $k-\omega$ model with a subscript 1 and the one from $k-\epsilon$ model with a subscript 2 via $\alpha_0 = \alpha_1 F_1 + \alpha_2(1-F_1)$, and $\beta^* = 0.090, \alpha_1 = 0.5532, \beta_1 = 0.0750, \sigma_{k1} = 0.850, \sigma_{\omega 1} = 0.500, \alpha_2 = 0.4404, \beta_2 = 0.0828, \sigma_{k2} = 1.000, \sigma_{\omega 2} = 0.856$.

μ_t is defined as follows (Frikha et al., 2008)

$$\mu_t = \frac{a_1 k(\rho_v + (1-\alpha_v)^{10}(\rho_l - \rho_v))}{\max(a_1\omega, F_2\sqrt{P_k})} \quad \text{(A.5)}$$

where $a_1 = 0.31$ and $F_2 = \tanh(\arg_2)$.

k and ω at an inlet boundary are specified and they have a zero-gradient condition at an outlet. The wall boundary condition is

$$k = 0, \qquad \omega = 10\frac{6\nu}{\beta_1 d^2} \tag{A.6}$$

A.2 Boundary conditions

Convective boundary condition

The unsteady convective boundary condition (Ferziger and Peric, 2002) at an east face as an example is

$$\frac{\partial \phi_e}{\partial t} + U\left(\frac{\partial \phi}{\partial n}\right)_e = 0 \tag{A.7}$$

where U is a velocity on the outlet surface, which is chosen to fulfill the global mass conservation, n is the unit vector outward normal to the boundary surface.

Its integral form is approximated by the linear interpolation for the face value, the CDS for the gradient and the second-order backward differencing scheme for the time derivative as follows

$$\frac{1}{\Delta t}\left[\frac{3}{2}\left(\frac{\phi_P + \phi_E}{2}\right) - 2\phi_e^* + \frac{1}{2}\phi_e^{**}\right]\left(\frac{\Delta V_P + \Delta V_E}{2}\right) + U\Delta A_e(\phi_E - \phi_P) = 0 \tag{A.8}$$

$$\rightarrow \phi_E = \phi_P \frac{A_1 - 1}{A_1 + 1} + \frac{2A_2}{A_1 + 1} \tag{A.9}$$

where the superscripted asterisk $*$ and double asterisk $**$ indicate the value at the previous and second previous time steps, respectively, and

$$A_1 = \frac{8}{3}\frac{U\Delta A_e \Delta t}{\Delta V_P + \Delta V_E}, \qquad A_2 = \frac{2}{3}(2\phi_e^* - \frac{1}{2}\phi_e^{**}) \tag{A.10}$$

By inserting ϕ_E into the linear equation, the coefficients and the source term are updated as follows

$$A_P^b = A_P + A_E\frac{A_1 - 1}{A_1 + 1}, \qquad S^b = S - 2A_E\frac{A_2}{A_1 + 1}, \qquad A_E^b = 0 \tag{A.11}$$

Dirichlet boundary condition

The Dirichlet boundary condition at an east face is

$$\phi_e = \frac{\phi_P + \phi_E}{2} = \phi_b \qquad \rightarrow \qquad \phi_E = 2\phi_b - \phi_p \tag{A.12}$$

The coefficients and the source term are updated as follows

$$A_P^b = A_P - A_E, \qquad S^b = S - 2A_E\phi_b, \qquad A_E^b = 0 \tag{A.13}$$

Neumann boundary condition

The Neumann boundary condition at an east face is

$$\left(\frac{\partial\phi}{\partial n}\right)_e = \phi_E - \phi_P = \nabla\phi_b \qquad \rightarrow \qquad \phi_E = \phi_p + \nabla\phi_b \tag{A.14}$$

The coefficients and the source term are updated as follows

$$A_P^b = A_P + A_E, \qquad S^b = S - A_E\nabla\phi_b, \qquad A_E^b = 0 \tag{A.15}$$

A.3 Numerical tests for Model 4

The derivative of $\dot{m}$ with respect to p for Model 4 is defined by

$$\frac{\partial \dot{m}}{\partial p} = \left| \frac{C_b \dot{m}}{p - p_v} \right| \tag{A.16}$$

To determine the value of C_b, numerical tests are conducted for $\alpha = 4^o, \sigma = 0.91$ with the 2D hydrofoil used in Chapter 3. As shown in Figure A.1, the cavity size is underestimated for $C_b = 100$ and the cavity is fully extended for $C_b = 10$. As C_b is decreased below 10, the cavity closure becomes unstable and the instability spreads from the fore part of the cavity to the trailing edge of the hydrofoil. For $C_b < 0.1$, the computation crashes due to the numerical instability.

As C_b is increased, the linear equation (2.34) is more stabilized. However, the cavity can be underestimated for an excessive high value of C_b, because the effect of the mass transfer rate in the source term is weakened. $C_b = 10$ is applied to the computation with Model 4 in Chapter 3.

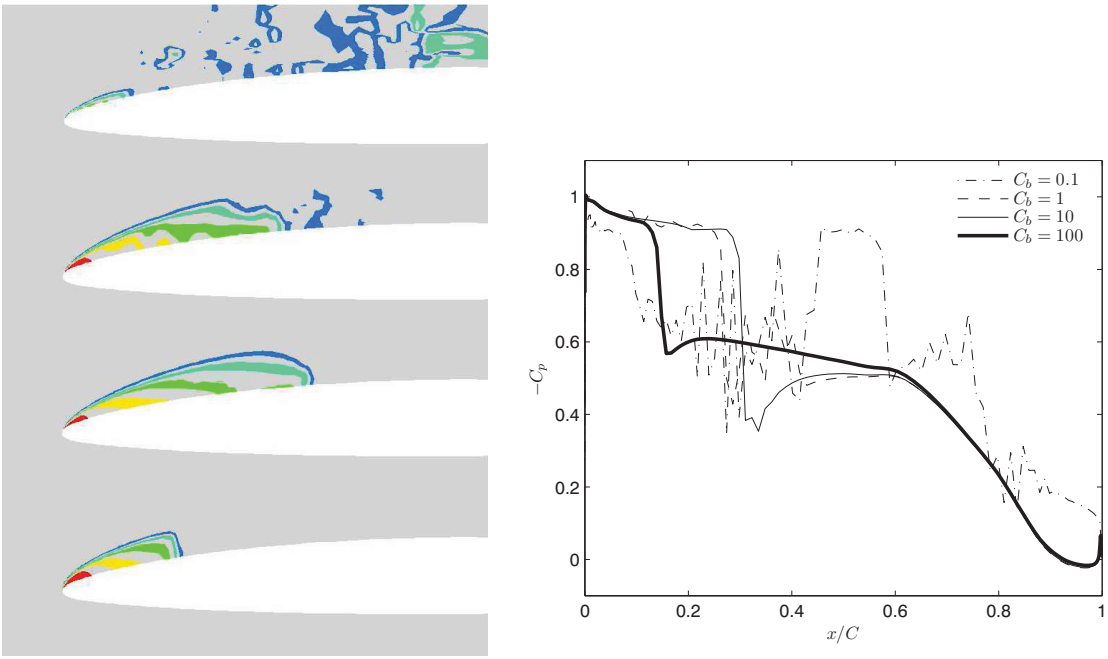

Figure A.1: α_v (left) for $C_b = 0.1, 1, 10, 100$ (from top to bottom) and pressure coefficient on the suction side (right) for $\alpha = 4^o, \sigma = 0.91$

A.4 Main particulars for propellers and ship

		Conventional propeller	Highly-skewed propeller
Full-scale diameter	D_S	$6.6m$	$5.2m$
Model scale factor	λ	23.50	22.29
Boss/Diameter ratio	D_H/D	0.181	0.315
Expanded blade area ratio	A_e/A_o	0.586	0.729
Design pitch ratio at $0.7R$	$P_{0.7R}/D$	0.701	1.224
Chord-length ratio at $0.7R$	$C_{0.7R}/D$	0.315	0.500
Thickness at $0.7R$	$t_{0.7R}$	$0.004m$	$0.002m$
		Tanker	Ferry
Length between perpendiculars	L_{pp}	–	$163.40m$
Breadth	B	–	$30.50m$
Draft*	T	$9.12m$	$6.50m$
Block coefficient	C_B	–	0.607
Wetted area	S	–	$5287m^2$

* It refers to the draft on even keel in the cavitation tunnel test with the wooden plate substituted for the free surface.

PhD Theses
Department of Naval Architecture and Offshore Engineering
Technical University of Denmark · Kgs. Lyngby

1961 Strøm-Tejsen, J.
Damage Stability Calculations on the Computer DASK.

1963 Silovic, V.
A Five Hole Spherical Pilot Tube for three Dimensional Wake Measurements.

1964 Chomchuenchit, V.
Determination of the Weight Distribution of Ship Models.

1965 Chislett, M.S.
A Planar Motion Mechanism.

1965 Nicordhanon, P.
A Phase Changer in the HyA Planar Motion Mechanism and Calculation of Phase Angle.

1966 Jensen, B.
Anvendelse af statistiske metoder til kontrol af forskellige eksisterende tilnærmelsesformler og udarbejdelse af nye til bestemmelse af skibes tonnage og stabilitet.

1968 Aage, C.
Eksperimentel og beregningsmæssig bestemmelse af vindkræfter på skibe.

1972 Prytz, K.
Datamatorienterede studier af planende bådes fremdrivningsforhold.

1977 Hee, J.M.
Store sideportes indflydelse på langskibs styrke.

1977 Madsen, N.F.
Vibrations in Ships.

1978 Andersen, P.
Bølgeinducerede bevægelser og belastninger for skib på lægt vand.

1978 Römeling, J.U.
Buling af afstivede pladepaneler.

1978 Sørensen, H.H.
Sammenkobling af rotations-symmetriske og generelle tre-dimensionale konstruktioner i elementmetode-beregninger.

1980 Fabian, O.
Elastic-Plastic Collapse of Long Tubes under Combined Bending and Pressure Load.

1980 Petersen, M.J.
Ship Collisions.

1981 Gong, J.
A Rational Approach to Automatic Design of Ship Sections.

1982 Nielsen, K.
Bølgeenergimaskiner.

1984 Nielsen, N.J.R.
Structural Optimization of Ship Structures.

1984 Liebst, J.
Torsion of Container Ships.

1985 Gjersøe-Fog, N.
Mathematical Definition of Ship Hull Surfaces using B-splines.

1985 Jensen, P.S.
Stationære skibsbølger.

1986 Nedergaard, H.
Collapse of Offshore Platforms.

1986 Yan, J.-Q.
3-D Analysis of Pipelines during Laying.

1987 Holt-Madsen, A.
A Quadratic Theory for the Fatigue Life Estimation of Offshore Structures.

1989 Andersen, S.V.
Numerical Treatment of the Design-Analysis Problem of Ship Propellers using Vortex Lattice Methods.

1989 Rasmussen, J.
Structural Design of Sandwich Structures.

1990 Baatrup, J.
Structural Analysis of Marine Structures.

1990 Wedel-Heinen, J.
Vibration Analysis of Imperfect Elements in Marine Structures.

1991 Almlund, J.
Life Cycle Model for Offshore Installations for Use in Prospect Evaluation.

1991 Back-Pedersen, A.
Analysis of Slender Marine Structures.

1992 Bendiksen, E.
Hull Girder Collapse.

1992 Petersen, J.B.
Non-Linear Strip Theories for Ship Response in Waves.

1992 Schalck, S.
Ship Design Using B-spline Patches.

1993 Kierkegaard, H.
Ship Collisions with Icebergs.

1994 Pedersen, B.
A Free-Surface Analysis of a Two-Dimensional Moving Surface-Piercing Body.

1994 Hansen, P.F.
Reliability Analysis of a Midship Section.

1994 Michelsen, J.
A Free-Form Geometric Modelling Approach with Ship Design Applications.

1995 Hansen, A.M.
Reliability Methods for the Longitudinal Strength of Ships.

1995 Branner, K.
Capacity and Lifetime of Foam Core Sandwich Structures.

1995 Schack, C.
Skrogudvikling af hurtiggående færger med henblik på sødygtighed og lav modstand.

1997 Simonsen, B.C.
Mechanics of Ship Grounding.

1997 Olesen, N.A.
Turbulent Flow past Ship Hulls.

1997 Riber, H.J.
Response Analysis of Dynamically Loaded Composite Panels.

1998 Andersen, M.R.
Fatigue Crack Initiation and Growth in Ship Structures.

1998 Nielsen, L.P.
Structural Capacity of the Hull Girder.

1999 Zhang, S.
The Mechanics of Ship Collisions.

1999 Birk-Sørensen, M.
Simulation of Welding Distortions of Ship Sections.

1999 Jensen, K.
Analysis and Documentation of Ancient Ships.

2000 Wang, Z.
Hydroelastic Analysis of High-Speed Ships.

2000 Petersen, T.
Wave Load Prediction—a Design Tool.

2000 Banke, L.
Flexible Pipe End Fitting.

2000 Simonsen, C.D.
Rudder, Propeller and Hull Interaction by RANS.

2000 Clausen, H.B.
Plate Forming by Line Heating.

2000 Krishnaswamy, P.
Flow Modelling for Partially Cavitating Hydrofoils.

2000 Andersen, L.F.
Residual Stresses and Deformations in Steel Structures.

2000 Friis-Hansen, A.
Bayesian Networks as a Decision Support Tool in Marine Applications.

PhD Theses
Maritime Engineering · Department of Mechanical Engineering
Technical University of Denmark · Kgs. Lyngby

2001 Lützen, M.
Ship Collision Damage.

2001 Olsen, A.S.
Optimisation of Propellers Using the Vortex-Lattice Method.

2002 Rüdinger, F.
Modelling and Estimation of Damping in Non-linear Random Vibration.

2002 Bredmose, H.
Deterministic Modelling of Water Waves in the Frequency Domain.

2003 Urban, J.
Crushing and Fracture of Lightweight Structures.

2003 Lazarov, B.S.
Slepian Simulations of Plastic Displacement of Randomly Excited Hysteretic Structures.

2003 Ravn, E.S.
Probabilistic Damage Stability of Ro-Ro Ships.

2003 Törnqvist, R.
Design of Crashworthy Ship Structures.

2003 Nielsen, K.B.
Numerical Prediction of Green Water Loads on Ships.

2004 Folsø, R.
Comfort Monitoring of High Speed Passenger Ferries.

2004 Fuhrman, D.R.
Numerical Solutions of Boussinesq Equations for Fully Nonlinear and Extremely Dispersive Water Waves.

2004 Dietz, J.S.
Application of Conditional Waves as Critical Wave Episodes for Extreme Loads on Marine Structures.

2004 Berggreen, C.
Damage Tolerance of Debonded Sandwich Structures.

PhD Theses
Coastal, Maritime and Structural Engineering
Department of Mechanical Engineering
Technical University of Denmark · Kgs. Lyngby

2005 Berntsen, K.N.
Modelling Granular Media and Molecular Dynamics Simulations of Ellipses.

2005 Nielsen, U.D.
Estimation of Directional Wave Spectra from Measured Ship Responses.

2005 Vidic-Perunovic, J.
Springing Response due to Bidirectional Wave Excitation.

2005 Zhang, H.
A Deterministic Combination of Numerical and Physical Models for Coastal Waves.

2005 Hgsberg, J.R.
Modelling of Dampers and Damping in Structures.

2006 Engsig-Karup, A.P.
Unstructured Nodal DG-FEM solution of High-order Boussinesq-type Equation.

2006 Yamada, Y.
Bulbous Buffer Bows: A Measure to Reduce Oil Spill in Tanker Collisions.

2008 Lundsgaard-Larsen, C.
Predicting and Improving Damage Tolerance of Composite Structures.

2009 Joncquez, Soizic A.G.
Second-order Forces and Moments acting on Ships in Waves.

2010 Lajic, Zoran
Fault - Tolerant Onboard Monitoring and Decision Support Systems.

DTU Mechanical Engineering
Section of Coastal, Maritime and Structural Engineering
Technical University of Denmark

Nils Koppels Allé, Bld. 403
DK- 2800 Kgs. Lyngby
Denmark
Phone (+45) 45 25 13 60
Fax (+45) 45 88 43 25

www.mek.dtu.dk